Technische Universität München

Max-Planck-Institut für Biochemie

Abteilung für Molekulare Strukturbiologie

# "Structural analysis of short-term release facilitation in synaptosomes and synapses"

Ulrike Laugks

Vollständiger Abdruck der von der Fakultät für Chemie der Technischen Universität München zur Erlangung des akademischen Grades eines Doktors der Naturwissenschaften genehmigten Dissertation.

# Contents

Contents

# Summary

Neuronal cells and their highly specialized entities, axonal processes and synaptic connections, continue to be of tremendous interest in the different fields of microscopy. Synaptic plasticity and facilitation of neurotransmitter release was intensively studied by electrophysiology, but little ultrastructural data of release facilitated synapses exist. To investigate synaptic vesicle priming during synaptic plasticity neuronal samples have been routinely treated with phorbol esters, tumor promotors, which are known to activate protein kinase C (PKC) and translocate Munc13 to the presynaptic membrane. Experiments executed so far could not demonstrate to what extent phorbol ester dependent synaptic plasticity is modified by the increased activity of the enzyme PKC or by the anchoring of Munc13 to the site of synaptic vesicle fusion. By the application of the phorbol ester 4-β-phorbol-12,13-dibutyrat (PDBu) and two differently acting inhibitors of PKC to neuronal samples, the selectively inhibiting staurosporin Ro31-8220 and the chemical compound Calphostin C, we could determine the importance of PKC and Munc13 for release facilitation. These treatments were applied to both isolated synaptic terminals derived from rodent cortices and to a lesser extend to primary cultured neurons grown from dissociated embryonic hippocampal cells. By vitrification, neuronal specimen were fixed in a fully hydrated, close-to-native state for the acquisition of three-dimensional data by means of cryo-electron tomography. Since this unique method allows to investigate ultrastructural details of thin biological samples without artifacts from resin embedding procedures and heavy metal staining, the fine details of the synaptic release machinery during synaptic plasticity can be visualized. Tomography data was analyzed by hierarchical segmentation of filaments connecting synaptic vesicles with each other (connectors) and to the presynaptic membrane (tethers) as well as other synaptic features. We found that PDBu-treated and PKC-inhibited synaptosomes by Ro31, showed increased numbers of synaptic vesicles tethered to the presynaptic membrane, as well as vesicles tethered by multiple tethers and thus being in the enhanced readily releasable pool. Both treatments showed spontaneous and evoked PDBu-dependent release facilitation, features that could be obliterated by Calphostin C, a PKC-inhibitor simultaneously blocking the translocation of Munc13. Complete PKC-inhibition, although not influencing release facilitation, resulted in reduced numbers of short tethers (< 10 nm), presumably due to the lack of PKC-dependent phosphorylation of Munc18

Summary

and the SNARE-complex binding partner SNAP-25. Thus, we could visualize two different states of release facilitation. PDBu-dependent Munc13 translocation leads to the formation of a priming complex consisting of long tethers, while the following step of short tether formation is stimulated by PKC-activation. Furthermore, release facilitated synaptosomes showed increased connector lengths in proximity to vesicle release sites, presumably provoking increased spontaneous transmitter release. While the analysis of synaptosomes enabled statistical analysis of synaptic plasticity, limited data acquired from synapses in primary cultured neurons, from samples thinned by focused ion beam milling, confirmed the main results. Additionally, neurons grown on electron microscopy grids reveal ultrastructural features of non-synaptic axonal boutons, as well as significant structural differences between immature and fully developed synapses.

# Zusammenfassung

Nervenzellen, bestehend aus hochspezialisierten Axonen und synaptischen Verbindungen, sind für die verschiedenen Bereiche der Mikroskopie von anhaltendem Interesse. Synapsenplastizität und die Potenzierung von Transmitterfreisetzung wurden mit Hilfe der Elektrophysiologie intensiv erforscht, aber es existiert nur wenig ultrastrukturelle Information in diesem Bereich. Für die Untersuchung der Bereitstellung synaptischer Vesikel im Zusammenhang mit synaptischer Plastizität wurden Nervenzellen routinemäßig mit Phorbolestern behandelt. Diese sind dafür bekannt das Enzym Proteinkinase C (PKC) zu aktivieren und gelten somit als karzinogen. Zusätzlich verankern Phorbolester das Molekül Munc13 in der präsynaptischen Membran. In welchem Ausmaß die durch Phorbolester ausgelöste Synapsenplastizität durch die Aktivierung von PKC oder die Verankerung von Munc13 am Ort der Transmitterausschüttung ausgelöst wird, konnte in bisherigen Studien nicht gezeigt werden. Durch die Anwendung des Phorbolesters 4-β-phorbol-12,13-dibutyrat (PDBu) und zweier unterschiedlich wirkenden Inhibitoren von PKC, das selektiv inhibierende Staurosporin Ro31-8220 und die Chemikalie Calphostin C, konnten wir die Rolle von PKC und Munc13 für die synaptische Potenzierung bestimmen. Als Proben dienten sowohl aus dem Nagerkortex isolierte Synapsen, als auch in Primärzellkultur kultivierte Neuronen aus dissoziierten embryonalen Hippocampi. Diese neuronalen Proben wurden durch Vitrifizierung in amorphem Eis eingebettet und im nativen Zustand für die Aufnahme dreidimensionaler Tomogramme am Kryo-Elektronenmikroskop vorbereitet. Diese einzigartige Methode erlaubt die Untersuchung ultrastruktureller Details dünner biologischer Proben, wobei die Artefakte durch Harzeinbettung und Schwermetallkontrastierung vermieden werden und somit die Visualisierung der präsynaptischen Maschinerie während der Signalübertragungspotenzierung ermöglicht wird. In den Tomogrammen wurden die Filamente, die die synaptischen Vesikel miteinander (connector) oder mit der präsynaptischen Membran (tether) verbinden, durch hierarchische Segmentierung analysiert und auf andere Eigenschaften hin untersucht. Wir stellten fest, dass mit PDBu behandelte Synaptosomen und Proben mit zusätzlich durch Ro31 inhibierter Aktivität des Enzyms PKC, eine höhere Anzahl an die präsynaptische Membran gebundener synaptischer Vesikel aufweisen und diese Vesikel durch mehrere Filamente gebunden waren. Somit zeichnen sich diese Vesikel mit hoher Freisetzungswahrscheinlichkeit aus.

Zusammenfassung

Weiterhin zeigten mit PDBu und Ro31 behandelte Proben eine Potenzierung von spontaner und stimulierter Transmitterausschüttung. Dieser Effekt wurde durch die Behandlung mit CalC verhindert, da dieser Inhibitor sowohl die Aktivierung von PKC als auch die Verankerung von Munc13 verhindert. Die alleinige Inhibierung von PKC durch Ro31, beeinflusste nicht die PDBu-abhängige Potenzierung der Transmitterausschüttung, resultierte aber in einer geringeren Anzahl kurzer tether-Filamente (< 10 nm), was vermutlich durch die fehlende PKC-abhängige Phosphorylierung von Munc18 und des SNARE-Komplex Moleküls SNAP-25 ausgelöst wird. Folglich konnten zwei unterschiedliche Stufen der Signalübertragungspotenzierung visualisiert werden. Die PDBu-abhängige Munc13-Aktivierung führt zur Bildung von priming-Komplexen, die aus langen Filamenten bestehen, während die nachfolgende Bildung kurzer tether-Filamente durch PKC-Aktivierung stimuliert wird. Weiterhin zeigten Synaptosomen mit potenzierter Signalübertragung verlängerte connector-Filamente im proximalen Bereich der Vesikelfusion, was auf eine Förderung der spontanen Transmitterausschüttung hindeutet. Während die statistische Auswertung von synaptischer Potenzierung durch die Analyse von Synaptosomen ermöglicht wurde, bestätigte ein begrenzter Datensatz von Synapsen aus primärer Zellkultur, die durch Ionendünnung bearbeitet wurden, die wichtigsten Ergebnisse der Studie. Zusätzlich eröffnen Neuronen, die auf Probenträgern für Elektronenmikroskopie kultiviert wurden, den Blick auf die Ultrastruktur von nicht-synaptischen axonalen Schwellungen, sowie signifikante strukturelle Unterschiede zwischen unreifen und voll entwickelten Synapsen.

# 1. Introduction

## 1.1 Transmission electron microscopy of native specimens

Cryo-electron tomography (CET) provides an insight into the three-dimensional (3D) near-to-native organization (Lučić et al., 2013) of purified protein complexes, isolated cellular organelles endowed with macromolecular complexes and even intact cells, provided that a thickness of 500 nm is not exceeded (Brandt et al., 2010; Koning, 2010). With focused ion beam (FIB) milling even thicker structures can be targeted and in combination with correlative light microscopy specific sub-volumes of the cell can be localized and imaged (Engel et al., 2015; Rigort et al., 2010, 2012). Since the development of advanced image processing techniques, subtomogram averaging became an established method allowing to analyze the orientation and location of protein complexes relative to each other *in situ*. Initial analysis was performed for large structures like the nuclear pore complex (Beck et al., 2004) and recently advanced to the investigation of the 26S proteasome inside the cell and nucleus (Albert et al., 2017; Asano et al., 2015). For the structural analysis of isolated complexes (single particle analysis), CET aims to balance with biochemistry for detailed information of subdomains of the molecule to understand the protein in its cellular context. The supplementation of structural results becomes more and more obsolete since the development of direct electron detection devices (DDD) (Li et al., 2013) and more advanced data processing software (Chen et al., 2013) allow subtomogram averaging to reach sub-nanometer resolution (Schur et al., 2015).

### 1.1.1 Basics of cryo electron microscopy

The basic functionality of electron microscopy (EM) is in multiple aspects comparable to light microscopy (LM) with electrons probing an object instead of light waves (Frank, 2006). The three methodologies of EM comprise transmission electron microscopy (TEM), which will be described in detail below, as well as scanning electron microscopy (SEM) suitable for the analysis of the surface of a sample by detection of secondary and backscattered electrons. As the third method electron crystallography allows the investigation of two-dimensional (2D) crystals of a layer of periodically arranged proteins.

Introduction

The scattering pattern of electrons passing through the crystal acquired at different tilt angles permits determination of the three-dimensional (3D) structure (Glaeser, 1999; Lottspeich and Engels, 2006).

Data collection for this work was performed at different TEMs operated at 300 kV. As for light-optical methods, EM imaging resolution depends on the wavelength but compared to the maximum resolution achievable in common LM-techniques of around 200 nm, TEM allows a theoretical resolution in the picometer range. However the resolution reached by the best microscopes is around 0.5 Å (Kisielowski et al., 2008) and foremost resolution is limited for imaging of biological samples. Electrons interact strongly with matter, resulting in breakage of chemical bonds and release of free radicals in organic objects, creating sample damage (Glaeser and Taylor, 1978). The interaction of electrons and specimen atoms creates the electron microscopic image. Elastic scattering of electrons is the result of electron-sample interaction, with electrons interacting with the nuclei of the sample atoms. The scattering angle of the electron is higher the larger the atomic number and the closer the electron passes the specimen atom nucleus. Elastically scattered electrons contribute to the image information, while inelastically scattered electrons are events of interaction of electrons with the atomic shell of the specimen atom and do not contribute to image information but result in noise (Reimer and Kohl, 2008). In SEM the topology of an object is probed by detection of secondary electrons, while elastically backscattered electrons or emitted X-rays are detected in analytical SEM to draw conclusions of the chemical compounds of the specimen (Goldstein et al., 2003).

All types of EM require a method of sample fixation, as the high vacuum conditions leads to evaporation from samples in the native state. This issue was solved by using chemical fixation, dehydration and plastic embedding followed by heavy metal staining, which significantly improves the signal-to-noise ratio (SNR) but hides high resolution information and due to fixation modifies internal structural details. Rapid freezing employed for cryo-electron microscopy (Cryo-EM) is the preferred method rendering the sample in a hydrated and close to native state in a non-crystalline layer of vitreous ice.

Due to the low intrinsic contrast of the unstained sample and owing the fact that organic samples can be exposed to merely minimal electron doses to avoid afore mentioned

sample damage (low-dose imaging: see 3.3) the SNR is commonly very low in Cryo-TEM. The theory of image formation and phase contrast will be explained in detail in chapter 1.1.3.

## 1.1.2  Essential elements of a transmission electron microscope

A basic cryo-TEM is made up an electron source, a set of electromagnetic and electrostatic lenses, a liquid nitrogen ($LN_2$) cooled sample holder and a detection device, with all compartments kept in high vacuum. The following chapter will describe the individual segments in detail (see also Figure 1).

The electron source emits and accelerates electrons into the column which is kept in constant vacuum (usually $10^{-10}$ bar) to prevent interaction between electrons and gas molecules (Williams and Carter, 2009). The microscopes used in this study are all equipped with modern field emission guns (FEG) with an acceleration voltage of 300 keV. FEGs consist of a pointed tungsten cathode tip and at least two anodes. Electron extraction is performed by applying a high voltage to the crystal, producing a very strong electric field at the sharp tip (Kirkland et al., 2007). In contrast to conventional electron sources making use of thermionic emission from a tungsten or lanthanum hexaboride wire, FEGs produce a bright electron beam with a narrow energy spread. Furthermore, modern FEGs stand out due to high temporal and spatial coherence, achieved by mechanic tunneling, creating a stable electron beam and the basis for high resolution imaging (Förster et al., 2012; Reimer and Kohl, 2008).

The illumination system is a set of lenses focusing the beam on the sample. Lenses in EM are electromagnetic lenses consisting of coils creating a radially symmetric magnetic field, acting similar to optical lenses. Deviations from the radial symmetry of the magnetic field result in astigmatism, which has to be corrected for during alignment of the illumination system. The first lenses manipulating the electron beam are a set of at least two condenser lenses (C1 and C2) able to provide illumination of the specimen, ideally in parallel illumination. Condenser lens C1 de-magnifies the gun cross-over and thus controls the physical size of the beam on the specimen, also known as spot size, which can be modified by the user depending on the required electron dose. The C2 lens allows to manually set the size of the illumination area on the sample, while limiting the radiation damage and contamination in nonirradiated areas and thus outside the field of view. The Titan Krios®

Introduction

(Thermo Fisher) microscope used in this study is additionally equipped with a C3 lens, which allows parallel illumination at different illumination sizes. Condenser lenses are complemented with their respective apertures which are basically annular metal plates restricting the electron beam to the optical axis.

The imaging system is a set of lenses creating the magnified image of the specimen. It consists of the objective lens, objective aperture, intermediate and projector lenses. The objective lens produces only moderate magnification, but the quality of its image is critical for the final resolution (Reimer and Kohl, 2008). The objective aperture located in the back focal plane of the objective lens can improve image contrast by screening out electrons scattered at high angles. The intermediate lenses between objective and projector lenses allow to project the image on the fluorescent screen or the detector and they can be operated in image mode or diffraction mode. Furthermore, they produce a wide range of magnifications.

In addition to the illumination system, deflector coils are installed in the column to allow beam tilting and shifting, so that the beam can be brought to the optical axis during microscope alignment.

While contrast in EM is created by defocus-based phase contrast, recently developed phase plates allow phase contrast generation without or with minimal defocus. A phase plate is a thin layer of carbon whole-free (Volta Phase Plate) or endowed with a 1 µm hole (Zernike-type Phase Plate). The device is installed in the back focal plane of the microscope in place of the objective aperture and functions comparable to phase plates in light microscopy. Details on image and contrast formation will be provided in 1.1.3.

The sample holder, a computerized goniometer stage is able to be shifted in x, y and z and tilted around the x-axis at a maximum angle of $\pm70°$, while cooled constantly to $LN_2$-temperature. The stage can either be accessed for sample loading by a side-entry-holder or a computerized autoloader system.

For observation of the electron beam and the specimen image, most TEMs are equipped with a phosphor coated fluorescent screen, which allows observation of the

projected image directly, or via an internal camera screening the image on a monitor. Data recording was traditionally performed on photographic emulsions and later on imaging plates which offer a wide dynamic range and high quantum efficiency but at the cost of elaborate post processing and digitization (Mori et al., 1988). Imaging plates were replaced by scintillator coupled charge coupled devices (CCD), which allow immediate digitization and thus are indispensable for tomography and automated data acquisition. For TEM applications, electrons are first detected by a thin scintillator which converts them to photons, which are then transported to the CCD array by either fiber optical or lens coupling (Krivanek and Mooney, 1993). A drawback for CCD is the limitation of resolution since the photons produced by the scintillator are detected as a cloud of light by the sensor resulting in a wide point spread function (PSF). The most recent development in electron detection generated direct electron detection devices (DDD) avoiding the need for a scintillator. DDD stand out due to detective quantum efficiency (DQE) for high spatial frequencies in particular (McMullan et al., 2014; Ruskin et al., 2013) enabling high resolution imaging and a high SNR. Furthermore, highly improved data readout speed permits frame alignment for every image acquired and thus limiting the effect of drift and sample movement (Faruqi and Henderson, 2007). Image quality can be further increased by weighing subframes according to dose accumulation during data post-processing.

Due to the high thickness of tomography samples used in this work, a Gatan post column energy filter operated in zero-loss mode was indispensable (Grimm et al., 1996; Lučić et al., 2005a). The inelastically scattered electrons, which create a blurry contrast in the final image are filtered out by the energy filter and thus SNR is increased (Grimm et al., 1997). Post column energy filters are comprised of a magnetic prism, an energy selective slit that filters out electrons outside the defined energy range and a lens to restore the final image on the detector (Krivanek et al., 1995).
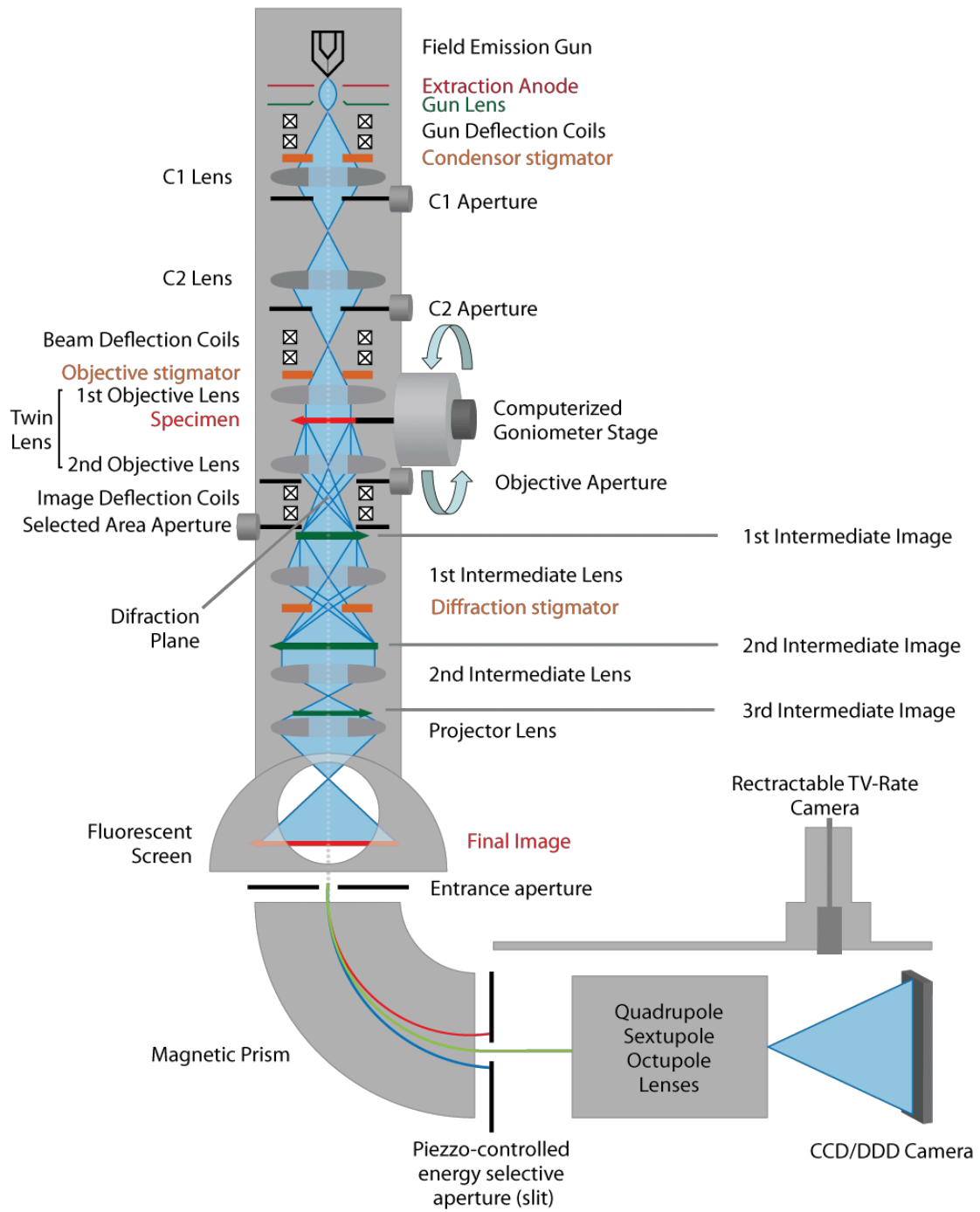
# Introduction



*Figure 1: Schematic overview of a transmission electron microscope with the beam path illustrated in blue. From* (Kochovski, 2014)

### 1.1.3 Image formation and image resolution

As mentioned in 1.1.1 electrons interact with specimen atoms in two major ways. While elastic scattering is the result of interaction of the electron with the sample atom nucleus and elicits a wide range of scattering angles, inelastically scattered electrons interact with the atomic shell and are only mildly deviated in angular distribution but undergo strong loss in kinetic energy. Elastically scattered electrons contribute to the high resolution image information, while inelastic scattering is dominated by plasmon and interband excitations and do result in image noise (Reimer and Kohl, 2008). With the low angular distribution of inelastically scattered electrons, they are not screened by the objective aperture, but thanks to the diminished kinetic energy, those electrons are filtered out by the energy filter, which is especially critical for thick samples with high electron-specimen interaction. Finally, this can highly improve image contrast. But how is image contrast generated in TEM?

Image contrast arises from the local difference in intensity of two adjacent areas or pixels in an image. In TEM image contrast is comprised of phase and amplitude contrast.

Elastically scattered electrons experience a phase shift in their wave plane while travelling the EM column and the biological sample, which is the main source of high resolution image contrast in TEM (Dubochet et al., 1988a). When imaged in defocus, the superposition of scattered and unscattered electron waves creates an interference pattern and thus creates contrast. Phase contrast depends on the objective lens spherical aberration and the defocus value and can thus be influenced by the microscope operator.

As mentioned in 1.1.2 one of the instruments used for this thesis was equipped with a VPP enabling data acquisition close to focus. Here the phase shift is the result of the beam passing a heated amorphous carbon film, which develops a beam induced volta potential (Danev et al., 2014). The VPP phase shift of around $\frac{\pi}{2}$ allows imaging close to focus (- 0.5 µm) compared to the commonly used defocus of -5 µm in tomography data acquisition.

Amplitude contrast is also called absorption contrast or scattering contrast leading to low intensity areas of the image. The effect increases with higher thickness and mass value

Introduction

of the sample, both increasing scattering of electrons passing the specimen. These highly scattered electrons are a result of interaction with the specimen atomic nuclei and are screened from the objective aperture, which leads to decreased transmitted energy. Additionally, electrons can be absorbed by the sample. Since biological samples are comprised of lipids and proteins with a low atomic number, amplitude contrast is weak and more critical for low and medium resolution imaging instead of high-resolution information.

The resolution of an instrument is its capability to separately visualize two points of an object and can be described by the Rayleigh criterion (Williams and Carter, 2009):

$$d = \frac{0.61 \cdot \lambda}{\propto}$$

with the angular aperture $\alpha$ and the wavelength $\lambda$. Consequently, the resolution of a good light microscope with a source of light in the middle of the visible field (550 nm) cannot go beyond a resolution of 300 nm (Williams and Carter, 2009). De Broglie showed that the wavelengths of electrons is related to their energy and can be described as:

$$\lambda \sim \frac{1.22}{E^{1/2}}$$

Relativistic effects are ignored here. Based on the particle-wave-duality the particle momentum $p$ of an electron can be related to its wavelength through the Planck's constant $h$:

$$\lambda = \frac{h}{p}$$

The momentum is conveyed to the electron by acceleration, imparting a kinetic energy $e$V:

$$eV = \frac{m_0 v^2}{2}$$

Replacing the momentum $p$ of the electron by the electron mass $m_0$ times its velocity $v$:

$$p = m_0 v = (2m_0 eV)^{1/2}$$

Consequently, the resolution of a TEM depends on the energy of the accelerated electrons and thus on the acceleration voltage of the microscope as follows:

$$\lambda = \frac{h}{(2m_0 eV)^{1/2}}$$

This expression illustrates that increasing the acceleration voltage decreases the wavelength of an electron. By taking relativistic effects into account, which cannot be ignored when working with acceleration voltages of 100 keV and above:

$$\lambda = \frac{h}{\left[ 2m_0 eV \left( 1 + \frac{eV}{2m_0 c^2} \right) \right]^{1/2}}$$

Electrons at this acceleration voltage reach a velocity of more than half the speed of light $c$. The microscopes used in this study were operated at 300 kV resulting in a relativistic wavelength of electrons of 0.00197 nm as can be seen in table 1.2 in (Williams and Carter, 2009).

However, the theoretical resolution of an instrument cannot be reached due to the following factors:

As in light microscopy optics aberrations of the lens system reduce the effective resolution. The spherical aberration, astigmatism, coma and chromatic aberration are the most critical errors and will be summed up below.

Spherical aberration reduces the focal length of electrons passing the objective lens off the optical axis. The difference in refraction of electrons depending on the distance from the optical axis is specific for a lens system and can be determined as the spherical aberration

Introduction

coefficient $C_S$. As electrons are not refracted homogeneously by the objective lens, the electron beam is not focused in one point but in a disc of a specific radius $r_{sa}$. The minimal resolution is limited by the spherical aberration coefficient:

$$r_{min} = 0.91 \cdot (C_S \lambda^3)^{1/4}$$

leading to $r_{min}$ of $0.7 - 1.5$ Å for high resolution instruments (Reimer and Kohl, 2008).

Astigmatism arises from the imperfect magnetic field of the lenses, which are never produced in perfect cylindrical shape and also because of the fact that microstructural incoherencies are enough to cause local variations in the magnetic field. Furthermore, contamination on apertures deflects the beam and contributes to astigmatism. This defect is corrected for by stigmators in the illumination and the imaging system (Williams and Carter, 2009).

In EM electrons spiral along the optical axis around a symmetry center. An offset in respect to the center of the electromagnetic lenses results in coma and the rotation center is not aligned correctly. For high-resolution imaging coma-free alignment is a critical step prior to imaging (Reimer and Kohl, 2008; Williams and Carter, 2009).

Chromatic aberration results from the difference in scattering angles of different electron wavelengths by the objective lens, since electrons with lower energy are scattered more strongly. Consequently, electrons from one object point are once more (as for spherical aberration) projected into a disc with a specific diameter:

$$r_{chr} = C_c \frac{\Delta E}{E_0} \beta$$

with $C_c$ as the chromatic aberration coefficient, $E_0$ the initial energy of the electron and $\beta$ is the semiangle of collection of the lens.

### 1.1.4 Sample preparation for cryo-electron tomography

Considering the high rate of evaporation of water from native samples in high vacuum conditions, a method of fixation is indispensable. Conventionally EM-samples are dehydrated by gradually replacing cellular water with ethanol and embedding in epoxy resin. Embedded specimens are sectioned and treated with heavy metal staining. All these steps dislodge the biological specimen from its native state.

Cryo-preservation makes use of the fact that native samples immersed in an aqueous solution can be rapidly ($10^5$ °C/sec in 20 μm depth of sample) frozen, leaving them in vitrified or amorphous ice, thus avoiding formation of ice crystals (Dubochet et al., 1988b). After initial experiments of cryo-fixation of catalase crystals (Taylor and Glaeser, 1974) vitrification by direct contact with a cryogen became more and more of use. The ideal cryogens proved to be ethane and propane close to their melting points. The sample sits on an EM grid and is rapidly immersed in ethane/propane with the help of a plunging device to ensure direct contact of liquid cryogen and liquid film. Liquid ethane and propane have proven to be perfect cryogens for vitrification, since both can be warmed up by 100°C without evaporation. Consequently the process of calefaction, which creates a layer of evaporating gas and thus insulation around the sample is avoided (Dubochet et al., 1988b). After plunge freezing EM-grids are stored in liquid nitrogen until they are transferred to the microscope. The sample temperature must not exceed -135°C to avoid formation of cubic ice, which is detrimental to the native structure (Fernández-Busnadiego and Lučić, 2012). Thus, a vitrified specimen maintains a fully hydrated native structure without reorientation or aggregation of proteins and including smooth and continuous membranes.

### 1.1.5 Cryo-electron tomography data acquisition

Cryo-TEM permits the direct observation of two-dimensional projections of the transmission image of thin biological samples without fixation or staining artifacts. Thanks to digitized data acquisition and elaborate image processing, three-dimensional information of the sample can be fathomed. Both available methods, single particle analysis (SPA) and cryo-electron tomography (CET) rely on the computational reconstruction of 2D-projection images.

Introduction

In SPA, purified particles of a protein or protein complex are vitrified at a concentration which allows high SNR-imaging and at the same time recording of micrographs with multiple copies of the complex in different orientations. Particles have to be extracted from projection images ideally representing all orientations equally. Extracted particles are aligned and reconstructed to a 3D-model iteratively until a stable resolution has been established (Nogales and Scheres, 2015). Recently near atomic resolutions could be achieved by SPA revealing subtle conformational changes in proteins (Unverdorben et al., 2014; Wehmer et al., 2017). Furthermore, so far unsurpassed size limitations for the analyzed particle have become amenable by SPA using the VPP (Khoshouei et al., 2017).

In CET, a series of projection images is recorded from a typically more complex sample like cell organelles or cellular fractionations. The sample is imaged at different orientations by tilting the computerized stage around a tilt axis. These projection images are then computationally aligned and reconstructed to produce the final tomogram (see Figure 2). Due to limitations of the instrument, the tilt range can reach a maximum of ±70° , but imaging is practically limited to ±60° due to the increasing sample thickness with increasing tilt angles.
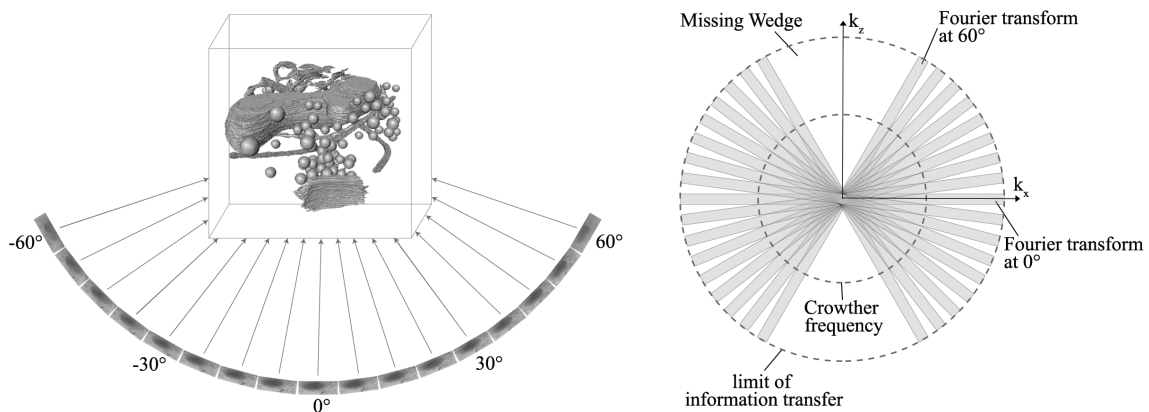


*Figure 2: Principle of tomography:*

*Transmission images are acquired from -60° to 60° in according to individual tilt schemes (see text). Projection images are aligned and computationally back projected into a 3D-volume (left). Each projection is represented by a thin slice in Fourier space with continuous sampling until the Crowther frequency. Due to the limited tilt range an unsampled volume, the missing wedge, is inevitable (right).*

The most common angular increment scheme is the constant increment scheme with increasing electron dose at higher tilts, as compared to the Saxton scheme, which aims to compensate for higher thickness in higher tilt angles with decreasing tilt increments (Saxton et al., 1984). While tomograms have conventionally been recorded in two separate series (e.g. 0° – 60° and -2° – -60°) or in one stretch from the negative to the positive maximum tilt, it recently became possible to record dose symmetrical tilt series (Hagen et al., 2017). Compared to a continuous or a bidirectional tilt scheme, the dose-symmetric tilt scheme profits from the fact that the electron dose the sample is exposed to is weighted on the low tilt images, since the series begins at 0° tilt alternating between increasingly negative and positive tilts.

The chosen tilt increment $\Delta\alpha$ directly influences the isotropic resolution d of a tomogram, which can be described by the Crowther criterion (Crowther et al., 1970):

$$d = D\Delta\alpha$$

assuming the sample do be a cylinder of diameter *D*.

Due to the limitations of sample tilting, an object can never be sampled completely. Since each projection image is represented in the Fourier space as a slice perpendicular to the optical axis of the microscope, every tomogram has a wedge-shaped region in the Fourier space where the structural information is missing (Fernández-Busnadiego and Lučić, 2012). To narrow down the missing information, dual-tilt tomography was developed, by tilting the sample around a second tilt axis perpendicular to the first and recording two series of images.

As mentioned above the biological sample is highly sensitive to the electron beam. The maximum tolerable dose depends on the sample and also on the intended resolution. To accomplish a high SNR the maximum electron dose tolerable by the specimen ($\sim 100$ $\text{Å}^{-2}$) has to be fractionated for each projection image, defined by the exposure time of each projection during automated data acquisition. This acquisition strategy is furthermore enriched by the so-called low-dose-mode, allowing to correct for errors in positioning and focusing without additional exposure to the specimen (Koster et al., 1997). In this mode

additional images are acquired in some micrometer distance from the area of interest without dissipating more electron dose on the latter.

Despite very stable instrumentation, the tilt series has to be properly aligned before reconstruction to compensate for imperfect tilting or translations in the image plane. For that purpose, high-contrast gold fiducial markers are added to the specimen and can be tracked automatically during the software-based postprocessing. Subsequently the tilt series images are projected into 3D-space by weighted back-projection, while correcting for the uneven radial distribution of information in the Fourier space that this reprojection causes (Fernández-Busnadiego and Lučić, 2012; Radermacher, 2006).

## 1.2   Analysis of mammalian neuronal processes and synapses by cryo-electron tomography

Throughout the development of super-resolution microscopy and the ongoing achievements in high-resolution cellular cryo-electron microscopy as well as live-cell imaging neuronal cells have always been a much sought-after target. It has been a central challenge in neuroscience to investigate the dynamic organization of synapses in its development and during stages of plasticity. While it is possible to identify presynaptic boutons and postsynaptic spines by diffraction-limited light microscopy, the functional domains of the synapse remain elusive. The same is true for axonal processes which are less than 200 nm in diameter. The complex organization of organelles and proteins in the synaptic compartments and in neuronal processes have remained unexplored until further development of imaging techniques. Super-resolution microscopy methods like STED (stimulated emission depletion) microscopy of living neurons demonstrated features of synaptic subdomains including vesicular mobility during exo- and endocytosis as well as during formation of vesicle clusters (Kamin et al., 2010; Westphal et al., 2008). Three-dimensional STORM (stochastic optical reconstruction microscopy) imaging allowed the nanoscale localization of synaptic proteins at a maximal spatial resolution of 15 nm in fixed mouse brain sections (Dani et al., 2010). Despite these methods giving great insight into neuronal organization, both are limited in resolution compared to CET and most importantly rely on labelling of protein targets. Consequently, the observation of neuronal cells by CET

is a crucial step towards elucidating the molecular organization in synapses and axonal processes in a fully hydrated unstained environment.

The method of sample preparation from neuronal tissue for CET is not at all trivial. While organotypic hippocampal rat slices provide an insight into neuronal structure in physiological environment, they require cryo-sectioning due to their thickness and thus sectioning artefacts cannot be avoided (Garvalov et al., 2006; Zuber et al., 2005). Primary cultured neuronal cells form a thin layer as well as an interconnecting network of neuronal processes on the EM grid and thus are a suitable system to study synaptic connections and axonal transport processes (Fernández-Busnadiego et al., 2011; Fukuda et al., 2015; Lučić et al., 2007). If the structural analysis is focused on synaptic connections, synaptosomes are a system of choice. The isolated synapses obtained from brain tissue homogenate by fractionation allow pharmacological treatment and also functional studies on transmitter release (Fernández-Busnadiego et al., 2010; Lučić et al., 2005b; Whittaker, 1993). While primary cultured neurons provide a physiologically intact system to visualize both neuronal processes and synapses, the latter are extremely hard to localize in TEM. Furthermore, mature synapses may exceed the maximum thickness feasible by CET and thus have to be thinned by focused ion beam-milling (Fukuda et al., 2015). Synaptosomes on the other hand are physiologically intact for several hours (Dunkley et al., 2008) and provide a rather pure sample of synaptic terminals and are thus suitable for statistical analysis of synaptic organization. For those reasons both primary cultured neurons and synaptosomes were the specimen objects in this thesis.

### 1.2.1 Basic structure of synapses

Synapses are specialized junctions between neurons or between neurons and other excitable cells, which transfer signals with high spatial precision and speed (Cowen et al., 2001). While the electrical synapse is comprised of a gap junction between neurons allowing a bidirectional signal (Bennett, 2000), in the chemical synapse the presynaptic electrical signal is converted into a secretory response leading to the release of a chemical transmitter into the synaptic cleft. The transmitter binds postsynaptic receptors and opens ion channels, thus reconverting the chemical signal into an electrical postsynaptic response. For both main types of synapses, excitatory, mainly glutamatergic synapses as well as inhibitory, that are mainly GABA (γ-aminobutyric acid) -ergic, the main structural feature is the close

apposition of the highly specialized plasma membrane segments. While the presynaptic bouton is endowed with transmitter filled synaptic vesicles (SV), the postsynaptic density (PSD) represents an accumulation of neurotransmitter receptors and a sub-membranous dense protein filament network. The presynapse shows unique features to cope with the large distance between cell body and location of protein synthesis and the specialized location of secretion by being capable of resupply of SVs by recycling (Cowen et al., 2001). The presynaptic vesicle cluster consists of up to several hundred SVs (Harris and Sultan, 1995) with a size around 40 nm in diameter and endowed with a clear lumen. In large synaptic terminals a single presynapse is connected by more than one PSD independently. At each of these contacts vesicles are engaged at an active zone (AZ), the site of vesicle release, which will be explained in chapter 1.2.2. Additionally presynaptic terminals contain endocytotic intermediates such as clathrin-coated pits and pleiomorphic membrane compartments (Heuser and Reese, 1973), usually well separated from vesicle clusters, indicating segregation of exo- and endocytosis. After maturation from early endosomes small multi-vesicular bodies (late endosomes) can occasionally be observed and are destined to delivery to lysosomes after retrograde axoplasmic flow (Tsukita and Ishikawa, 1980). Furthermore, TEM-images reveal membrane profiles that can be identified as smooth endoplasmatic reticulum (SER) stretching throughout dendrites to nerve terminals. The main role of the SER is the storage of internal $Ca^{2+}$, which is releasable via the generation of IP$_3$ (inositol-1,4,5-trisphosphate) acting on IP$_3$-gated $Ca^{2+}$-channels in the SER-membrane. While this increase in $Ca^{2+}$-concentration is not critical for exocytosis it enhances the efficiency of depolarization-secretion coupling and induces release of large dense core vesicles (Nicholls, 1998). As many steps of the vesicle cycle inside the presynaptic terminal require ATP such as vesicle priming for release, clathrin-uncoating, and the uptake of transmitter into SVs, mitochondria can be found in close proximity to the AZ (Cowen et al., 2001). The electron dense synaptic cleft is endowed with extracellular domains of proteins keeping the pre- and postsynaptic membranes in register and are also critical for synapse formation after the induction of cell adhesion as an initial step (Robbins et al., 2010).

## 1.2.2 The presynaptic release machinery

The presynaptic active zone allows fusion and exocytosis of neurotransmitter within less than 1 ms of the $Ca^{2+}$-influx into the presynaptic terminal, thus requiring a highly

specialized and efficient release machinery (Südhof, 1995). Synaptic transmission is induced when an electro-chemical membrane potential, the action potential, arrives at the presynaptic terminal. The depolarization of the synaptic membrane opens up voltage-gated $Ca^{2+}$-channels and elicits $Ca^{2+}$-influx into the synaptic terminal. As a consequence, the $Ca^{2+}$-sensitive system of proteins assists primed SVs to fuse with the presynaptic membrane and release neurotransmitter into the synaptic cleft (Südhof, 2004). At rest, synapses have a low probability of release causing electrophysiological measurable recordings of miniature postsynaptic currents. Upon activity, evoked SV release is SNARE-dependent. The complex is a composition of the vesicle-bound protein synaptobrevin and syntaxin-1 and SNAP-25 at the plasma membrane. Additionally synaptotagmin-1 (Syt-1) interacts with both membranes and the SNARE complex (see Figure 3 C), as well as complexin, building the SNARE-synaptotagmin-complexin complex collaborating for vesicle fusion (Zhou et al., 2017). Synaptotagmin-1 contains two $C_2$ domains and is generally believed to be the calcium sensor for synchronous evoked exocytosis (Fernandez-Chacon et al., 2002; Mackler et al., 2002). Due to their differential localization within the nerve terminal membranes, synaptobrevin is termed v-SNARE (vesicle SNARE) while syntaxin-1 and SNAP-25 are termed t-SNAREs (target SNAREs; (Hanson et al., 1997)). Vesicles in this fusion-competent, primed state represent what is termed the readily releasable pool (RRP). Each synapse holds about 12 RRP quanta which need about 10s time for replenishing (Rosenmund and Stevens, 1996). But how is this critical step of SV priming controlled?
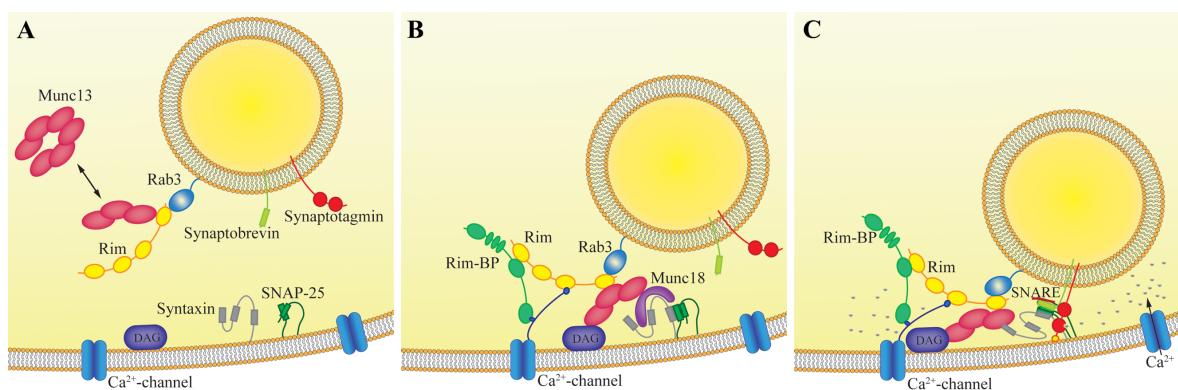


*Figure 3: The priming complex.*

**A**: *The homodimer of Munc13 is activated and becomes engaged with the RIM1α-Rab3-complex.* **B**: *Rim1α directly and indirectly via RIM-BP interacts with Ca2+-channels. Munc13 is anchored to the presynaptic membrane via DAG and can thus interact with t-SNARES.* **C**: *Munc13 binds syntaxin-1 and thus dissociates it from Munc18, which keeps it in an inactive conformation. The Calcium sensor synaptotagmin-1 and Munc13 assist the formation of the SNARE complex, setting up the SNARE-synaptotagmin-complexin (red) complex. Synaptotagmin is bound via PIP$_2$ (orange) to the presynaptic membrane.*

Introduction

The plasma membrane protein syntaxin-1 is the coordinator of the priming process, but syntaxin-1 needs to be in the active conformation to perform this priming function. The N-terminal domain of syntaxin binds to several proteins that are essential for synaptic vesicle exocytosis, namely Munc18-1 and Munc13-1 (Südhof, 1995). Homologues of mouse Munc13-1 exist in *Drosophila melanogaster* (Dunc13) and *C. elegans* (Unc13) demonstrating the central role of Munc13 in the priming process (Silinsky and Searl, 2003). Also, Munc13-1 deficient synapses show no morphological changes but lack fusion-competent SVs (Augustin et al., 1999), indicating that Munc13-1 is dispensable for synapse formation but critical for SV priming. While four isoforms of Munc13 exist (Munc13-1, bMunc13-2, Munc13-3 and ubMunc13-2), Munc13-1 is the most dominant isoform in the brain (Junge et al., 2004) and all isoforms will in the following thesis be referred to as Munc13. Preceding to priming, syntaxin-1 is maintained in an inactive conformation by its association with Munc18, but may be dissociated by binding of Munc13 to the N-terminus of syntaxin-1. The Munc13 – syntaxin interaction serves to initiate the assembly of the primed core complex (Betz et al., 1997). Additionally, Munc13 binds RIM1$\alpha$, the Rab3-interacting molecule (see Figure 3), which recruits Munc13 by opening up the inactive Munc13 homodimer (see Figure 3 A) (Lu et al., 2006). Consequently, a complex of Munc13-RIM1$\alpha$-Rab3 is formed (see Figure 3 B) and mediates SV priming (Deng et al., 2011). RIM1$\alpha$ interacts with $Ca^{2+}$-channels directly and via the RIM-BP (RIM binding protein) and thus attracts $Ca^{2+}$-channels to the AZ (Acuna et al., 2015; Han et al., 2011; Kaeser et al., 2011). RIM1$\alpha$ interacts also with SNARE-complex protein SNAP-25 and synaptotagmin-1 and is thus involved in synaptic vesicle priming and synaptic plasticity (Coppola et al., 2001). Rab3 is a vesicle associated small GTP-binding protein, which negatively regulates vesicle fusion since its depletion enhances neurotransmitter release without changing tethering of SVs (Coppola et al., 2001; Geppert et al., 1997). Furthermore, Munc13 is binding to Piccolo, a large protein which acts together with Bassoon on scaffolding and organization of the AZ, is associated with F-actin and influences SV dynamics (Torres and Inestrosa, 2017). Besides, both proteins regulate synaptic degradation since they interact with the E3 ubiquitin ligase Siah1, inhibiting ubiquitination and proteasome degradation (Waites et al., 2013).

From all central players of the presynaptic release machinery only a few and well known have been described here. Munc13 with its multiple binding partners is essential for vesicle priming and is thus of central interest for this study.

### 1.2.3 Pharmacologically induced short-term facilitation

During repetitive stimulation of the synapse the presynaptic strength changes rapidly together with intracellular signaling pathways (de Jong and Verhage, 2009; Zucker and Regehr, 2002). The diacylglycerol (DAG)/protein kinase C (PKC)-dependent cascade is one of the most potent ways in the presynaptic terminal to increase synaptic strength by 50-100% for both spontaneous and evoked (AP-dependent) transmitter release (Lou et al., 2005; Malenka et al., 1986; Shapira et al., 1987).

Munc13 is a key player in SV priming and it is critical for the fusion competence of the readily releasable pool (RRP), which was impressively shown by (Augustin et al., 1999) for the Munc13-1 isoform. Depletion of the brain-specific isoform leads to a 90% decrease in glutamate release, while the following application of sucrose, typically used for RRP size estimation, leads to a quantifiable asynchronous glutamate discharge. With Munc13 isoforms seem to be critical for SV priming, deletion of the most prevalent isoform in the brain did not result in morphological changes of the AZ or reduction of SV numbers despite the dramatic reduction in transmitter release (Tokumaru and Augustine, 1999). Thus, Munc13 KO mutants are firstly an unsuitable source of synaptosomes, since DKO mutants of Munc13-1 and -2 isoforms show a lethal phenotype (Varoqueaux et al., 2002). In that case, samples have to be prepared from non-lethal developmental stages such as rodent embryos. Secondly as mentioned above, the ultrastructure is known to reveal a synaptic phenotype with physiological features missing primed SVs. Consequently, triggering SV priming via activation of Munc13 can be expected to provide a more interesting ultrastructural insight into SV priming and maturation for transmitter release.

Munc13 is comprised of several domains including the MUN module responsible for the interaction with syntaxin-1 mentioned above. MUN can extract the SNARE motifs out of the syntaxin-1-Munc18 inhibitory complex and thus assists SNARE-complex formation (Ma et al., 2011). Other domains of Munc13 function synergistically to induce vesicle priming. Close to the N-terminus, most isoforms include a $C_2$-domain ($C_2$A-domain), a $C_2$B-

domain that regulates release probability and modifies short term plasticity through its $Ca^{2+}$- and phosphatidylinositolphosphate-binding activities, a $C_2C$-domain that is also important for release and finally a $C_1$-domain involved in DAG/phorbol-ester dependent augmentation of release (Liu et al., 2016). In the synaptic terminal the $C_1$-domain is binding DAG as a final step of a G-protein dependent signaling pathway. By activation of this classical G-protein pathway, phospholipase C (PLC) is produced. It acts on phosphatidylinositol-4,5-biphosphahte (PIP$_2$) and produces diacylglycerol (DAG) and inositol triphosphate (IP$_3$). This process generates an increase in intracellular $Ca^{2+}$ that activates $Ca^{2+}$-dependent proteins (Torres and Inestrosa, 2017) but most importantly membrane bound DAG binds the $C_1$-domain of Munc13 and thus anchors it to the presynaptic membrane (see Figure 6).

To activate Munc13 in synaptosomes, two chemical compounds have been used for pharmacological manipulation of neuronal samples; L-AP4 and PDBu. L-AP4 binds metabotropic glutamate receptors, a G-protein coupled receptor (GPCR) located at the presynaptic membrane and acting as an autoinhibiting receptor mediating feedback inhibition of glutamate release (Forsythe and Clements, 1990; Gereau and Conn, 1995) by deactivation of $Ca^{2+}$-channels (Millán et al., 2002). A prolonged exposure to the agonist L-AP4 results in activation of G-protein dependent signaling pathway producing DAG mentioned above (Martín et al., 2010). To directly induce Munc13-translocation to the presynaptic membrane DAG can be replaced by 4-β-phorbol-12,13-dibutyrate (PDBu) (Parfitt and Madison, 1993).
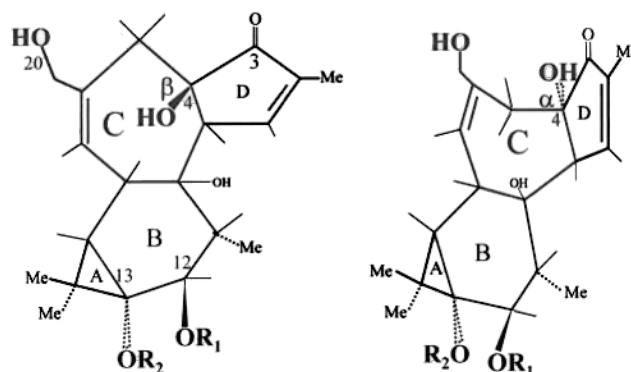


*Figure 4: Active (left) β-phorbol and inactive α-phorbol (right).*

*The phorbols are 4-ringed compounds (rings A-D). The two forms differ in the position of the OH-group in ring D at position 4 with the OH-group in β-position for the active form and in α-position for the inactive form. Modified from (Silinsky and Searl, 2003)*

The general structure of active phorbols (β-phorbols) is shown in Figure 4. The phorbols contain four rings depicted in Figure 4 as A-D. In the active β-phorbols, the hydroxy group is in the β-position, while in the inactive phorbols, the hydroxy group is in the α-position. Both forms are lipophilic, but only the β-form used in this study has a biological effect.
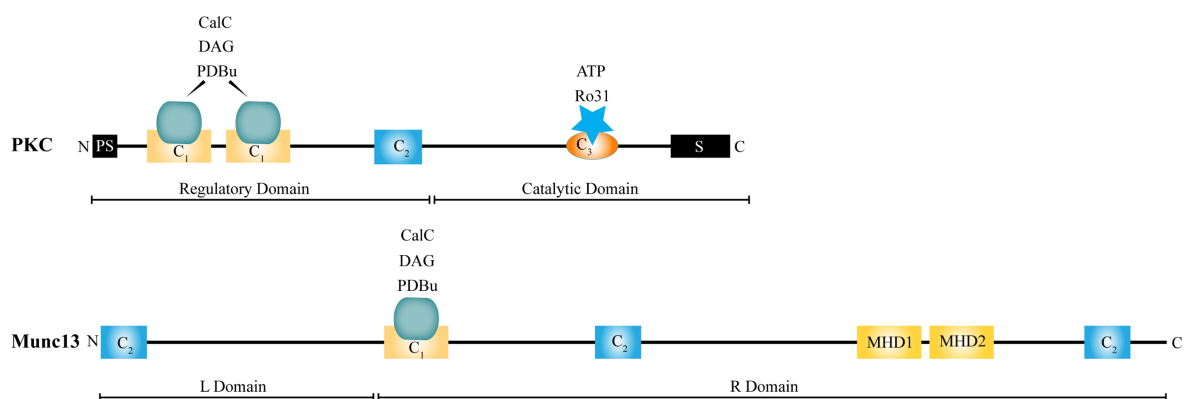


*Figure 5: Binding domains of PKC and Munc13.*

*The important domains of classical PKCs are comprised of the pseudo-substrate binding domain (PS) of the regulatory domain, which interacts with the catalytic domain in the inactive form of the enzyme. Two $C_1$-domains for interaction with DAG or phorbols and also the binding domain of CalC, one of the inhibitors used in this work. $C_2$ domains, present in PKC and Munc13 bind $Ca^{2+}$ as well as phospholipids. The $C_3$-domain is the ATP binding site and inhibited by Ro31. The substrate binding domain is located at the C-terminal region of the catalytic domain. Munc13 isoforms have the highly conserved R-region in common, binding most active zone binding partners (but Rim) and also PDBu/DAG at the $C_1$-domain.*

Phorbol esters such as PDBu bind the same $C_1$-domain of Munc13 as DAG and thus serves as a stable DAG-substitute (see Figure 5). The purpose of the $C_1$-domain is to help recruit proteins to membranes. The upper part of this domain holds a strategic region containing two β-sheets which separate a water-filled cavity. After displacing a molecule of water, the phorbol esters fit into this cavity (Silinsky and Searl, 2003). The binding of phorbols in the $C_1$-domain provides a hydrophobic cover allowing the complex to be inserted and anchored into membranes with little conformational change (Zhang et al., 1995). Phorbol esters are known to have myriad of physiological effects on cells and tissues, the most commonly observed being tumor growth (Nishizuka, 1988). The main target to mammalian tumor growth is calcium-and phospholipid-dependent protein kinase (PKC) and indeed PDBu is not only activating Munc13 but also PKC (Newton, 1995) in a very potent way compared to DAG due to its high stability in cells (Mosior and Newton, 1995). The $C_1$-ligand additionally markedly reduces the concentration of $Ca^{2+}$ required for the

Introduction

phosphatidylserine-dependent activation of PKC (Walker et al., 1990). The direct activation of PKC has been shown to potentiate synaptic transmission by increasing the release of glutamate by multiple mechanisms including the upregulation of $Ca^{2+}$-channel activity (Parfitt and Madison, 1993), the inhibition of $K^+$-channels (Zhang et al., 2001) or by augmenting the $Ca^{2+}$-sensitivity of the release machinery (Wu and Wu, 2001).

To ensure the tomographic data of this study does represent the influence of PDBu on Munc13 as a SV priming factor as opposed to the activation of PKC and its substrates, two antagonists of PDBu were included in the experimental setup (see Figure 6). Calphostin C (CalC) inhibits the binding of phorbols to the $C_1$-domain of Munc13 as well as PKC, inactivating the latter irreversibly by free radical production and destruction of the kinase after photoactivation (Gopalakrishna et al., 1992; Sossin, 2007). Ro31, a staurosporin is a competitive ATP-binding site inhibitor, which has no effect on the binding of PDBu (Tamaoki et al., 1986) and thus only inhibits the activation of PKC and does not influence the PDBu-dependent translocation of Munc13. The bisindolylmaleimide BID1 has the same binding affinity and the identical ATP-competitive inhibitory effect as the staurosporine Ro31 and was used additionally in some experiments (Wilkinson et al., 1993).
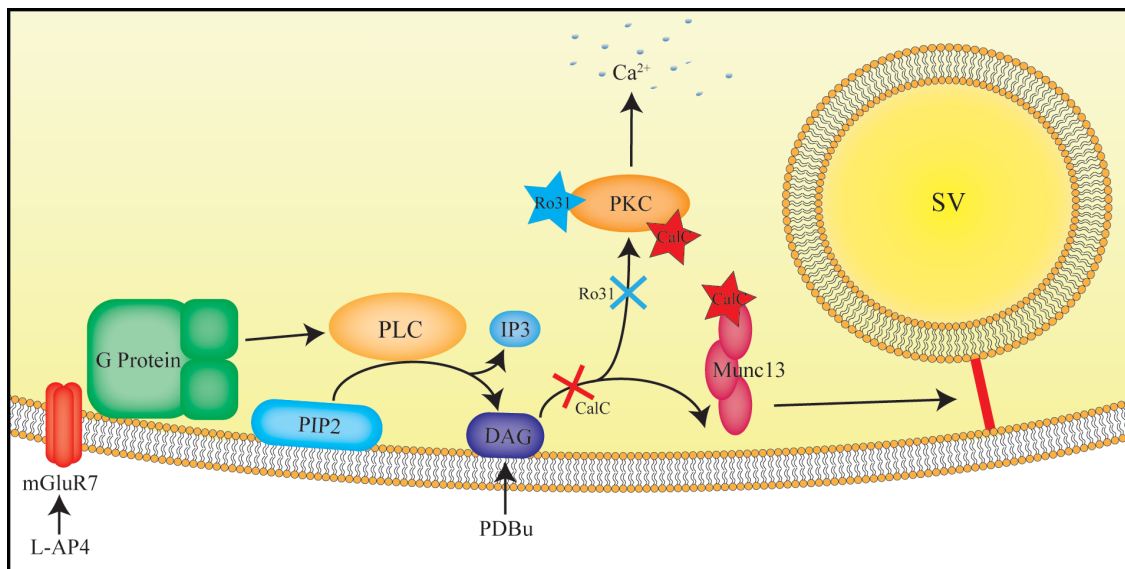


*Figure 6: G-protein pathway with the central players mGluR7 and DAG, which were to be pharmacologically activated by L-AP4 or substituted by PDBu in this project. The inhibitory role of the antagonists CalC and Ro31 is illustrated with binding affinities.*

# 2. Aim of this work

Cryo-electron tomography is a powerful tool to observe biological samples in the fully hydrated and unfixed state. While multiple studies on the structural analysis of synapses, and specifically pools of synaptic vesicles, do exist for conventional electron microscopy and dehydrated specimen, no data is available exploring the features of specific synaptic vesicle pools in native synaptic samples. The readily releasable pool is comprised of vesicles primed for the release of neurotransmitter into the synaptic cleft after fusion of the vesicular and the presynaptic membrane. In conventional preparations, this pool was defined as vesicles that are "docked" to the active zone membrane with direct contact of vesicle and presynaptic membrane before fusion. However, direct contact between vesicles and the AZ membrane is likely a dehydration artefact, because it is not observed in CET. The pharmacological manipulation of synapses that cause Munc13 translocation and vesicle priming is helpful to visualize the readily releasable pool. Furthermore, an elaborate statistical analysis of filaments interconnecting synaptic vesicles will be performed for synaptosomes in this state. With the help of phorbol ester PDBu and its antagonists, the role of not only Munc13 but also PKC in release facilitation will be examined. Thus, the currently unexplored structural features of the native synaptic active zone in the state of release potentiation will be examined here. Additionally, the analysis of primary cultured neuronal processes and synapses after focused ion beam milling with pharmacological treatment of the latter was central goal of this thesis.

# 3. Materials and methods

## 3.1 Sample preparation

Biological Samples were cortical or hippocampal neuronal cells derived from Wistar rats, which were either isolated for preparation of isolated synaptic terminals or used for primary neuronal culture. Both sample types were vitrified after pharmacological treatment or in native state. Depending on the experimental goal, some samples were thinned using ion milling. The detailed methods are described in the following chapter.

### 3.1.1 Synaptosomal preparation

Isolated synaptic connections were derived from cortical tissue of six to eight weeks old Wistar rats as described in Dunkley et al. (Dunkley et al., 1988, 2008). Animals were anesthetized with chloroform and decapitated according to the guidelines of the Max-Planck-Institute of Biochemistry. The cortex was quickly extracted over ice and transferred to a minimal volume of ice-cold homogenization buffer (HB: 0.32 M sucrose with 1 tablet of Complete mini EDTA-free protease inhibitor cocktail (Roche) per 10 ml buffer, pH 7.4) and homogenized with a motor driven Teflon piston at a speed of 700 rpm. The homogenate was centrifuged at 4 °C for 2 minutes at 2000 g in an SS-34 rotor (Sorvall). The supernatant (S1) was transferred to a fresh tube and the pellet (P1) was resuspended in HB and centrifuged at 2000 g at 4 °C for 2 minutes. Pellet S2′ was discarded; the supernatant S1′ was combined with S1 and spinned 9500 g for 12 minutes at 4 °C. Supernatant S2 was discarded and P2 was resuspended in minimal volume of HB. The suspension was transferred gently onto a three-step Percoll (GE Healthcare) gradient with the concentrations of 23%, 10% and 3% with a maximum volume of 1 ml suspension per gradient. Gradients were centrifuged in a Beckmann ultracentrifuge at 25000 g at 4 °C for 6 minutes in a 75 Ti rotor. The synaptosome rich layer between 10% and 23% Percoll was retrieved with a Pasteur pipette and diluted in 50 ml of Hepes-buffered medium (HBM:140 mM NaCl, 5 mM KCl, 5 mM NaHCO$_3$, 1.2 mM NaH$_2$PO$_4$-H$_2$O, 1 mM MgCl$_2$-6H$_2$O, 10 mM Glucose, 10 mM Hepes, pH 7.4). To wash out Percoll, synaptosomes were centrifuged at 22000 g for 10

minutes at 4 °C and diluted in HBM to a final concentration of 0.7 mg/ml, as determined by Protein-UV (Implen Nano Photometer). Suspension was split into several Eppendorf tubes with a volume of 1 ml each and spinned down again at 10000 g for 10 minutes. The supernatant was discarded, and pellets were kept on ice until incubation time (1 hour at 37 °C) but for a maximum time of 4 hours.

During the course of this experiments I tested the possibility to cut down the protocol for synaptosome preparation by omitting separation of the solution by Percoll gradient. P2 was the final sample in this case, brought to a protein concentration of 1 mg/ml and was vitrified.

### 3.1.2 Pharmacological treatment of synaptosomes

Synaptosomes were pharmacologically treated during the 1 hour-incubation time according to the following table:

*Table 1: Pharmacological treatment scheme of Synaptosomes*

| Substance | Incubation time | Concentration |
|---|---|---|
| Phorbol-12,13-dibutyrate (PDBu) | 5 minutes | 1 µM |
| L-(+)-phosphonobutyrate (L-AP4) | 10 minutes | 1 mM |
| Calphostin C (CalC) | 30 minutes | 0.1 µM |
| Ro31-8220 | 30 minutes | 0.1 µM |
| Bisindolylmaleimide 1 (BIM-1) | 30 minutes | 1 µM |

Incubations were stopped by vitrification of the sample on copper grids.

### 3.1.3 Preparation of membranous and cytosolic fractions

To analyze proteomics of synaptosomal membranes and cytosol synaptosomes were split into corresponding fractions.

Materials and methods

Synaptosomes of the density of 0.7 mg/ml were either treated as control sample or treated with L-AP4 for translocation of Munc13-1 to the presynaptic membrane. Samples were incubated at 37 °C according to the following scheme (Ferrero et al., 2013).

*Table 2: Incubation scheme for Synaptosome Fractionation*

| Buffer/Substance | Incubation time | concentration |
|---|---|---|
| HBM/BSA | 30 minutes | 16 µM |
| HBM/ADA | 20 minutes | 1.25 u/mg protein |
| HBM/L-AP4 | 10 minutes | 1 mM |

Incubation in bovine serum albumine (BSA) serves to bind fatty acids released from synaptosomes (Ferrero et al., 2011). Adenosine deaminase (ADA) converts extracellular adenosine to inosine to inhibit binding of adenosine to presynaptic glutamatergic receptors. After incubation, synaptosomes were washed by centrifugation at 13000 g for 1 minute and resuspended in hypo-osmotic Tris-HCl-buffer (8.3 mM, pH 7.4) to a protein concentration of 2 mg/ml with 1 tablet of Complete mini EDTA-free protease inhibitor cocktail (Roche) per 10 ml buffer. The Synaptosomal suspension was passed through a 20-gauge syringe to disaggregate synaptosomes and maintained at 4 °C with gentle shaking. To separate membrane and cytosolic fractions the suspension was centrifuged at 40000 g for 10 minutes in a Beckmann ultracentrifuge in a 75 Ti rotor. The supernatant was collected (cytosolic fraction) while the pellet (membrane fraction) was resuspended in radioimmunoprecipitation assay (RIPA) buffer (Martín et al., 2010) (50 mM Tris-HCl, pH7.4, 100 mM NaCl, 1% Triton X-100, 0.5% sodium deoxycholate, 0.2% SDS, and 1 mM EDTA).

Soluble and particulate fractions were analyzed with SDS-PAGE, Western Blotting and vitrified for Cryo Electron Microscopy.

### 3.1.4 Viability assays of synaptosomes

After preparation of synaptosomes, the biological material is presumably viable and physiologically active within 4 hours when kept at 4 °C. To verify viability of synaptosomes, two assays were conducted; the glutamate release assay and synaptic vesicle endocytosis analysis (Daniel et al., 2012).
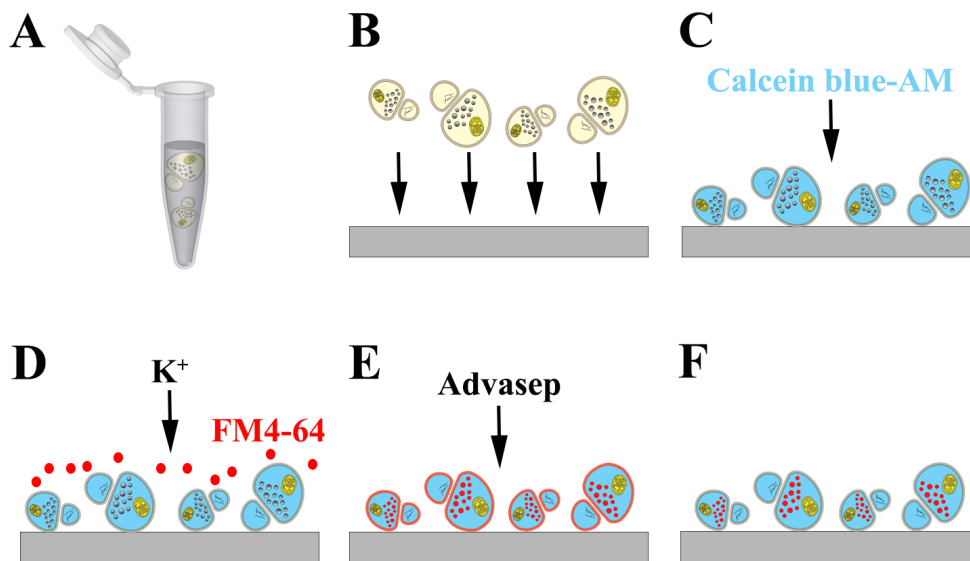
*Figure 7: The high-throughput SVE assay.*

*A: Solution of synaptosomes freshly prepared or thawed after freezing is suitable for the assay. **B**: Synaptosomes are pipetted on a PEI-coated objective slide with plastic wells (μ-Slide 8 Well, Ibidi, Planegg, Germany) and spinned at 1,500 g for firm attachment to the surface. Samples can be washed with buffers repeatedly without dissolution. **C**: Calcein blue-AM stains the cytosol. **D**: FM4-64 is applied exclusively for controls or together with $K^+$ and internalized during endocytosis of SV. **E**: Outer membranes are equally stained by the FM-dye requiring destaining with Advasep-4. **F**: Samples are ready for fluorescence imaging.*

For analysis of synaptic vesicle endocytosis (SVE), synaptosomes were prepared as described above replacing HBM for Percoll wash by Sucrose/EDTA/Tris (SET) buffer (0.32 M sucrose, 1 mM EDTA, 5 mM Tris; pH 7.4). Synaptosomes can be kept frozen after preparation and until SVE assay as mentioned in Figure 7 (step A). Microscopy slides equipped with 8 wells (μ-Slide 8 Well, Ibidi, Planegg, Germany), were coated with Polyethylenimine (PEI, Merck, Darmstadt, Germany) solution in a 1:15000 dilution by incubating the solution over night at 37 °C in the dark. After coating, slides were dried and cooled until synaptosome preparation. Isolated synaptosomes were diluted to a protein concentration of 20 µg/ml in SET buffer with 250 µM Dithiotreitol (DTT, Merck, Darmstadt, Germany) and transferred to the wells of the chilled microplate. The microplates were attached to a bucked adaptor of a benchtop centrifuge (Rotanta 460R, Hettich, Tuttlingen, Germany) and spinned at 1500 g for 30 minutes at 4 °C (step B in Figure 7).

Attached synaptosomes were prepared for labelling with Calcein blue-AM (Merck, Darmstadt, Germany) by changing the medium from SET buffer to Hepes-buffered Krebs-like buffer (143 mM NaCl, 4.7 mM KCl, 1.3 mM MgSO$_4$, 1.2 mM CaCl$_2$, 20 mM Hepes,

Materials and methods

0.1 mM $NaH_2PO_4$ and 10 mM D-Glucose; pH 7.4) warmed up to 30 °C. Slides were incubated for 15 minutes at 30 °C to allow the synaptosomes to recover from low-temperature conditions and to regenerate ATP levels and membrane potentials. For staining, buffer was replaced by HBK with 1 µM Calcein blue-AM and incubated for 30 minutes at 30 °C in the dark (step C in Figure 7). Calcein blue-AM enters the synaptosomes where esterases will cleave off the acetoxymethyl (AM-) group, leaving the fluorescent Calcein blue trapped inside the synaptosomes (Daniel et al., 2012).

For FM4-64 ((*N*-(3-Triethylammoniumpropyl)-4-(6-(4-(Diethylamino) Phenyl) Hexatrienyl) Pyridinium Dibromide, Thermo Fisher, Waltham, USA) staining, two solutions were prepared: Solution 1 is for unstimulated controls and is prepared by diluting FM4-64 in water to 1 mM. Solution 2 is for depolarizing synaptosomes and is prepared by diluting FM4-64 in a 400 mM KCl solution. Calcein blue solution was aspirated from warmed microplates and solution 1 was rapidly added to control wells as well as solution 2 to stimulated wells and incubated for 2 minutes (step E in Figure 7). To wash not internalized FM4-64 dye solutions 1 and 2 were replaced by 10 mM Advasep-4 in HBK and again incubated for 2 minutes (step F in Figure 7). After destaining, buffer was exchanged to HBK and slides were ready for imaging. All steps were performed in the dark to prevent photobleaching of the dyes. Immediately after the staining procedure, synaptosomes were imaged as described in 3.7. The excitation wavelength of FM4-64 is 500 nm so the Alexa 546 filter set was used; Calcein Blue excitation wavelength is 360 nm so the DAPI filter set was used for data acquisition.

Glutamate release assay was performed according to Nicholls et al (Nicholls et al., 1987) with modifications. Briefly during this enzymatic assay catalyzed by glutamate dehydrogenase (GDH) emitted fluorescence is measured which occurs while released glutamate is oxidized to oxoglutarate and $NADP^+$ is reduced NADPH as shown in Figure 8.
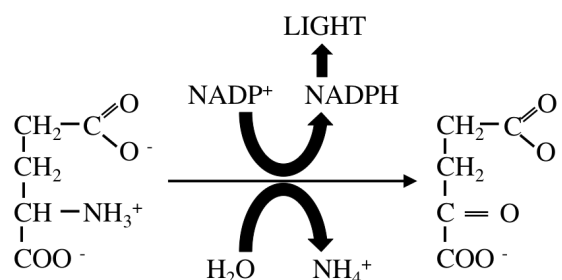
*Figure 8: Enzymatic reaction catalyzed by Glutamate Dehydrogenase during glutamate release assay*

The required synaptosome concentration of 0.7 mg/ml was determined immediately after synaptosome preparation. Aliquots of a 1 ml-volume were incubated in $Ca^{2+}$-free HBM at 37 °C for 60 minutes and transferred to a glass cuvette containing (Hellma Semi-Microcuvette, Müllheim, Germany) a magnetic stirrer. Cuvettes were positioned in a spectrometer (Luminescence Spectrometer LS 50 B, Perkin Elmer, Waltham, USA) and fluorescence was measured for 600 or 700 seconds. The temperature was kept constant at 37 °C and the stirrer speed was set to "low". During measurements, the cuvette was accessed to add chemical compounds according to Figure 9.
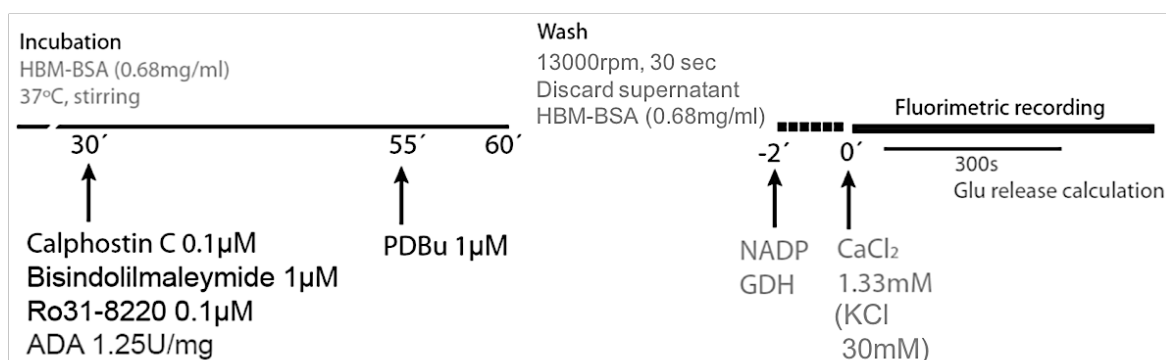


*Figure 9: Timing of incubation and chemical treatments during glutamate release assay (including concentrations).*

Excitation wavelength was 340 nm and emission wavelength 460 nm. To measure spontaneous release of glutamate, $CaCl_2$ was added but KCl was omitted. To measure release from depolarized synaptosomes, KCl was added. 200 seconds before termination of measurement, 2 μM of glutamate was added as a reference. Data was exported as CSV files

into Microsoft Excel and traces were plotted. For KCl applications, fluorescence signal was subtracted before depolarization. For spontaneous release 2 minutes of measurement of signal before starting the assay was used to determine background trace for subtraction. The calibration was done for each trace individually from the signal obtained at 2 µM glutamate.

### 3.1.5 Primary neuronal culture

Primary neuronal culture was prepared according to the Banker method (Kaech and Banker, 2006) modified to cultivate cells on electron microscopy grids. Gold Quantifoil grids (R1/4, Au 200 mesh, Quantifoil Micro Tools) were additionally coated with a 20-25 nm carbon layer (MED 020, BAL-TEC). For sterilization, grids were transferred to 4-well-dishes (Falcon, Amsterdam, Netherlands) and UV-irradiated for 30 minutes inside the clean bench. EM grids were coated with poly-L-lysine in a 1 mg/ml solution in 0.1 M borate buffer (pH 8.5) overnight in the dark as well as glass bottom dishes for light microscopy. Unbound poly-L-lysine was washed multiple times with autoclaved MilliQ water and soaked in neuronal plating medium until cell seeding.

Before primary neuronal culture, an astroglial cell feeder culture was started. Postnatal day 1 pups of Sprague-Dawley rats were sacrificed according to the guidelines of the Max-Planck-Institute of Biochemistry. Hippocampi and cortices were dissected after carefully removing meninges and transferred to ice cold CMF-HBSS-Hepes (Calcium- and Magnesium-free Hank's Balanced Salt Solution with 5% Hepes, Invitrogen, Carlsbad, USA). Tissue was minced and digested in 0.25% Trypsin and 0.1% (wt/vol) DNase I in a 37 °C water bath for 15 minutes and triturated with a 10-ml automated pipette. Cells were passed through a 70 µm Cell strainer (Becton Dickinson and company, Heidelberg), centrifuged at 120 g for 10 minutes to remove enzymes and lysed cells and resuspended in Glial Medium (Minimal Essential Medium with Earl's Salt and L-glutamine, 0.6% D-glucose, 100 U/ml Penicillin-Streptomycin, 10% fetal bovine serum; Invitrogen, Carlsbad, USA). Glial cells were plated in 75-cm$^2$-flasks (Falcon, Amsterdam, Netherlands) at a density of 7.5 x 10$^6$ cells per flask and incubated in a $CO_2$ incubator at 37 °C. Medium was exchanged every third day and flasks were swirled harshly to remove loosely attached cells from the flask surface such as microglia or O2A progenitor cells. Nearly confluent astroglia were harvested by trypsination, centrifuged at 120 g for 7 minutes and resuspended in Glial

Medium for seeding in 6-mm-dishes at a concentration of $1.0 \times 10^5$ cells per dish. Glial medium was exchanged every 3-4 days and replaced by Neurobasal/B27 medium for preconditioning. Preconditioned Neurobasal/B27 is required to feed primary cultured neurons.

Neuronal tissue was dissected from E17-21 Sprague-Dawley rats. The pregnant dam was sacrificed in accordance with the guidelines of the Max-Planck-Institute of Biochemistry. The uterus was dissected from the womb and immersed in CMF-HBSS-Hepes. Embryos were dislocated from the amniotic sacs and sacrificed by decapitation. Using a dissecting microscope, brains were removed from the sculls, cerebellar hemispheres were removed, and meninges was carefully stripped off. Hippocampi were identified in each hemisphere, dissected with micro-scissors and transferred to ice cold CMF-HBSS-Hepes. The tissue was minced into small pieces with razor blades and transferred to 0.25% Trypsin and 0.1% (wt/vol) DNaseI in CMF-HBSS and incubated for digestion for 15 minutes at 37 °C. To wash out enzymes, CMF-HBSS medium was replaced three times and tissue was triturated with Pasteur pipettes, micropipette and 10-ml automated pipette. To remove left over clumps of biological material, the cell solution was passed through a 70 μm cell strainer (Becton Dickinson and company, Heidelberg). After centrifugation (120 g, 10 minutes) cells were resuspended in neuronal plating medium (NPM: Minimal Essential Medium with Earl's Salt and L-glutamine, 0.6% D-glucose, 5% fetal bovine serum; Invitrogen, Carlsbad, USA) and seeded to a concentration of $3.0 \times 10^5$ cells per well on EM grids and glass bottom dishes (MatTek corp., Ashland, USA) for immunohistochemistry. After 4 hours of settling cells on the substrate in a $CO_2$ incubator preconditioned Neurobasal/B-27 medium was added to the dishes. Three days after cell seeding 5 μM AraC in preconditioned Neurobasal/B27 was added to each culture dish. One third of medium was exchanged once a week with Neurobasal/B27 and preconditioned Neurobasal/B27 in equal parts. After 21 days grids were vitrified for CET.

## 3.1.6  Sample vitrification

Samples from primary neuronal culture and synaptosome preparation were plunge-frozen in a liquid ethane/propane mixture with Vitrobot Mark III or Vitrobot Mark IV (FEI, Eindhoven, Netherlands).

Materials and methods

For synaptosomes Quantifoil® R 2/1 copper or molybdenum 200 mesh grids (Quantifoil, Jena, Germany) with 100 Holey Carbon film were glow discharged for 45 seconds to remove organic contamination and to apply a negative charge and thus create a hydrophilic surface (Aebi and Pollard, 1987). After incubation, samples were mixed with 4 times concentrated BSA-coated 10 nm gold nanoparticle solution (Aurion, Wageningen, Netherlands) in a ratio of 1:10. Fiducial marker solution was concentrated by two centrifugations (14000 rpm, 60 minutes, Beckman table top centrifuge, Beckman Coulter, Krefeld, Germany) and the commercial buffer was replaced by HBM to wash off sodiumazide. A volume of 4 µl of sample mixed with nanogold was applied to grids held by Vitrobot tweezers and attached to the plunging arm. Vitrobot was operated with a food pedal and the settings are shown in Table 3.

*Table 3: Vitrobot settings for both generations (Mark III and Mark IV) for synaptosome vitrification*

| Vitrobot | Blot force | Blot offset | Blotting time | Temperature | Humidity |
|---|---|---|---|---|---|
| Mark III | - | -3 | 10 seconds | 37 °C | 95% |
| MarkIV | 10 | - | 10 seconds | 37 °C | 95% |

Primary cultured neurons were seeded onto Quantifoil R 1/4 gold grids (Au 200 mesh) with a 100 Holey Carbon support film. Immediately before plunge freezing, culture dishes containing 4 grids were transferred one by one to an incubator (37 °C, no $CO_2$ available) located next to Vitrobot Mark IV. BSA-coated 10 nm gold nanoparticle solution was again 4 times concentrated by centrifugation (2x, 14000 rpm, 60 minutes). Grids were taken from culture dishes with a pre-warmed Vitrobot tweezers and attached to the plunging arm. During Vitrobot plunging procedure, 4 µl of gold solution was applied through the side entry. Vitrobot Mark IV settings were as described in Table 3. In addition, a waiting time of 5 seconds was imposed to allow fiducial markers to diffuse on the sample.

Immediately after vitrification, all samples were transferred from liquid ethane/propane mixture to liquid nitrogen and into an in-house-designed grid box holding 4 grids for storage. Grid boxes were collected in a perforated 50-ml Falcon tube and stored in a large dewar in liquid nitrogen until data acquisition.

### 3.1.7 Focused ion beam milling of vitrified neurons

To observe mature synaptic structures in primary cultured neurons, vitrified samples were thinned by focused ion beam (FIB) milling as described before (Fukuda et al., 2015). To monitor the milling process, the dual-beam microscope (Quanta 3D FEG or Scios DualBeam, FEI) houses a scanning electron microscope (SEM), which allows low dose imaging of the sample during milling. The additional carbon layer evaporated on the grid before primary culture, helped to find the correct orientation for mounting grids onto a cryo-FIB shuttle (Rigort et al., 2010). Vitrified samples were clipped into a custom-made support frame structure called autogrids (FEI), which was modified with a cut-out to increase accessibility (see Figure 10) of the ion beam for shallow milling angles (Rigort et al., 2012). The cryo-shuttle was transferred from the loading station into the microscope under constant cryogenic temperatures using a cryo-transfer system (PP3000Q, Quorum, East Sussex, UK). The cryo-shuttle with a transfer rod allowed grids to be attached to an in-house-designed 360° rotatable cryo-stage operated at -180 °C. For initial experiments the cryo-shuttle was fixed in an intermediate prep chamber, where grids were sputtered (10 mA, 60 seconds) with a platinum layer to prevent surface charging of specimen. The effect of uneven milling (curtaining) was avoided by applying a protective layer of platinum onto the grid by a gas injection system (GIS). For sample milling, a region of interest was monitored by the electron beam at 5 kV and milled with 30 kV gallium ions at various tilt angles using a variety of beam currents and milling strategies. Since wedges turned out to be more stable, they were milled in a relatively wide pattern of 35 μm, while lamellas are too fragile and were thus milled 15 μm wide. In general, milling was initiated by rough milling of 0.3 – 0.5 nA, to cut rectangular holes into the tissue surrounding the region of interest. The milled area was then thinned down with an ion beam current of 0.1 nA; for lamella milling a thickness of 1 μm was aspired in this step. For polishing the milled surface, currents between 30 pA and 50 pA were used. As an alternative approach, a pre-defined milling strategy called cleaning cross section (CCS) was performed at 0.1 nA. In CCS, a selected area is milled line by line using the following parameters: the thickness of the sample in the region of interest (z-size = 6 μm), a dwell time (700 ns) and an overlap (65%).

Materials and methods

During milling and thinning process, the thickness of the sample was estimated by observing SEM images. Fibbed samples were handled with additional care to prevent lamella breaking and stored in modified grid boxes designed to hold autogrids.
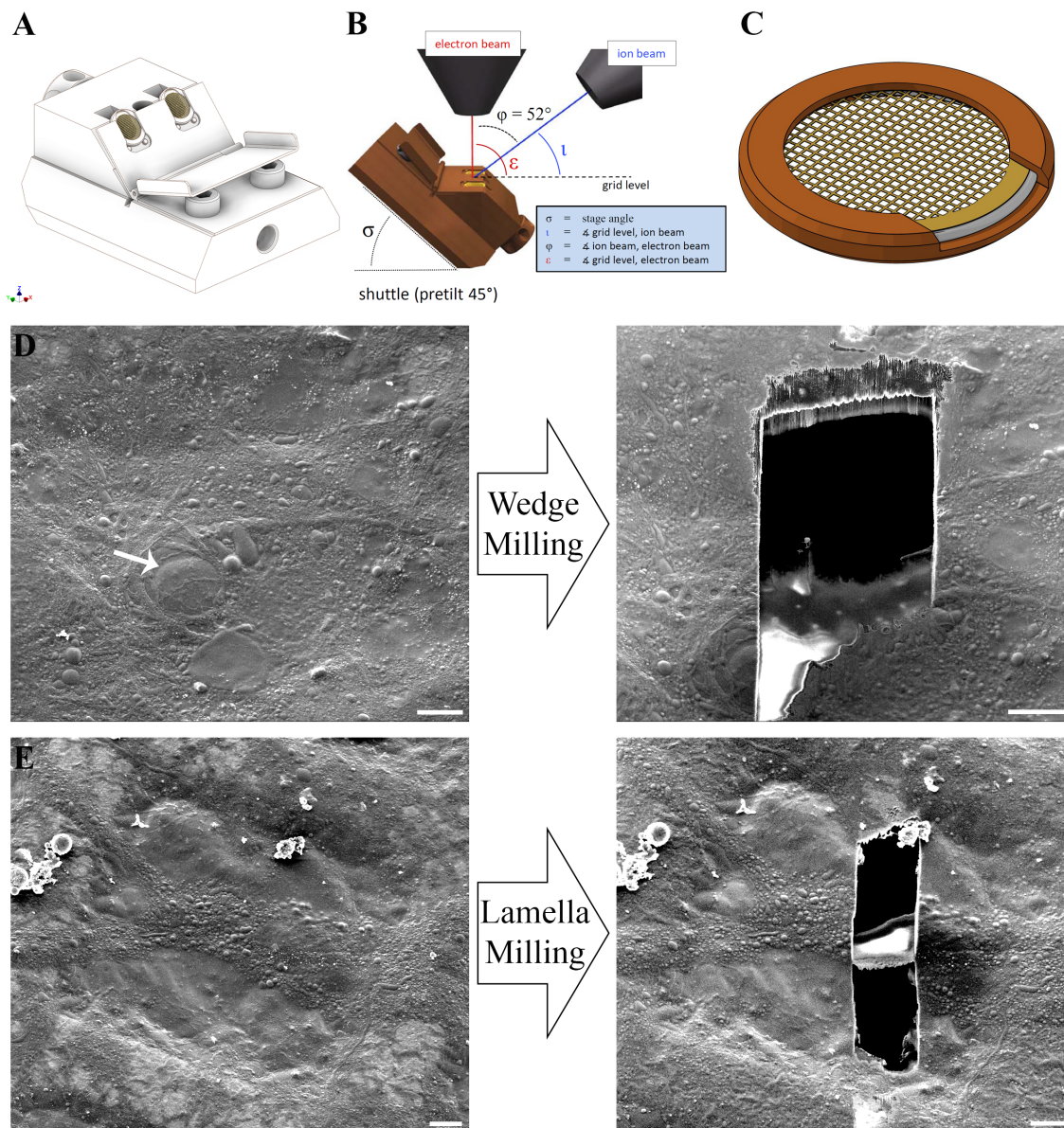


*Figure 10: FIB milling geometry and strategies.*

**A**: *FIB shuttle with two samples loaded in normal fibbing autogrids.* **B**: *Geometry of electron and ion beam is depicted, as well as the tilt angle of the shuttle itself which has to be set by the user. Usual stage tilts for milling were 12° - 18°. The real incident angle of the ion beam on the grid is l=σ-7.* **C**: *A modified autogrid for wedge milling providing a larger cut out than the autogrid used for lamella milling depicted in A.* **D**: *Wedge milling (in SEM) of primary cultured neurons was performed close to a cell body (arrow) whenever possible.* **E**: *SEM image of lamella milling at neuronal processes. Scale bars: 10 μm (Drawings A, B and C provided by Tim Laugks)*

## 3.2    Proteinbiochemistry

Samples of particulate and soluble fractions of synaptosomes were prepared as described in 3.1.3 and analyzed by gel electrophoresis and western blotting. Synaptosomes of the density of 0.7 mg/ml were either treated as control sample or treated with L-AP4 for translocation of Munc13-1 to the presynaptic membrane (see Figure 6) (Ferrero et al., 2013).

### 3.2.1  SDS-PAGE

Samples of Synaptosomal membranes and cytosol were separated by denaturing discontinuous polyacrylamide gel electrophoresis (Laemmli, 1970) (PAGE). The acrylamide concentration was 7.5% for the separation gel and 4% for the stacking gel (BioRad, Mini-PROTEAN, Munich, Germany). Samples were mixed with 5:1 with sample loading buffer (250 mM Tris pH 6.8, 10% SDS, 50% glycerol, 0.02% bromphenol blue, 10% β-mercaptoethanol) and boiled at 95 °C for 5 minutes before being loaded onto the gel. As a reference ladder Precision Plus Protein Standards (BioRad) was loaded. Electrophoretic separation was performed in SDS-PAGE running buffer (25 mM Tris, 1.92 mM glycine, 0.1% SDS) two steps, initially at 90 V for 30 minutes and then at 140 V for 60 minutes. After electrophoresis, gels were either washed in western blot transfer buffer or incubated in InstantBlue protein stain (Expedeon Ltd., Over Cambridgeshire, UK) for 15 minutes with constant shaking which renders destaining unnecessary.

### 3.2.2  Western blotting

After electrophoretic separation, proteins were transferred by Semi-Dry Western Blotting for protein identification by immunostaining.

PVDF (polyvinylidendifluorid) membranes were prepared by soaking in pure ethanol and rinsing in MilliQ water. The membranes and filter paper were immersed in semi-dry blotting buffer (SDB: 48 mM Tris, 37 mM Glycine, 1.3 mM SDS, 20% Methanol) for 15-30 minutes, the PAGE-gel was equilibrated for 5 minutes and protein transfer was performed for 50 minutes at 150 mA and 8-15 V. Immunolabelling of desired proteins was carried out with a Fast Western Blot Kit (Thermo Fisher) which includes reagents for primary incubation and a HRP reagent as well as a washing buffer. Primary antibodies were

monoclonal mouse anti-panMunc13 (1:200, Sigma, Darmstadt, Germany) and monoclonal mouse anti-β-tubulin (1:2000, Sigma). Detection of chemiluminescense was done using a chemiluminescence analyzer (NTAS Chemocam, Göttingen, Germany) with an excitation laser at a wavelength of 473 nm. Quantitative analysis of western blot bands was done using ImageJ (Fiji (Schindelin et al., 2012)).

## 3.3   Cryo electron microscopy data acquisition

During the process of this projects, microscope instrumentation available was revolutionized.

All data was collected with field emission gun-equipped microscopes operated in low dose mode (Koster et al., 1997) and at liquid nitrogen temperature. Initial tomograms of synaptosomes were acquired with two Tecnai F30 G$^2$ Polara (FEI Eindhoven, Netherlands) transmission electron microscopes at 300 kV acceleration voltage. A loading station allows to transfer samples in liquid nitrogen, where they were clipped into gold plated copper cartridges and loaded into a multispecimen holder capable of holding up to six samples. The holder was evacuated by an adsorption pump and cooled by liquid nitrogen. A cooled down insertion rod allows the transfer from the multi-specimen holder to the computerized goniometer cryostage. The latter is able to tilt samples to ± 70°. In earlier experiments Polara microscopes were equipped with an in-column CCD camera (UltraScan 4k, Gatan, Pleasanton, USA), a retractable TV camera and Gatan imaging filter (GIF), operated in zero-loss mode (20 eV slit), as well as a post-GIF 2k CCD (Gatan MegaScan, 2k x 2k) camera. In later stages of the experiments the CCD camera was replaced by a Gatan K2 Summit direct electron detector (DED, 4k x 4k) operated in counting mode, which is capable of dose fractionation. Data was recorded in frames with a zero-tilt exposure time of 1/10 of the total exposure time of one projection image. Consequently, ten subframes were recorded at zero tilt and number of subframes increased in higher tilts proportional to the increasing exposure time.

Primary cultured neurons were imaged by FEI Titan Krios transmission electron microscope equipped with a volta phase plate (Danev et al., 2014) (VPP), an energy filter

and K2 direct detector. Sample loading to Titan Krios was performed by an automatic loading system.

Tomographic tilt series were recorded with FEI tomography software or Serial-EM (Mastronarde, 2005), using a number of magnifications and defocus values depending on instrumentation. Additional to the FEI user interface, Polara and Titan microscopes use Digital Micrograph (Gatan) to control K2 direct electron detector. At Polara TEM, a -5 μm defocus was typically used. At Titan Krios TEM with VPP a defocus value of -500 nm was used. Imaging was performed in the low dose mode. A desired defocus was set prior to tomogram acquisition and confirmed before every projection image by three-image-focusing in a distance of 3-5 μm from the area of interest and along the tilt axis. Additionally, tracking images were recorded in the same spot and compared to earlier tracking images by cross-correlation to correct image and beam shifts (Figure 11). The total electron dose received by a sample during one tilt series, was kept below 100 e$^-$/Å$^2$. Depending on sample thickness, a total dose of 25-50 e$^-$/Å$^2$ reached the CCD or electron detector. To apply the electron dose evenly, exposure time was increased while tilting the sample and thus expanding the path of electrons travelling through the sample by choosing the option to vary intensity as 1/cosine of tilt angle. Depending on accessibility of the area of interest by the electron beam in high tilts (grid bar or ice crystal contamination obscuring the beam) tomograms were recorded with a total tilt range of around -65° to 65° and an increment of 1.5° or 2°. Detailed tomography settings are listed in Supplementary table 2 (see chapter 7).
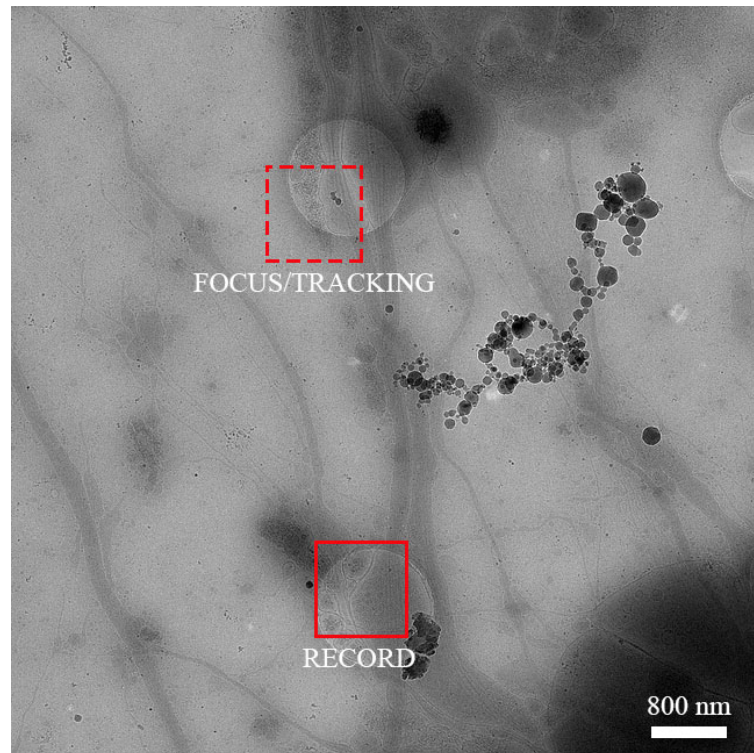
*Figure 11: Low dose acquisition scheme.*

*Low magnification image of record area (red rectangle) and the focus and tracking area (dashed red rectangle) along the tilt axis. Grid shows primary cultured neurons grown on a R1/4 Holey Carbon Film (Qantifoil®)*

## 3.4   Data reconstruction and image processing

Reconstruction and image processing procedures also improved during the course of this project. While the early CCD-data was reconstructed using TOM toolbox (Nickell et al., 2005) direct detector data was processed with Digital Micrograph, K2Align or MotionCor2 (Zheng et al., 2017) and reconstructed with IMOD (Kremer et al., 1996).

TOM toolbox tilt series projections were saved in EM file format (Hegerl, 1996) and aligned using fiducial markers keeping the alignment error below 1.5 pixels. Reconstruction was done with the weighted back projection method in analytical or exact mode. The latter was suitable for visual presentation of data as well as manual segmentation since high frequency information is reduced while low frequency information is enhanced. Tomograms reconstructed using the analytical mode showed a higher signal-to-noise ratio but together with anisotropic denoising (AND) was suitable for further analysis of the data by

segmentation. To increase SNR, tomograms were binned twice before reconstruction and cropped in z-direction to the thickness of the actual biological structure recorded.

Data recorded with K2 Summit direct detector was processed by subframe alignment. Digital Micrograph frame alignment used a combination of Hanning Window and bandpass filter, while the in-house-developed software K2Align used a bandpass filter with the values 0.001-0.063. Since Digital Micrograph produced occasionally misaligned frames for thick samples, Motioncorr2 became the standard software to use without any further settings.
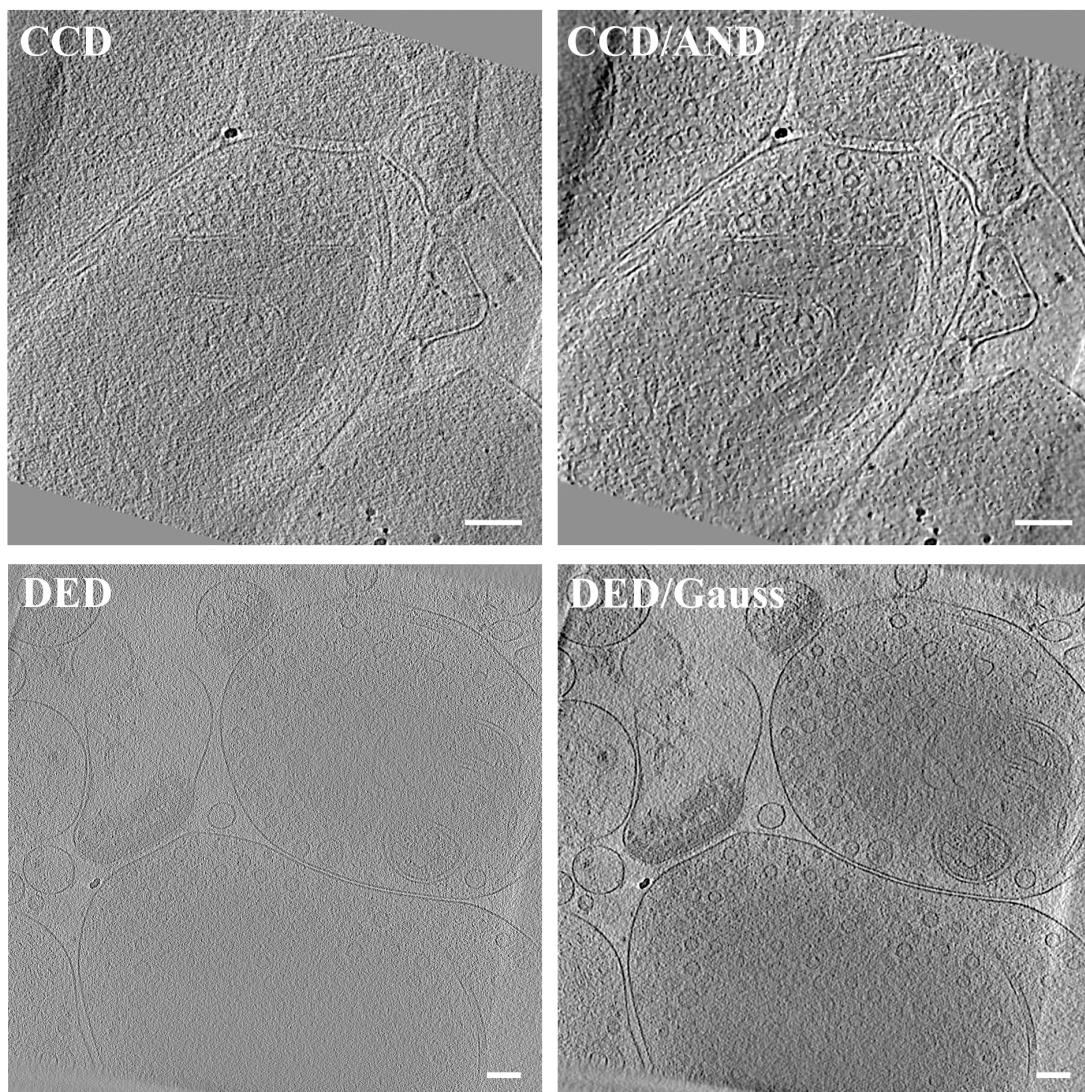


*Figure 12: Slices of tomograms acquired with CCD and DED, both at Polara2, with and without anisotropic denoising or gaussian filter applied. Scale bars: 100 nm*

Materials and methods

K2 data was reconstructed with IMOD. In short, X-rays were removed in the initial step, cross-correlation was done using default settings and course alignment was created from a 4-times-binned stack while at no point data was converted to bytes. During binning the antialiasing filter was applied. Fiducial markers were seeded manually in the zero-tilt projection image and tracked automatically for the remaining projections. For the fine alignment of the stack, correction of rotations, tilt angles (grouped with group size 5) and beam tilt was applied. Fine alignment as well as bead tracking were fixed manually. This was usually necessary for thick samples such as for synapses. Tomogram positioning was skipped or only done for the purpose of presenting the data in the flattest volume possible. The final aligned stack was created with binning twice or four times depending on the project's purpose and without linear interpolation. Tomograms were generated with weighted back projection method with a radial filter cutoff at 0.45. Logarithm density scaling factor was set to intensity values between -15,000 and 15,000, which were extracted from the tilt.log file created by IMOD. During post-processing the tomogram was cropped in z-direction and rotated around x-axis.

For tomograms acquired with direct electron detector, anisotropic denoising was not necessary, but a Gaussian filter with 0.2 pixel cutoff was applied (Eman2 image processing suite (Tang et al., 2007), see Figure 12). For data recorded on CCD and reconstructed with the analytical method of TOM an algorithm for noise reduction was used which is capable of automated parameter tuning (Fernandez et al., 2007). To assess the average noise background of the tomogram, a subvolume devoid of any structure is defined. Since interesting structures show significantly higher gradient than the defined background, all voxels having gradient below a given threshold are considered background and smoothed by a Gaussian filter. Furthermore, a hybrid diffusion approach is used to combine edge enhancement and coherence enhancement making it possible to efficiently denoise data by highlighting edges and connecting lines. The parameters for these two diffusion modes are tuned automatically based on the information of the subvolume noise and develop in each iteration depending on the remaining noise. There is also the option to stop iterations automatically depending on noise variance between the initial subvolume and a given iteration. Since a mild denoising was the goal, this option was not used but instead iteration numbers of 5-10 were usually sufficient.

## 3.5   Removing contamination-induced reconstruction artifacts

During preparation of samples from primary cultured neurons by cryo-fibbing, a strong redeposition of milled particles occurred repeatedly on wedges but also lamellas. Since different milling conditions (see 4.3.1) did not significantly improve the incidence of the problem, a cleaning procedure was applied. This procedure includes the software-based removal of contamination from the reconstructed tomogram and the 3D reconstruction artifacts arising from the contamination (Fernandez et al., 2016). The initial step is reconstruction of the tomogram from the aligned tilt-series. In Amira, the contamination is masked in y-slices of the tomogram. During the procedure, the mask is reprojected and subtracted from the original tilt-series. The new partially cleaned tilt-series obtained is again reconstructed with weighted back projection. These steps are performed iteratively to gradually remove contamination as well as the resulting artifacts visible in 3d, while valuable information is preserved. Five iterations were usually sufficient, while more iterations did not provide further improvements.

## 3.6   Computational analysis and segmentation

After data processing and reconstruction suitable tomograms were selected for analysis. Aside from tilt series which were too thick to achieve a good signal-to-noise ratio (SNR) multiple morphological features limited the data for analysis. To be selected, synaptosomes had to be in a healthy physiological state defined as follows. For proper supply of ATP, a mitochondrion should be present and healthy looking, synaptic vesicles should be round instead of elongated (a sign of physiological osmotic pressure), signs of degradation should be minimal, such as endosomes and large vacuoles; and finally, presynaptic and postsynaptic structures should be uninterrupted and enclosed by a healthy membrane as well as connected by synaptic cleft proteins.
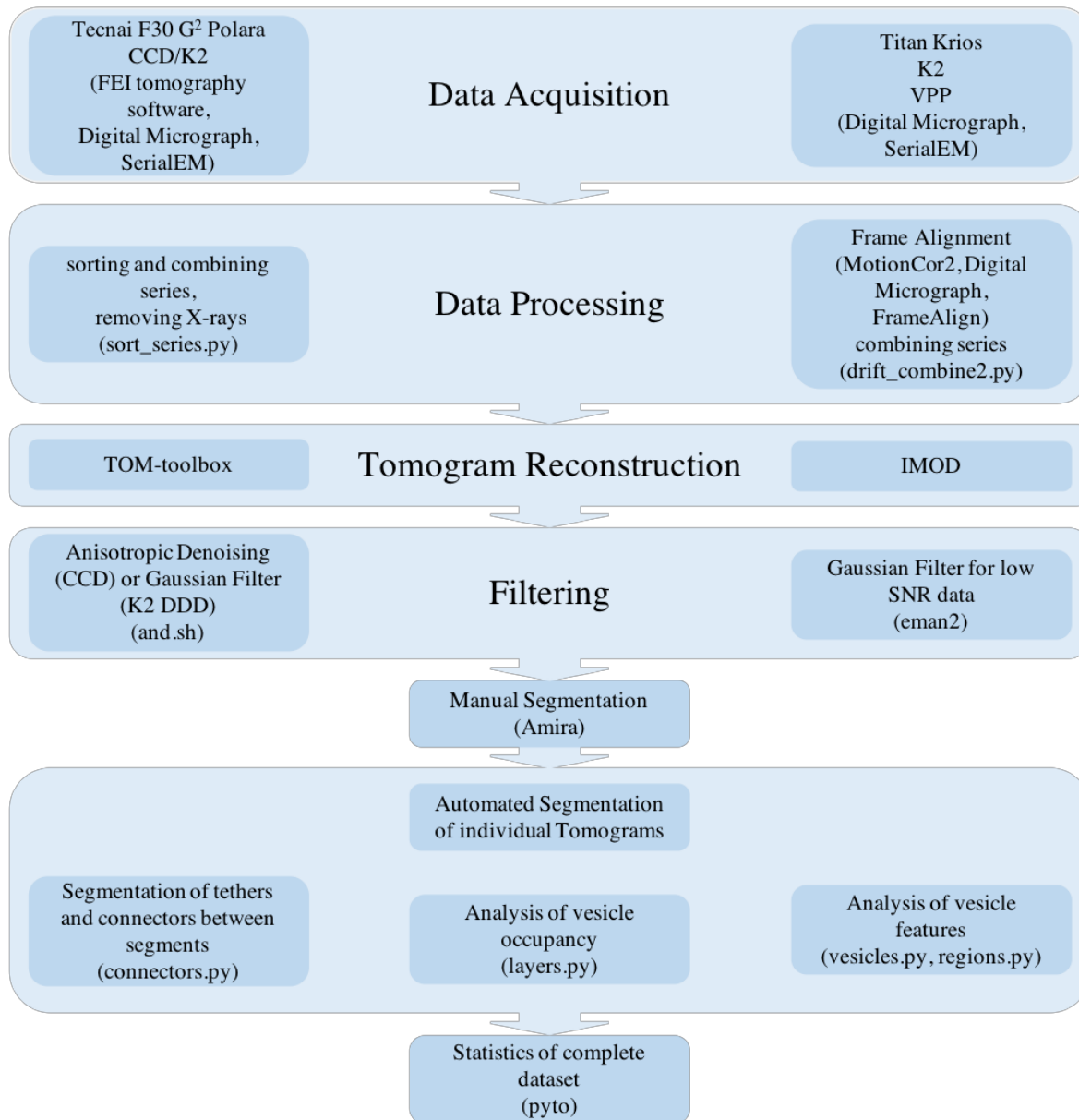
*Figure 13: Overview of the complete workflow from data acquisition to the final statistics of the dataset.*

Tomograms which met all the criteria were included in a semi-automated segmentation workflow (Fernández-Busnadiego et al., 2010). Manual segmentation was done with Amira (FEI), automated segmentation with the help of a pyto software package developed by Dr. Vladan Lučić (Lučić et al., 2016):
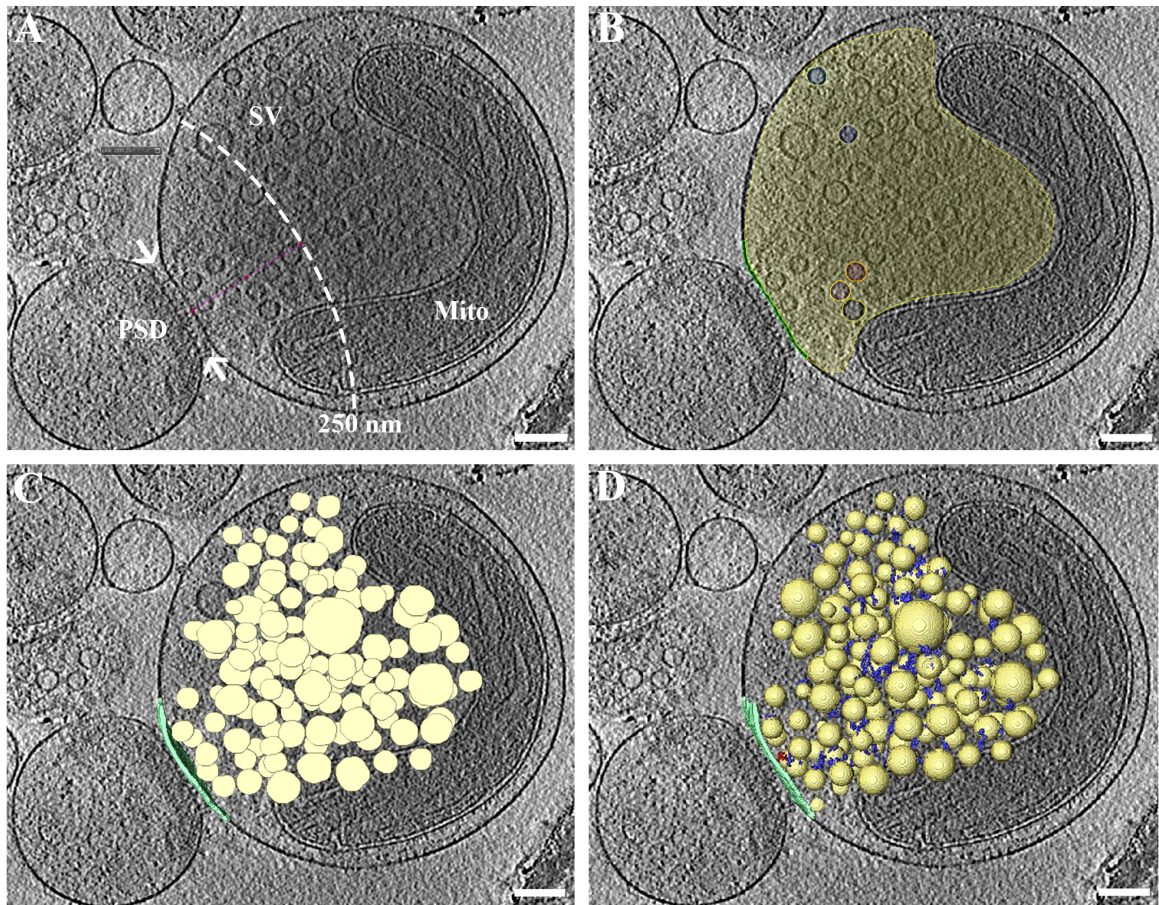
*Figure 14: Segmentation workflow.*

*The reconstructed tomogram (**A**) shows a healthy synaptosome with round synaptic vesicles (SV), mitochondrion (Mito) and a postsynaptic density (PSD) opposite the synaptic cleft (SC) which will be analyzed within a distance of 250 nm from the AZ membrane (membrane at the SC). Amira segmentation (**B**) of the AZ membrane is shown in green, cytosol segmentation is segmented in yellow and equatorial planes of exemplary vesicles on various colors. Isosurfaces of the amira manual segmentation output (**C**) shows the AZ membrane in light green and discs at vesicular equatorial plane. Discs are expanded to balls (**D**) and voxels below the mean background threshold are automatically segmented between vesicles (blue) and between vesicles and the AZ membrane (red) by connectors.py-script. Scale bar: 100 nm*

Initial step was the manual segmentation of equatorial planes of each synaptic vesicle (see Figure 14 A-C) within a distance of 250 nm from the active zone (AZ) membrane as well as the membrane at the AZ (defined by the synaptic cleft). A segmentation region had to be defined as the cytosol around synaptic vesicles ideally omitting structures like microtubules and vacuoles. As part of the Pyto software package used, the segmented equatorial planes of each vesicle were expanded to spheres. Next step was the hierarchical gray-scale based segmentation of voxels connecting membranes and SVs (see Figure 14 D). Connectors are structures that interlink SVs, while tethers are linking SVs to the AZ. The segments were found at multiple threshold levels. The higher limit of the threshold range depends on the average pixel values of the segmentation region. The latter was determined

by the regions.py-script. Setting the upper threshold limit to 10% below the mean value of the background was usually suitable. The lower threshold was set to the lowest threshold value at which segments were detected. The number of thresholds was similar in all analyzed tomograms.

The analysis of connector and tether morphology as well as SV size and distribution was performed and finally statistical results of all data was combined and plotted with matplotlib (Hunter and Hunter, 2011). The confidence tests used during the analysis were Student's t-test for Gaussian distributed values, Kruskal-Wallis test for values not following a normal distribution and Chi-square test for values in discrete bins. Pearson's coefficient and t-test were used for correlation analysis. In all graphs, confidence values are indicated as: *: $p < 0.05$; **: $p < 0.01$; ***: $p < 0.001$.

A workflow overview of the analysis procedure with all scripts included in the pyto software package is summed up in Figure 13.

## 3.7   Immunohistochemistry and light microscopy

As mentioned during primary neuronal culture cells were not only seeded on EM grids but also on glass bottom dishes (GBD) for light microscopy applications. Here the presence of synapses in cultured neurons was shown by Immunohistochemistry. Munc13-1 was stained against Phalloidin and PSD-95, a protein present in the postsynaptic density.

In short, immunolabelling was done by fixing neurons inside the GBD with 4% Paraformaldehyde in 0.1 M PBS (Phosphate-buffered Saline, Gibco, Carlsbad, USA) followed by three washing steps for 15 minutes in PBS at room temperature. Primary antibodies were diluted in Buffer G (0.1% Triton X-100, 5% normal goat serum in PBS), specifically monoclonal mouse anti-panMunc13 (1:200, Sigma) and anti-PSD-95 (1:2000) and incubated over night at 4 °C, followed again by three washes in PBS. GBD were then incubated in Buffer G containing TRITC (Tetramethylrhodamine B isothiocyanate)-conjugated Phalloidin (1:1000) and Alexa 488-conjugated anti-mouse secondary antibody

(1:1000) for 1 hour at room temperature. Neuronal cells were again washed in PBS three times and mounted in Fluoromount for imaging.

Fluorescence data acquisition was accomplished using an Axiovert 200M (Zeiss, Oberkochen, Germany) epifluorescence microscope, equipped with a motorized stage (DC 120100, Märzhäuser, Wetzlar, Germany). Data was recorded on a CCD camera (AxioCam MRm, Zeiss) and fluorescence was stimulated with a short-wavelength mercury lamp.

# 4. Results

This chapter is divided into three parts. First, light microscopy, physiology and biochemistry experiments are presented that prove viability of synaptosome samples and to illustrate proper effects of pharmacological treatment of synaptosomes. The second part focusses on the main part of this thesis, that is on the statistical of synaptosomal tomograms. The third part shows statistical results from the analysis of primary cultured neuron synapses in situ.

## 4.1   Viability assays of synaptosomes

According to Whittaker (Whittaker, 1993) Synaptosomal cell fractions are viable and capable of transmitter release for many hours. Nevertheless, it is worthwhile to confirm the viability of synaptosomes for the handling of the individual researcher. Here this confirmation was performed by combining endocytosis of synaptic vesicles after stimulation of transmitter release with KCl with that of control samples without stimulation.

Moreover, effects of the pharmacological treatments on synaptic release were measured by glutamate release assay.

### 4.1.1  Light microscopy of synaptosomes

To perform light microscopy on synaptosomes the cell fractions have to be attached to an objective slide. To achieve this a very low concentrated (20 µg/ml) synaptosome solution was centrifuged inside an 8-well ibidi objective slide. As can be seen in the bright field images of Figure 15 synaptosomes form an even layer on the coated slide.
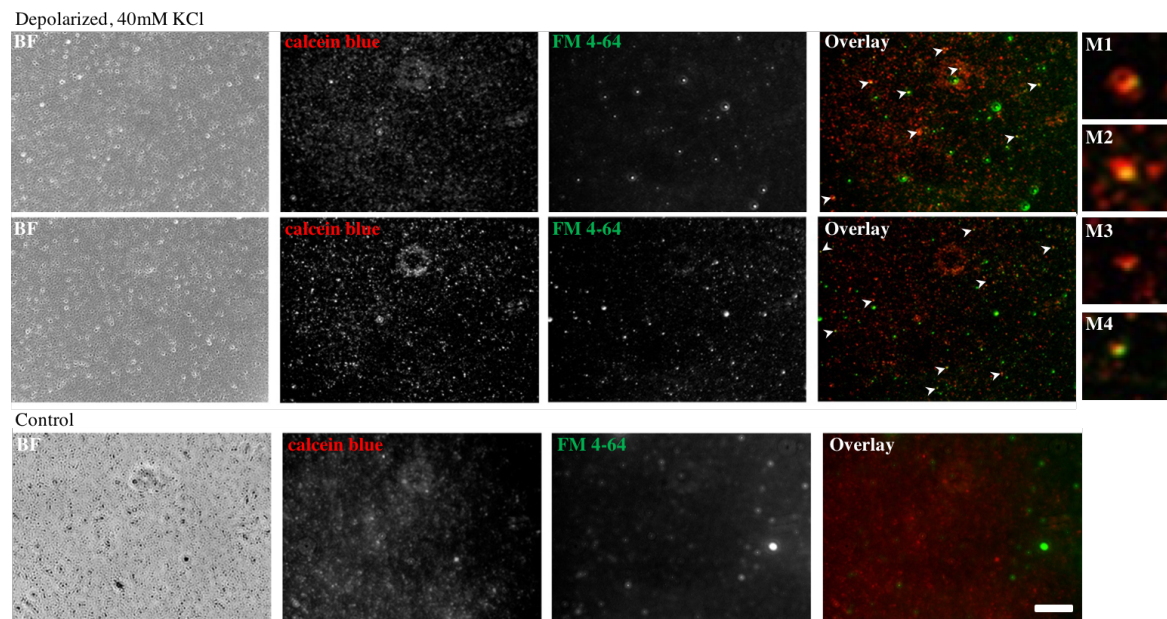
*Figure 15: Analysis of endocytotic activity of synaptosomes.*

*Calcein blue was internalized by synaptosomes independently of stimulation. FM 4-64 dye was taken up during endocytosis after stimulation or after spontaneous release for controls. Arrowheads indicate the most prominent overlay signals of both dyes, which were absent in control samples. Magnified images M1 - M4 show examples for overlay of both signals.*

Thus, this assay is suitable to determine physiological activity of a very low yield experiment like collecting synaptosomes from primary cultured neurons or organotypic slice cultures. The second column of Figure 15 shows the calcein blue signal residing in the cytosol. For detection of the fluorescent signal of calcein blue, the acetoxymethyl (AM-) group has to be cleaved off while entering the intact membrane of a viable cell (Daniel et al., 2012). Thus, the signal shows viable synaptosomes with maintained membrane integrity. The third column shows endocytosed synaptic vesicles stained by FM4-64 dye. Colocalization events are small puncta indicated with arrowheads in column "Overlay" and magnified puncta are illustrated in insets M1 – M4. Clear overlay of both signals was exclusively visible in synaptosomes depolarized and thus stimulated for release with 40 mM KCl, while control samples did not show any overlay puncta.

Results

## 4.1.2  Glutamate release of synaptosomes

Due to the relatively high volume of synaptosome solution required for each release measurement and the aspired protein mass of at least 0.67 mg/ml (Sanchez-Prieto et al., 1987) only 10 – 12 assays were performed for each dissection. Furthermore, synaptosomes tend to aggregate stronger the more tissue is disrupted during preparation. This leads to disturbance of signal detection by the spectrometer due to swirling dense synaptosome clumps. Consequently, most of the spectrometer traces reflect these disturbances as can be seen in Figure 16, curve PDBu + Ro31. The erratic courses of the majority of traces were difficult to analyze and were therefore not included in average release values. While plenty of assay schemes were tested, such as using ionomycin replacing KCl for depolarization (showing steep release curves, data not shown), or different $CaCl_2$ concentrations, the scheme shown in 3.1.4 proved to be the most efficient to achieve results.
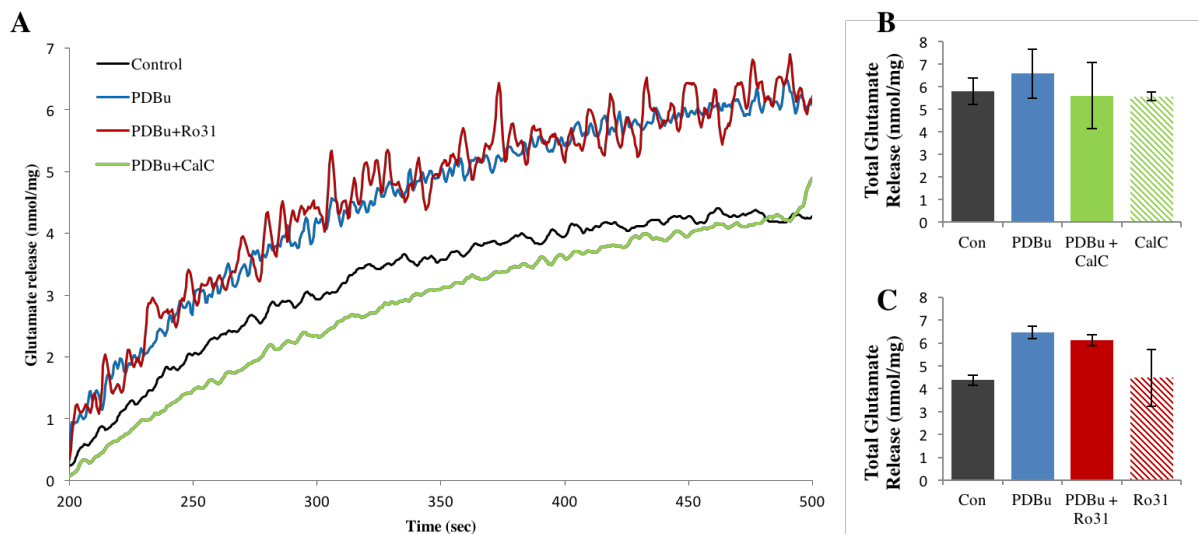


*Figure 16: Glutamate release assay with 40 mM KCl stimulation.*

*A: Exemplary traces of fluorometric measurement of glutamate release from depolarized synaptosomes, as well as the average total release (B and C) of glutamate per mg of tissue in the sample from three measurements of each treatment with PDBu, PDBu with CalC, PDBu with Ro31 and CalC/Ro31 individually. Mean values (n=3): **B**: Con: 5.81 ± 0.60 nmol/mg, PDBu: 6.58 ± 1.09 nmol/mg, PDBu + CalC: 5.61 ± 1.47 nmol/mg, CalC: 5.56 ± 0.19 nmol/mg. C: Con: 4.37 ± 0.21 nmol/mg, PDBu: 6.54 ± 0.27 nmol/mg, PDBu + Ro31: 6.11 ± 0.23 nmol/mg, Ro31: 4.48 ± 1.24 nmol/mg*

As can be seen in Figure 16 glutamate release is strong from synaptosomes depolarized with 40 mM KCl (5 nmol/mg stimulated Glu release vs. 0.8 nmol/mg

spontaneous Glu release), thus only a weaker release facilitation mediated by PDBu can be shown (mean facilitation from plots Figure 16 B and C: 24.9%). Despite the weaker effect of PDBu on depolarized synaptosomes, a consistent inhibition of release facilitation was observed for CalC-treated synaptosomes. Equally consistent was the release facilitation observed in Ro31-treated synaptosomes, while both the exclusive treatment with CalC and Ro31 omitting PDBu did not influence released glutamate amounts.

Because strongly stimulated synapses are depleted of releasable vesicles, analysis of synaptosomes was performed on KCl-free samples. Spontaneous release patterns are shown in Figure 17. During this experiment the timing of incubation in $CaCl_2$ revealed the short-term effect of PDBu-induced facilitation. In these experiments synaptosomes were washed from compounds added to the buffer during incubation 2 minutes prior to measurements. The tissue was combined with GDH, NADP as well as $CaCl_2$ either simultaneously or $CaCl_2$ was added immediately before onset of measurement. In the latter case release facilitation could be observed throughout measurement (Figure 17 C), while the time gap of 2 minutes between $CaCl_2$ incubation and spectrometer measurement resulted in diminishing release facilitation after a total time of four minutes (Figure 17 A). The slope of the PDBu trace runs parallel to the control trace after 2 minutes of measurement, but a steady slope of PDBu traces is depicted in Figure 17 C with initial $CaCl_2$ incubation from onset of measurement.
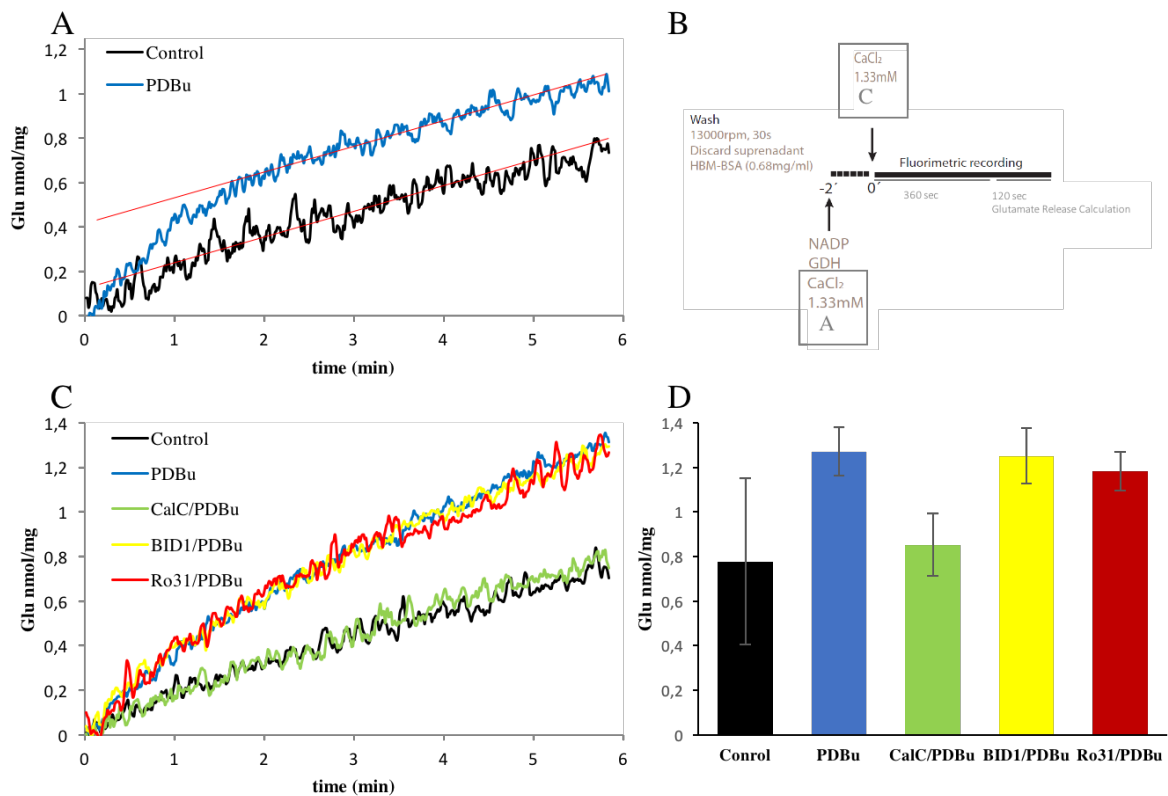
Results



*Figure 17: Spontaneous glutamate release from synaptosomes in native state or after treatments with PDBu or PDBu with either CalC, Ro31 or BID1.*

*Spontaneous release facilitation is a short-term effect indicated by plot **A**, showing a diminishing slope for release of PDBu-treated synaptosomes after 2 minutes. This effect was only observed when $CaCl_2$ was added before the pre-incubation step of 2 minutes (**A**), but a continuous increased release was observed (**C**) when CaCl2 was added with the onset of fluorometric recording as seen in scheme **B**. The latter was the strategy for the measurement in plot **C** showing a continuous increase of release for PDBu-treated as well as for BID1- and Ro31-treated synaptosomes, while CalC-treated synaptosomes release glutamate in the dimension of control samples. Mean values for **D**: Con: $0.78 \pm 0.37$ nmol/mg (n=5), PDBu: $1.27 \pm 0.12$ nmol/mg (n=6), CalC/PDBu: $0.85 \pm 0.14$ nmol/mg (n=6), BID1/PDBu: $1.25 \pm 0.12$ nmol/mg (n=6), Ro31: $1.18 \pm 0.09$ nmol/mg (n=7).*

Because synaptic transmitter is not depleted of synaptosomes by depolarization in this case, spontaneous release could be strongly facilitated by PDBu (62.8% increase of released glutamate in nmol/mg). Weak release facilitation was observed in CalC/PDBu-treated samples (8.9%) and BID1/PDBu- as well as Ro31/PDBu-treatments resulted in release facilitation comparable to PDBu treatment alone (64.1% and 51.3%, respectively) (Figure 17 D).

These findings confirmed that PDBu causes facilitation of synaptic release and synaptic, as it was shown before (Martín et al., 2011). These results indicate the suitability of the experimental setup to visualize plasticity in Cryo-EM with the assistance of the

chemical compounds used in this assay. Furthermore, the analysis of unstimulated synaptosomes promises to reveal a stronger facilitation effect.

### 4.1.3 Translocation of Munc13 shown by proteinbiochemistry

Since L-AP4-mediated release facilitation is provoked by binding of Munc13 to DAG, a translocation of Munc13 from cytosolic reservoirs to the plasma membrane can be observed. This was shown before (Martín et al., 2010) and confirmed here for samples prepared for CET. Soluble (cytosol) and particulate (plasma membrane) fractions of synaptosomes were derived by hypo-osmotic lysis and centrifugation, Munc13-contents were determined by western blot and quantified by densitometry (Figure 18). Samples were normalized against the levels of β-tubulin as a loading control.
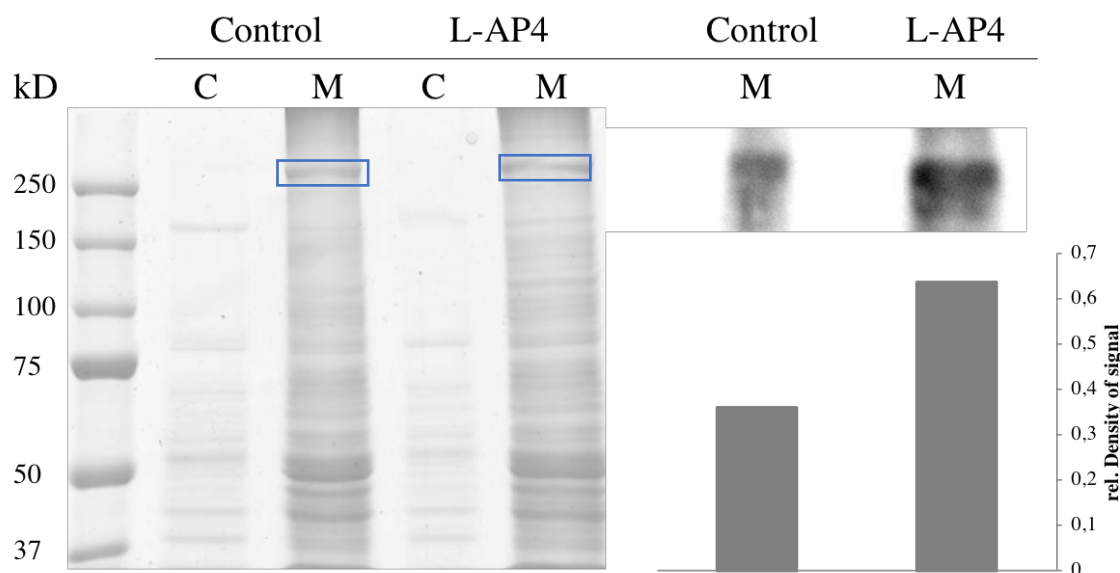


*Figure 18: SDS-PAGE and western blot against Munc13 in synaptosomal fractions.*

*Cytosolic (C) and membraneous (M) fractions were separated in SDS-PAGE (Munc13 in blue rectangle) and Munc13-content was quantified against a loading control of β-tubulin by desitometry.*

As can be seen in Figure 18 the cytosolic fraction does not show a signal for Munc13 (antibody used binds all four Munc13 isoforms) in the western blot while the membrane fractions show strong signals. Hence only the Munc13-content of the membrane fractions can be compared here. L-AP4-treated synaptosomes show a 1.77-times increase in Munc13-content of plasma membrane fractions in reference to controls.

In the introduction of this thesis a summary of methods to manipulate the pathway which ends up in translocation of Munc13 to the presynaptic membrane was given. This effect was tested by proteinbiochemistry. After initial experiments with the L-AP4 compound (glutamate release assay and proteinbiochemistry in the following chapter), additional research of the interactions in the presynapse, led to the change to the compound PDBu. First of all, the receptor mGluR7 does not exist in every synapse and thus not every synaptosome recorded with CET will show the structural features of release facilitation. Also, mGluR7 as a receptor of L-AP4 mainly acts on N-type $Ca^{2+}$-channels, while mature synapses hold a higher ratio of P/Q-type $Ca^{2+}$-channels and thus will show a lower effect of L-AP4-binding to mGluR7 (Ladera et al., 2009; Martín et al., 2011). Furthermore, L-AP4 can inhibit glutamate release depending on incubation times (Martín et al., 2010). PDBu on the other hand directly acts on Munc13 and is more independent of the existence of specific $Ca^{2+}$-channels, since PDBu-dependent release facilitation is independent of ionic membrane currents (Silinsky and Searl, 2003). Also the PKC-inhibitor BID1 was not included in the structural analysis, since it has the same ATP-competitive inhibitory effect as Ro31 (Wilkinson et al., 1993).

## 4.2   Structural analysis of the presynaptic terminal

The architecture of presynaptic terminals was studied from rat cerebrocortical synaptosomal fraction in the native state as well as under pharmacological treatment.

Since synaptosomal fractions are synapses detached from neuronal processes and held together by cell adhesion molecules of the synaptic cleft, they retain structural integrity as well as physiological function. Synaptosomes are viable for up to 4 h and are capable of several cycles of neurotransmitter release and vesicle recycling upon depolarization with a high amenability to pharmacological manipulation (Whittaker, 1993).

Synaptosome preparation for this study was performed according to the standard Percoll gradient protocol, in order to yield synaptosomes of high viability rate and containing mitochondria (Dunkley et al., 2008). The protocol was further adapted to criteria needed to perform CET (Fernández-Busnadiego et al., 2010) and improved to increase viability and

decrease aggerates (Martín et al., 2010). The synaptosome preparation protocol has several steps of centrifugation and resuspension, which can disrupt membranes if performed too harshly. If not performed carefully, these steps can cause formation of electron dense aggregates of synaptosomes (> 1 μm), which aggravates data acquisition.



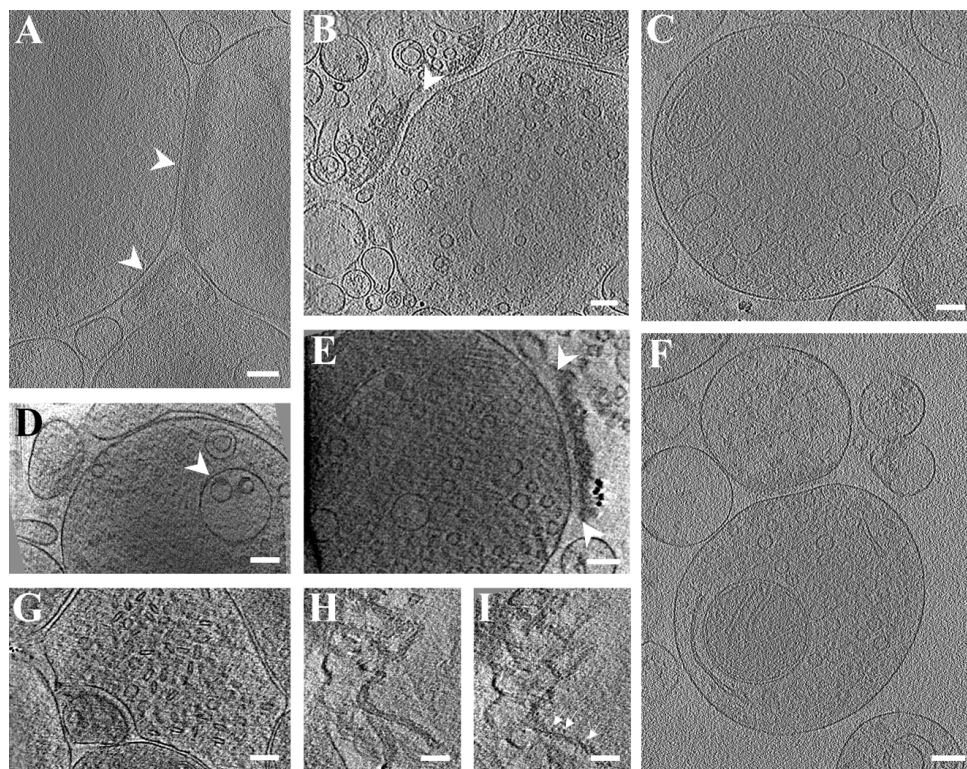*Figure 19: Exemplary slices of tomograms excluded for analysis.*

*Presynaptic terminals with more than one AZ (**A**, arrowheads) as well as disrupted synaptic clefts (**B**, arrowhead), or postsynapse (**E**, arrowhead) render analysis impossible due to unclear definition of the membrane at the AZ as well as a distict SV pool. Signs of degradation such as multivesicular bodies (**D**, arrowhead), large number of vacuoles (**C**) and degrading mitochondrion (**F**) excluded data. Aspherical SVs (**G**) were often observed together with deteriorated mitochodrion: **G**, **H** and **I** are from the same tomogram and show cristae (**H**) of disrupted mitochondrion with ATPases (**I**, arrows) sitting on them. Scale bars: 100 nm*

Fragmented, or synaptosomes showing signs of impaired physiological integrity were excluded from the analysis. Figure 19 sums up the prevailing features of synaptosome samples that are either symptomatic of degradation or disturb reliable analysis of the data. Degradation is in progress in synaptosomes with disrupted (G), swollen (Daum et al., 2013) (F) or missing mitochondria, leaving the cell fragment without ATP supply to maintain physiological function. Missing mitochondria often correlated with elongation of SVs (G), possibly a sign of osmotic stress due to malfunctioning ATP-dependent proton pumps sitting on SVs for acidification of vesicular lumen. Progressing symptoms of degradation were

Results

multi vesicular bodies (D), different shapes of endosomes and large (~ 100 µm in diameter) SVs (C) as a symptom of decreased endosome trafficking (Wagner et al., 2015).

Additional to morphological cues for degradation, specific features prevented accurate analysis of the data. For manual tracing of membranes opposed to each other along the synaptic cleft, both membranes must be intact and connected by cleft proteins to be properly assigned as pre- and postsynaptic membranes. Torn postsynaptic compartments as well as interrupted clefts (B) were excluded. Since the analysis of the presynaptic lumen was performed in an interval of 250 nm, double synapses (A) were excluded from the analysis as well, as the lumen to be analyzed usually overlapped.
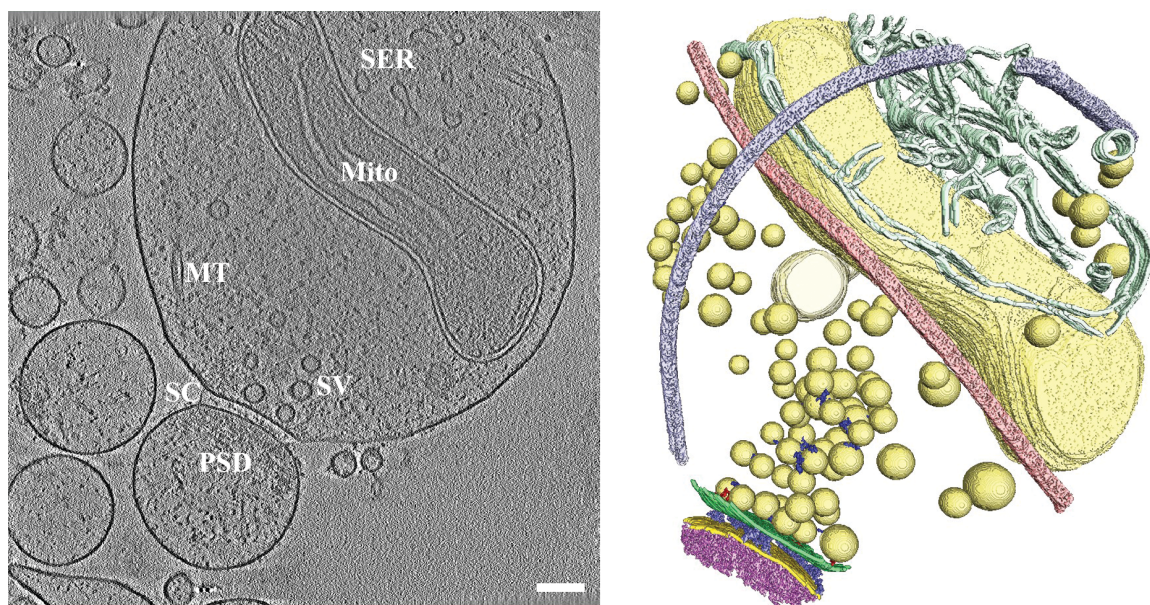


*Figure 20: Tomography of isolated synaptic terminals using VPP.*

*The tomographic slice of a synaptosome with intact presynaptic and postsynaptic compartment including postsynaptic density (PSD), connected by structures visible in the synaptic cleft (SC). The presynapse is endowed with mitochondrion (Mito), microtubules (MT) as well as smooth ER (SER). The rendered isosurface of the segmented tomogram displays compartments in the presynapse due to the volume of the Mito (light yellow), while MT span across the presynaptic volume (light pink and light purple, interrupted MT due to missing wedge). SER (light green) is concentrated distant from the AZ, while SVs accumulate in several pools close to the AZ. The membrane at the AZ (green) is connected by densities in the cleft (purple) to the postsynaptic membrane (yellow), which is equally endowed with structures of the PSD network (pink). Scale bar: 100 nm, Slice thickness: 1.368 nm*

A good tomogram of a synaptic terminal is illustrated in Figure 20. Data acquisition with Titan Krios microscope equipped with K2 DDD and Volta Phase Plate allows obtaining high contrast data, despite the sample thickness of 440 nm. Interconnecting filaments between SVs are clearly visible as well as synaptic cleft densities and the PSD. Two microtubules span the presynaptic compartment, well visible in the segmented volume. They

are endowed with internal densities, which are resolved especially well in neuronal samples. The large mitochondrion separates the presynapse into SV-filled and SER-filled compartments. Also, SVs are clustered in pools by a network of protein filaments connecting SVs to each (connectors) other and tethering SVs to the AZ membrane (tethers).

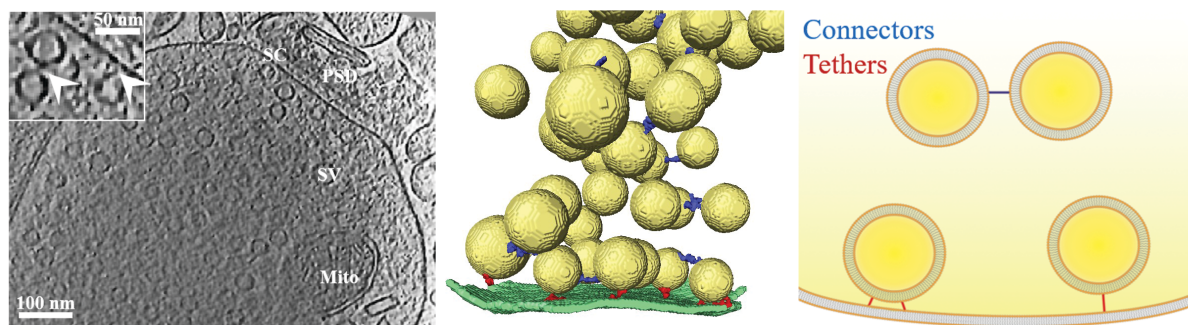The analysis of phorbol ester treated synaptosomes presented here focuses on these connectors and tethers and provides a statistical evaluation of their features.



*Figure 21: Analysis of tethers and connectors in synaptosomes.*

*Protein filaments connecting SVs (connectors) to each other and SVs to the AZ membrane (tethers) are shown here in a tomographic slice (indicated with arrowheads in the inset). The isosurface of a segmented volume shows tethers in red and connectors in blue (AZ membrane in green). The scheme uses the same color code in red and blue for tethers and connectors and will be used throughout this thesis for illustration of statistical data.*

## 4.2.1  Structure of phorbol ester treated presynaptic terminals

As described previously, tomograms of physiologically intact isolated synaptic connections were analyzed. Features to look for were closed pre- and postsynaptic membranes with presynaptic mitochondrion and intact cleft, as well as spherical SVs and an intact PSD. Additionally, data to be segmented needs a signal-to-noise-ratio that was sufficiently high for manual tracing of presynaptic and vesicular membranes and the software-based detection of fine filaments and protrusions.
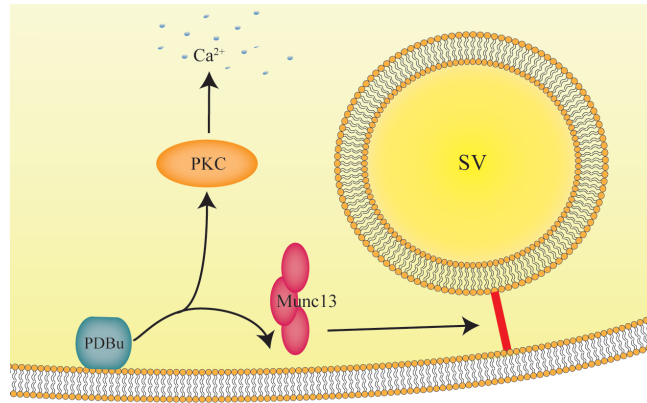
*Figure 22: Pathway of release facilitation initiated by the presence of PDBu.*

Data quality improved throughout the progress of this project since charge-coupled device (CCD) based electron detectors were replaced by direct detection devices (DDD). The latter are able to detect electrons directly without the use of scintillators diminishing the image quality. Direct detectors allow for smaller pixelsizes and provide a better transfer of high spatial frequencies. Finally, in the last phase of data collection VPP became a standard tool for the acquisition of tomography data. As the number of tomograms is critical for significant statistical results of the analysis, it was my goal to combine acquired data after assessing if the difference in quality influences final results. To make the three different datasets combinable CCD, DDD and VPP data was processed by anisotropic denoising and gauss filtering as mentioned in 3.4 and illustrated in Figure 12. As can be seen in Figure 23, tomograms showed a similar contrast and SNR and pixelsizes of twice binned data were in an acceptable range between 1.368 nm and 2.644 nm. Additionally, statistical analysis of synaptic features was examined for individual tomograms to ensure the results do not refer to the detection method used. Figure 23 evidently displays an analysis of SV radii and a quantification of tethers with data ordered by date of acquisition and thus data acquisition method. No apparent influence of data acquisition method on determination of structure sizes (SV radii) or quantification of structures (N of tethers) is discernable. Thus, datasets were combined for the following statistical analysis.
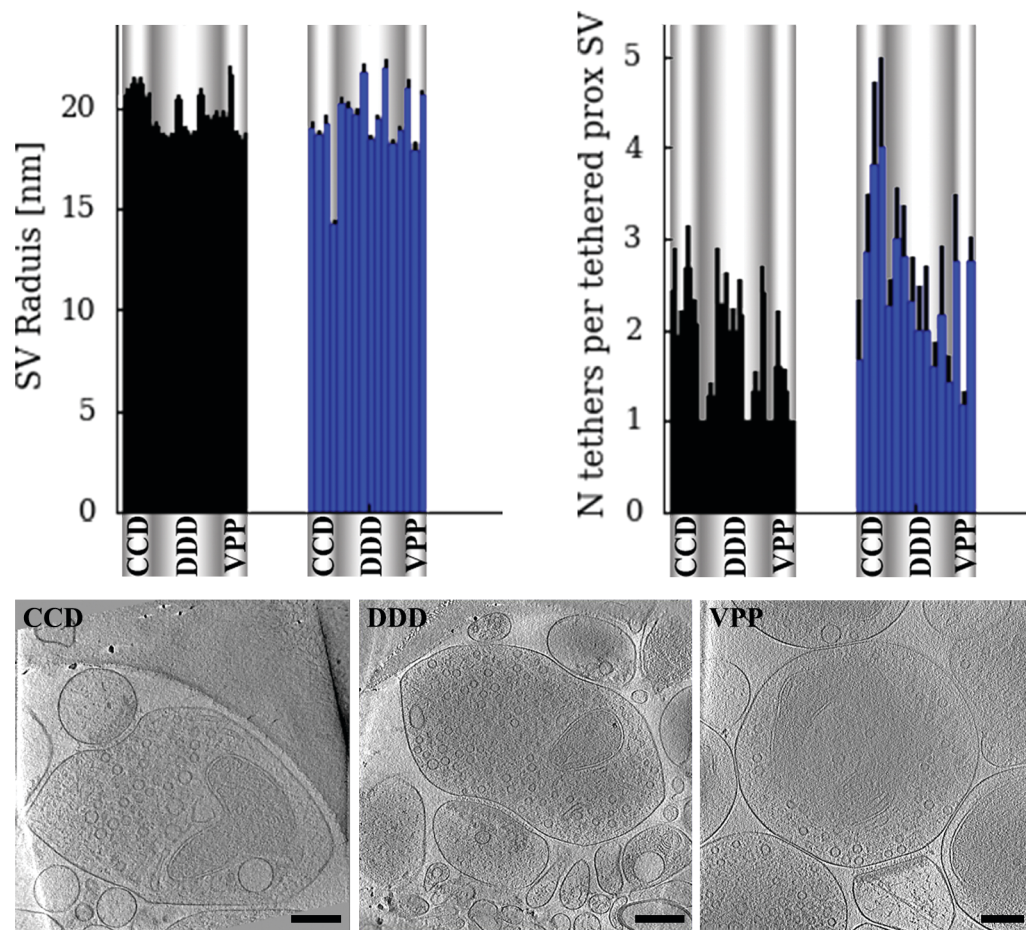
*Figure 23: Comparison of data acquired with CCD, DDD or DDD with VPP.*

*Statistical analysis of synaptic features presumably not affected by PDBu-treatment (SV radius and number of tethers) are depicted for each tomogram; each column represents a tomogram of the dataset with control tomograms in black and treated tomograms in blue. For both datasets 4 tomograms were recorded on a CCD camera with a FEI Polara microscope, 9 tomograms were recorded on K2 DDD at a Polara microscope and 4(controls) / 3 (PDBu) tomograms were recorded on a K2 DDD using VPP. Statistical results depicted here show no pattern of bias depending on the detector used. Exemplary tomograms of average quality in the bottom row of images, acquired with CCD, DDD and VPP respectively, show a similar contrast after anisotropic denoising (CCD data) and Gaussian filter (DDD data). Scale bars: 200 nm*

Results

*Table 4: Summary of the total number of tomograms acquired, the number of dissections (total number/analyzed number) from which samples were prepared as well as the number of synaptosomes with its vesicles, tethers and connectors analyzed in included in statistical analysis.*

|  | Control | PDBu |
|---|---|---|
| Synaptosomes recorded/analyzed | 27/17 | 59/16 |
| Synaptosomal preparations total/analyzed | 13/5 | 14/5 |
| vesicles | 2115 | 1450 |
| tethers | 319 | 333 |
| connectors | 4550 | 4084 |

As mentioned before, synaptosomes preserve the physiological structure of a synapse (Fernández-Busnadiego et al., 2010) but they come in different sizes of the presynaptic volume and the cleft size. To account for the variance in presynaptic terminal size, vesicles were segmented within a zone of 250 nm from the AZ. Synaptosomes investigated in this thesis showed the typical distribution of SVs within this zone. A peak in vesicle occupancy in the proximal zone (0 – 45 nm), a significantly lower density of SVs in the intermediate zone (45 nm – 75 nm), and the highest density of SVs in the distal zone (75 nm – 250 nm). As opposed to this, stimulated synapses were depleted of SVs in the proximal zone and shows a decreased SV occupancy in that area (Fernández-Busnadiego et al., 2010). To visualize fine details in SV tethering, depolarization of synapses was avoided here. In tomogram recorded for this project, PDBu-treated synaptosomes showed significantly smaller AZ-membrane area. Consequently, wherever necessary results were put in relation to AZ surface area in $\mu m^2$ (see Figure 24).
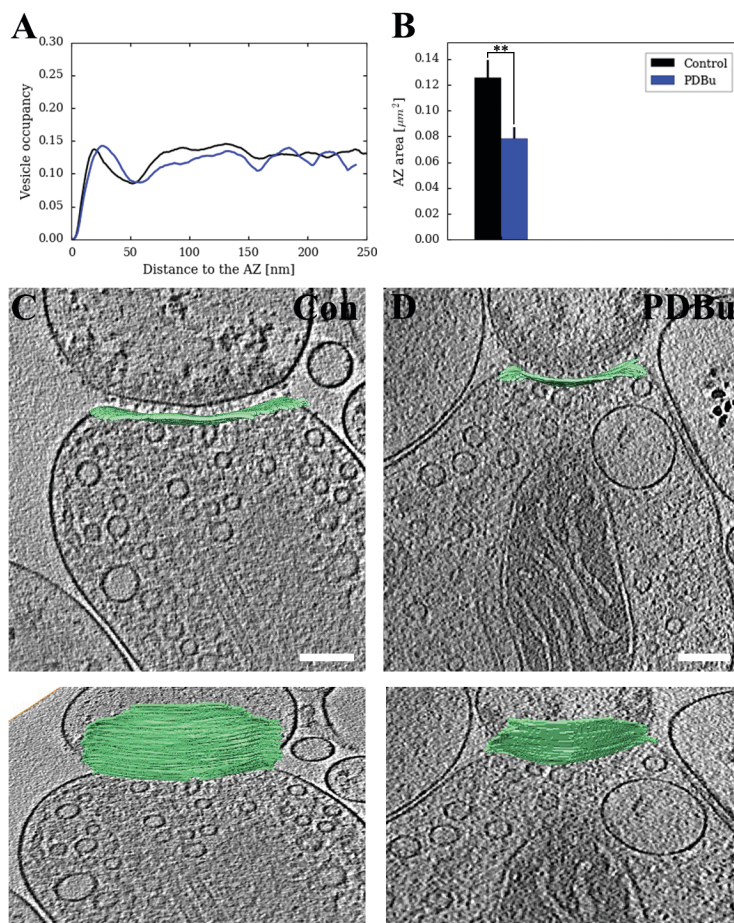
*Figure 24: Vesicle occupancy and mean active zone size.*

*A: Vesicle densities show the typical pattern of healthy synapses with a peak in the proximal zone (0 – 45 nm), a dip in the intermediate zone and a similar density to the proximal zone in the distal zone. **B**: Active zone areas of PDBu-treated synaptosomes are significantly smaller than control synaptosomes (control: mean ± sem = 0.13 ± 0.01 $\mu m^2$, PDBu: mean ± sem = 0.08 ± 0.01 $\mu m^2$, Student's t-test p < 0.01). **C** and **D** show exemplary tomograms with typical appearance for the respective treatment.*

With PDBu recruiting Munc13 to the presynaptic membrane (see Figure 22), we expected to see protrusions prominently accumulating at the AZ membrane. Figure 25 shows three exemplary segmentations of these protrusions for control and PDBu-treated synaptosomes. These were detected automatically by the hierarchical connectivity segmentation implemented in the Pyto software package, where protrusions were defined as segments bound only to the AZ-membrane. No obvious difference in the density of protrusions (without linking SVs) was observed. This indicates that Munc13 being recruited to the presynaptic membrane is immediately involved in vesicle priming and thus orphaned Munc13 may exist or only for a limited time.

Results
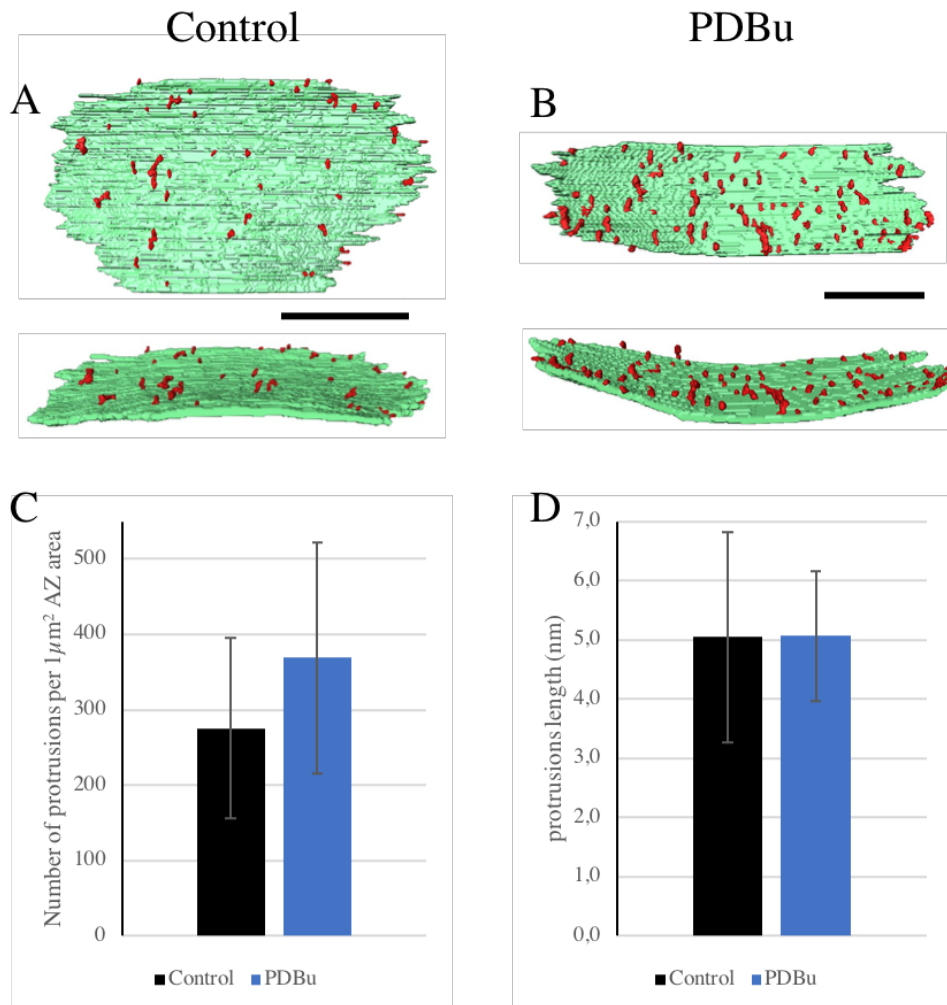


*Figure 25: Segmentation and quantification of protrusions at the AZ membrane.*

*Two exemplary AZ-isosurfaces of control (**A**) and PDBu-treated (**B**) synaptosomes with segmented protrusions; structures binding the AZ membrane exclusively without binding SVs (1-bound segments). PDBu-treated samples show an insignificantly (K-W test, p > 0.1) increased number of protrusions in plot **C**. The length of protrusions is measured perpendicular to the membrane in plot **D**. While structures with a length of around 20 nm are visible in the segmentation, plot **D** illustrates that these structures do not rise from the AZ more than 7 nm. Tomograms were acquired with Polara and Titan Krios microscope, DDD and VPP at a pixelsize of 1.708 nm (control) and 1.684 nm (PDBu). Scale bars: 100 nm*

As indicated by the results of physiological experiments such as glutamate release assay we expected to see an SV occupancy increase in the vicinity of the AZ-membrane in PDBu-treated synaptosomes. While the density of SVs in the proximal zone did only slightly increase after PDBu-treatment [1] (plots from data not shown), the number of tethers linking

---

[1] Number of proximal SV per AZ area (1 $\mu m^2$): mean ± sem (control) = 115.17 ± 8.5, N = 17; mean ± sem (PDBu) = 134.41 ± 8.60, N = 16, p > 0.1, Student's t-test.

SVs to the presynaptic membrane increased significantly (see Figure 26). On the other hand, the number of tethered proximal SVs per 1 $\mu m^2$ active zone surface increased only insignificantly [2]. These results led us to the conclusion that the number of tethers per SV is a crucial factor in SV priming for release.
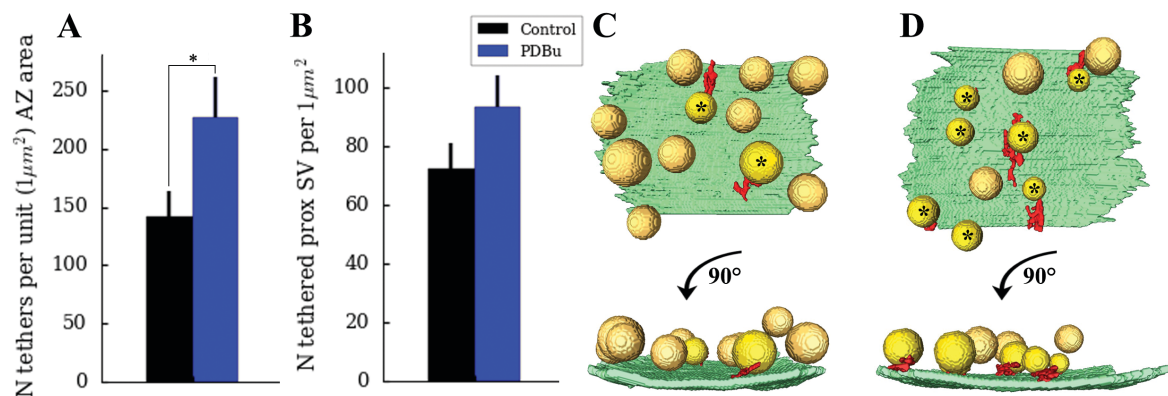


*Figure 26: Tether analysis in phorbol ester treated synaptosomes.*

*Plots **A** and **B** show an increase of tethers/1 $\mu m^2$ AZ membrane as well as an increase of tethered proximal SVs in PDBu-treated synaptosomes. A mean of 141.32 ± 22.84 tethers was counted in control synaptosomes, 226.96 ± 34.14 tethers were counted in treated synaptosomes (N (con) = 17, N (PDBu) = 16, t-test p < 0.05). For tethered proximal SVs in control samples 72.11 ± 9.04 were counted, in treated samples 93.32 ± 10.96 were counted (t-test p = 0.1). **C** and **D** show segmented AZ membranes and proximal SVs (within 45 nm from the AZ membrane), which are tethered (asterisk) and non-tethered. **C** shows tethered SVs in a control synaptosome and **D** shows tethered SVs in a PDBu-treated synaptosome, in top-view and side view respectively.*

In accordance with the results mentioned in the last paragraph, Figure 27 illustrates the significant[3] increase in number of tethers per tethered proximal SVs with PDBu-treated synaptosomes having SVs being tethered more than twice on average. To overcome the energy barrier for membrane fusion and transmitter release, several tethers between the presynaptic membrane and the SV are necessary (Zhou et al., 2017). SVs with more than two tethers are structurally defined to be in the readily releasable pool (RRP; Fernández-Busnadiego et al., 2010). Treated synaptosomes showed a significant[4] increase of the

---

[2] P > 0.1, Student's t-test

[3] N tethers per tethered prox SV: mean ± sem Control = 1.97, N = 146; mean ± sem PDBu = 2.35, N = 114; K-W test p < 0.05

[4] Fraction of SV in RRP: control: fraction = 0.184, N = 228, PDBu: fraction = 0.268, N = 164, Chi-square-test p < 0.05

Results

percentage of proximal SVs that belong to the RRP. This is a strong indicator that higher release competence in PDBu-treated samples could be visualized here.
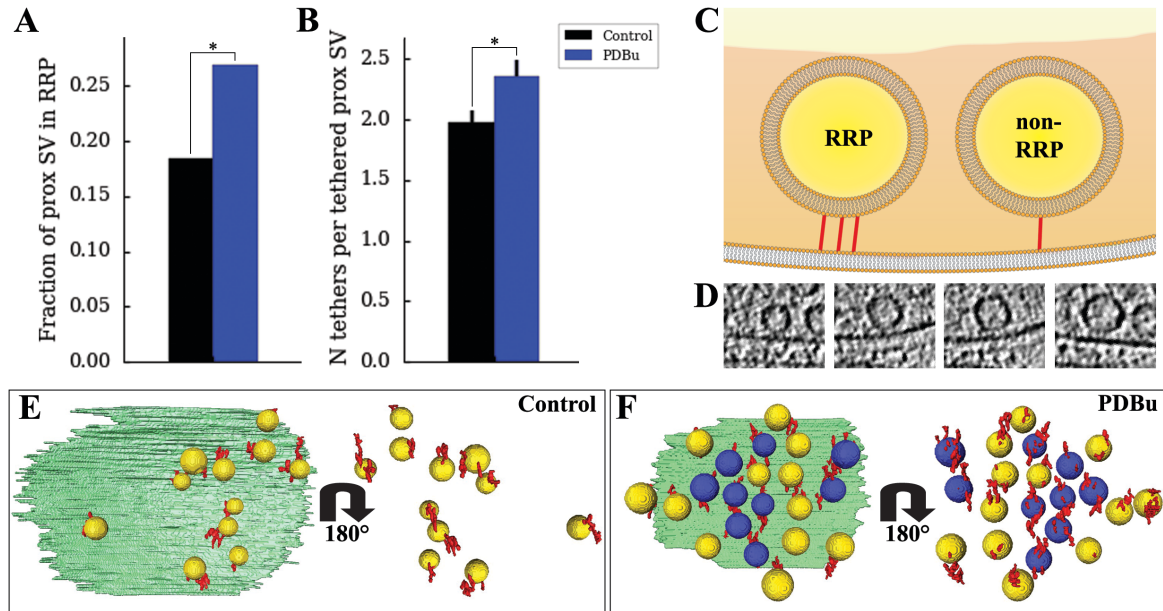


Figure 27: Readily releasable pool in phorbol ester treated synaptosomes.

Plots **A** and **B** show significantly higher fraction of proximal SVs in the RRP (control: fraction = 0.184, N = 228, PDBu: fraction = 0.268, N = 164, Chi-square-test p < 0.05) and a significantly higher number of tethers per tethered proximal SV for PDBu-treated synaptosomes (mean ± sem Control = 1.97 ± 0.09, N = 146; mean ± sem PDBu = 2.35 ± 0.13, N = 114; K-W test p < 0.05). **C** illustrates the definition of SVs in the RRP (> 2 tethers per SV) within the proximal zone of 45 nm from the AZ membrane. Panel **D** depicts exemplary tethered SVs with 3 – 5 tethers per SV in tomography slices of 1.684 nm thickness. **E** and **F** show segmented AZ membranes from a control (**E**) and a PDBu-treated synaptosome (**F**) with tethered SVs. SVs in RRP are blue, SVs tethered by two or less tethers are yellow. In the 180°-flipped perspective tethers are visible. PDBu-treated synaptosomes show short tethers in addition to long tethers.

Additional to the tethering status of vesicles other features meet the eye. Tethered SVs were slightly but significantly[5] smaller in PDBu-treated synaptosomes, a feature which is also visible but insignificant in non-tethered SVs.

---

[5] Tethered SV radii: mean ± sem (control) = 19.51 ± 0.24 nm, N = 146; mean ± sem (PDBu) = 18.46 ± 0.33 nm, N = 114, p < 0.05, Student's t-test.

Non-tethered SV radii: radii: mean ± sem (control) = 18.84 ± 0.32 nm, N = 82; mean ± sem (PDBu) = 18.25 ± 0.42 nm, N = 50, p > 0.1, Student's t-test.

Because the minimal distance of proximal SVs to the AZ is significantly smaller in PDBu-treated synaptosomes[6], it is interesting to investigate how this reduction can be explained by observing the features of tethers more closely. Figure 28 illustrates an overall highly significant reduction in tether length in treated synaptosomes. While PDBu-treated synaptosomes show only one peak of tethers of 6 nm length in the histogram, control samples show an additional peak at 16 nm. This led us to define short and long tethers according to this histogram with a threshold at 11 nm. Interestingly, PDBu-treated synaptosomes showed a lack of additional long tethers, although Munc13 recruitment to the AZ would be expected to create additional tethers in the range of 18 nm – 20 nm. Since these long structures are not increased compared to controls is another indication that SV priming for release occurs rapidly after Munc13 translocation. PDBu-treatment almost doubled the number of short (< 11 nm) tethers creating additional tethering structures. As it can be seen in section F of Figure 28, tiny segments appear on vesicles shortly tethered to the AZ membrane, in addition to long tethers. Visualized in a complete segmentation of the AZ-membrane and the tethered SVs these additional tiny tethers bring SVs in close proximity to the membrane.

---

[6] Minimal distance proximal SV to AZ: mean ± sem (control) = 10.11 ± 0.37 nm, N = 228; mean ± sem (PDBu) = 8.89 ± 0.45 nm, N = 164, p < 0.05, Student's t-test.
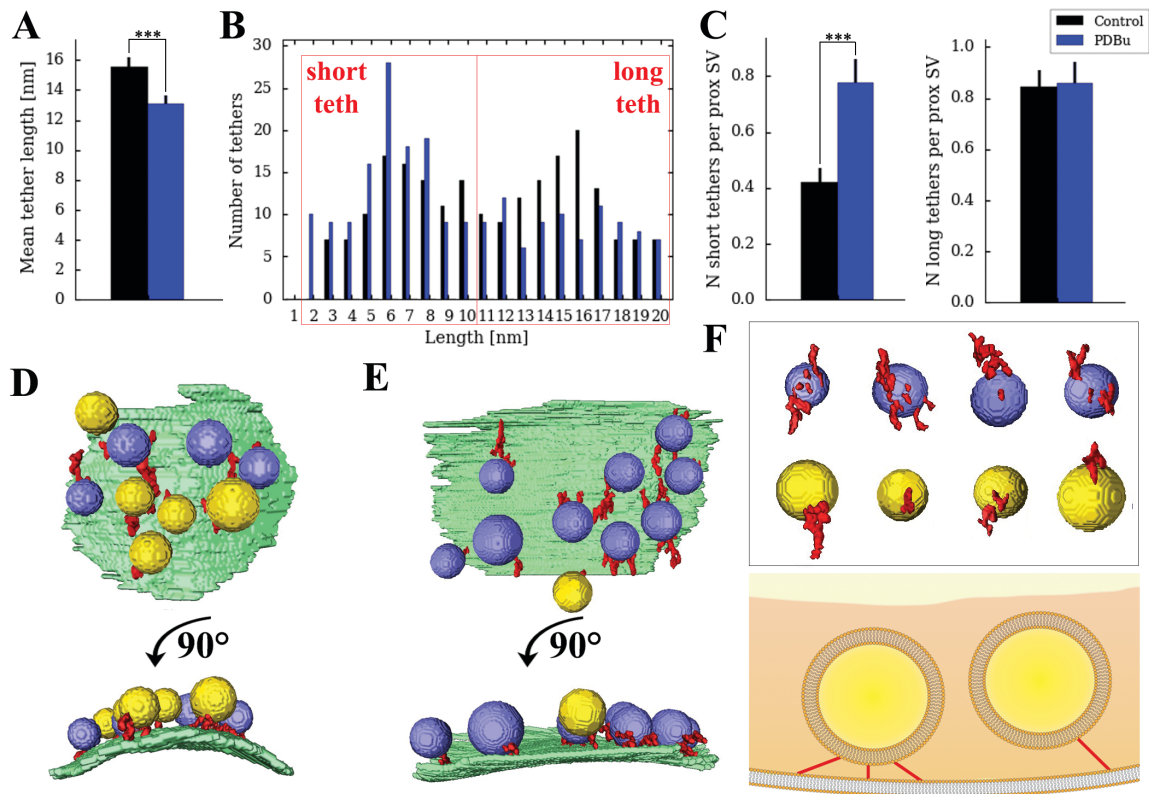
Results



Figure 28: Tether length in phorbol ester treated synaptosomes.

*Plot **A** shows overall significantly shorter tethers in PDBu-treated synaptosomes (mean ± sem control = 15.58 ± 0.57 nm, N = 288; mean ± sem PDBu = 13.1 ± 0.57 nm; N = 270; K-W test p < 0.001). The tether length histogram in **B** shows peaks at 6 nm for PDBu and 16 nm for controls, serving as a basis for defining the threshold of tether length at 11 nm and dividing tethers into categories of short and long. Plots **C** illustrate the higher incidence of short tethers in treated synaptosomes compared to controls (mean ± sem control = 0.42 ± 0.05, N = 228; mean ± sem PDBu = 0.77 ± 0.08, N = 164; K-W test p < 0.001) while long tethers are equally prevalent (mean ± sem control = 0.51 ± 0.05, N = 228; mean ± sem PDBu = 0.54 ± 0.07, N = 164). A schematic illustration in **G** depicts short and long tethers, which were quantified here, in a typical composition. **D** and **E** show segmented AZ membranes with tethered vesicles from a control (**D**) and a treated (**E**) tomogram. The additional short tethers in PDBu-treated synaptosomes results in shortly tethered SVs in purple as opposed to long tethered SVs in yellow (**F**).*

Despite we were mainly expecting an influence of phorbol ester treatment of synaptosomes on SV tethering and priming for transmitter release, multiple other features of the synapse have been analyzed. Amongst these is the connectivity of SVs with each other and features of the connecting network. The overall fraction of connected SVs is the same in the segmented volume[7]. Also, tethered and non-tethered are connected to neighboring SVs in the same ratio[8]. A different pattern in connectivity could be observed in number of

---

[7] Fraction of connected SV: control: 0.808, N = 2115; PDBu: 0.789, N = 1450

[8] Fraction of tethered SV that are connected: control: 0.705, N = 146; PDBu: 0.719, N = 114

Fraction of non-tethered SV that are connected: control: 0.634, N = 82; PDBu: 0.580, N = 50

connectors for each SV, which is decreased[9] in PDBu-treated samples and especially in the proximal zone of the presynaptic volume. In the proximal and intermediate zones, a mean higher length of connectors[10] met the eye. This did not depend on tethering but was purely related to the distance from the AZ membrane (Figure 33 C). This might indicate that PDBu has an influence on the connecting species which can be found proximal to its recruitment area around the AZ resulting in a relatively higher distance between connected SVs as well as a lower number of connectors for each SV.

Altogether, phorbol ester treatment on synaptosomes allowed us to analyze synapses in release facilitated state by cryo-TEM. We saw structures linking SVs to the AZ membrane, which itself is crucial for release of transmitter. The specific fashion of short tethering around 6 nm and multiple tethers per SV turned out to be critical for release facilitation.

### 4.2.2 Inhibitors of phorbol ester treatment

Because the effect of PDBu-treatment on release facilitation in synaptosomes was shown by tomography data, the results should be reconfirmed by two antagonists of the release facilitation pathway; CalC and Ro31. Since phorbol esters mimic the role of DAG, not only Munc13 is recruited to the presynaptic membrane, but also PKC is activated; a kinase which has multiple substrates in the synapse. PKC activation is known to increase transmitter release by upregulation of $Ca^{2+}$-channel activity (Parfitt and Madison, 1993), to augment $Ca^{2+}$-sensitivity of the release machinery (Wu and Wu, 2001) and to increase the size of the RRP (Stevens and Sullivan, 1998). To obliterate these effects from our experiment we used Calphostin C (CalC), as an inhibitor of PKC. CalC is interacting with PKC at the

---

[9] N connectors per SV: mean ± sem (control) = 2.80 ± 0.05, mean ± sem (PDBu) = 2.60 ± 0.06, K-W-test p < 0.05

[10] Connector length in the proximal zone: mean ± sem (control) = 15.15 ± 0.66 nm, N = 198; mean ± sem (PDBu) = 17.53 ± 0.87 nm, N = 135, K-W-test p < 0.05

Connector length in the intermediate zone: mean ± sem (control) = 16.22 ± 0.82 nm, N = 162; mean ± sem (PDBu) = 18.97 ± 1.10 nm, N = 110, K-W-test p < 0.05

very same $C_1$-binding domain as phorbol esters and DAG do. Consequently, CalC equally interacts with the $C_1$-binding domain of Munc13 and thus inhibits the activation of Munc13 as well. To visualize the pure effect of PDBu on Munc13, an additional inhibitor was necessary. The goal is the deactivation of PKC without inhibiting the re-localization of Munc13 to the presynaptic membrane. For this purpose, Ro31 was added to the list of treatments, an inhibitor of the $C_3$-ATP-binding site of PKC with no binding affinity to Munc13 (see Figure 29). In the following chapter samples treated with a combination of PDBu and CalC or PDBu and Ro31 are denoted as CalC- and Ro31-treated samples.

*Table 5: Summary of the total number of tomograms acquired, the number of dissections (total number/analyzed number) from which samples were prepared as well as the number of synaptosomes with its vesicles, tethers and connectors analyzed in included in statistical analysis.*

|  | CalC | Ro31 |
|---|---|---|
| Synaptosomes recorded/analyzed | 26/9 | 33/8 |
| Synaptosomal preparations total/analyzed | 7/4 | 6/4 |
| vesicles | 1089 | 991 |
| tethers | 128 | 236 |
| connectors | 2875 | 3106 |
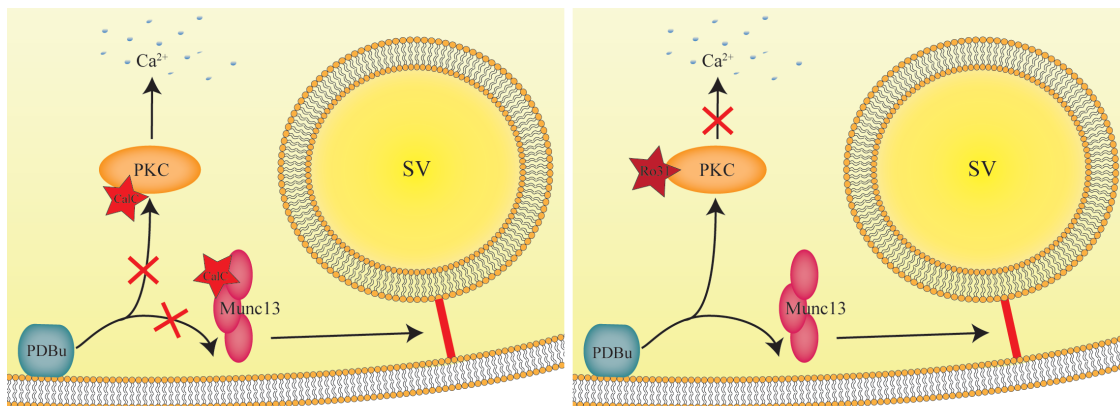


*Figure 29: Pathway of release facilitation illustrating the role of the two antagonists CalC and Ro31.*

While tomograms of control and PDBu-treated samples were recorded with different detectors and microscopes, inhibitor data was with few exceptions acquired with FEI Polara microscope and K2 DDD without VPP. Statistical tests of the inhibitor treatments were performed in respect to PDBu.

Because the antagonist CalC inhibits the activation of PKC as well as the transfer of Munc13 at the presynaptic membrane, it was expected to create a phenotype similar to control samples or possibly influenced by missing activation of PKC and PKC substrates. In Ro31-treated samples, the activation of Munc13 is expected to remain the same as in PDBu-treated samples. Additionally, PKC is deactivated completely and thus might influence the synaptic phenotype in other ways than so far observed. While the treatment with both inhibitors did not result in altered vesicle occupancy relative to the distance from the active zone, the mean distance of SVs to the AZ-membrane was reduced in PDBu- as well as in Ro31-treated synaptosomes compared to control and CalC-samples (see Figure 30). The mean distance is defined as the minimal distance between the voxels representing these membranes.
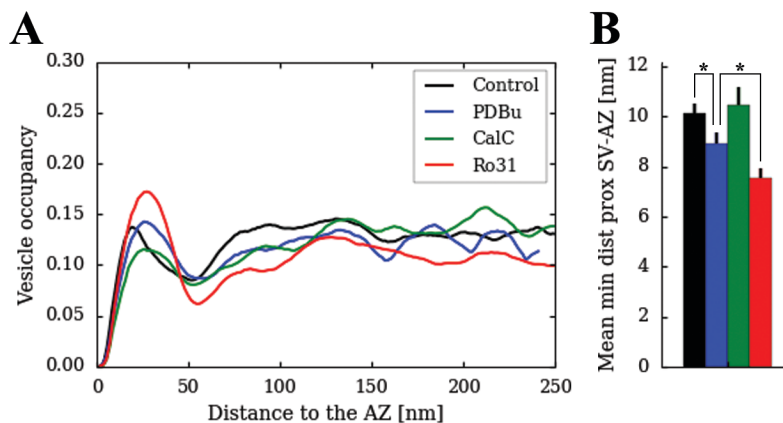


*Figure 30: Mean vesicle occupancy and minimal distance of proximal SVs to the AZ-membrane.*

*A: As for control and phorbol ester treated synaptosomes CalC- and Ro31-treatment does not impede the typical mean vesicle occupancy of the segmented volume. B: The minimal distance of SVs to the AZ-membrane of antagonist-treated synaptosomes hints to altered tethering of SVs.*

The main interest of this analysis was to confirm the structural features of synapses in the state of release facilitation due to a translocation of Munc13 to the presynaptic membrane. Thus, the features of tethering were to be analyzed as performed before for solely phorbol ester treated samples (see Figure 31). Ro31-samples show a strong increase in number of tethers per unit AZ surface area similar to that observed in PDBu-treated samples, while CalC-samples show similar numbers to control samples. Furthermore, mean tether number per SV was equally significantly increased for PDBu- and Ro31-treated synaptosomes. Similarly, the fraction of SVs in the RRP is larger for both treatments, while CalC-treated synaptosomes show no augmentation of RRP-vesicle numbers compared to

Results

control samples. As tethering is increased in PDBu and Ro31-treated synaptosomes, the positive correlation of the AZ-surface area size and the number of tethered SVs had steeper slopes for PDBu and Ro31 samples than for control and CalC samples.
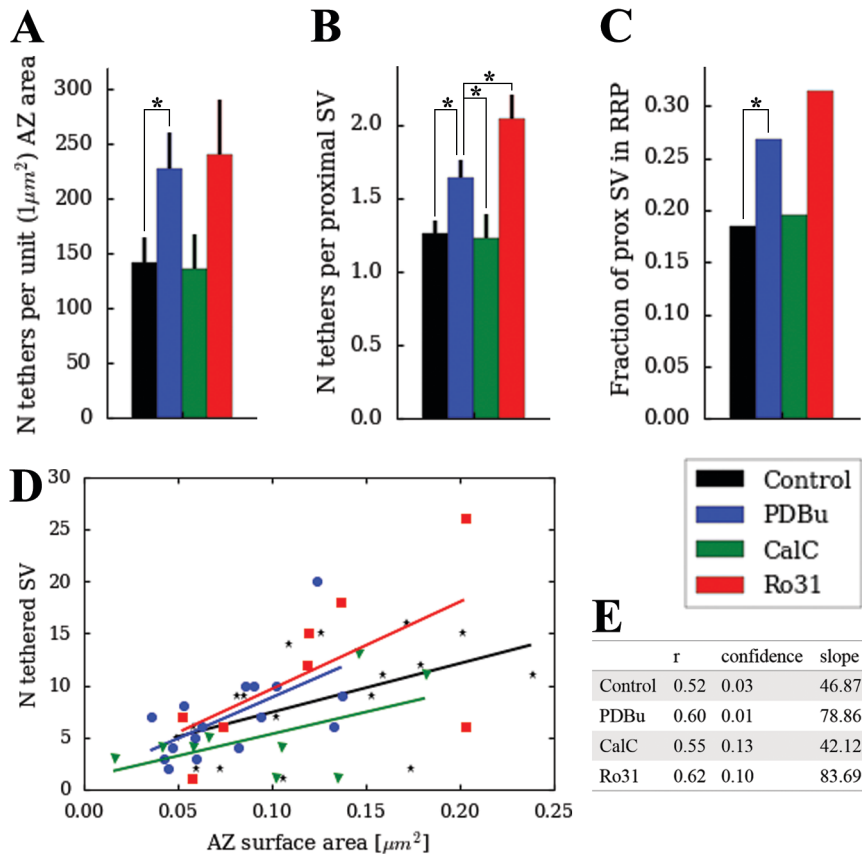


*Figure 31: Tethering in synaptosomes treated with inhibitors of phorbol esters.*

*A: The number of tethers extrapolated for an AZ-surface of 1 $\mu m^2$ is significantly increased for PDBu and increased for Ro31, while CalC samples show similar numbers as controls (mean ± sem CalC = 136.28 ± 31.19, N = 9, p > 0.05; mean ± sem Ro31 = 240.86 ± 49.35, N = 8, p > 0.1; Student's t-test). B: The number of tethers per proximal SVs are equally significantly increased for PDBu and Ro31 with CalC-samples showing similar tether numbers as controls (mean ± sem CalC = 1.23 ± 0.16, N = 87, p < 0.05; mean ± sem Ro31 = 2.03 ± 0.16, N = 118, p < 0.05; K-W-test). C: Consequently, the fraction of proximal in the RRP is significantly increased for PDBu and increased for Ro31, while the fraction of CalC-treated samples is similar to controls (CalC: 0.195, N = 87, p > 0.1; Ro31: 0.314, N = 118, p > 0.1; Chi-square-test). D: There is a positive correlation of the AZ-surface with the number of tethered SVs in healthy synapses, visualized here by control synaptosomes. The slope is equally increased for PDBu and Ro31 with CalC running parallel to control. E: r-, confidence-, and slope values illustrated in D.*

Besides the number of tethers defining SVs to be primed for release and in the RRP, the length of tethers was analyzed for PDBu-treated samples and appeared to be a critical feature of tethers of release facilitated SVs. While we expected tethering to be similar in PDBu- and Ro31-treated samples we were surprised to observe the mean tether length to be

significantly[11] longer after Ro31 inhibiting PKC activity (Figure 32). Synaptosomes under the influence of CalC showed tethers with no significant difference in length to PDBu-treated samples. As a consequence, the fraction of short tethers (< 11 nm) was decreased by PKC inhibition (Ro31) to the control level, while CalC-treated synaptosomes showed a tether length phenotype similar to PDBu-samples. When taking a closer look at the number of tethers for tethered SVs (Figure 32 C and D), it becomes obvious, that CalC does not seem to have a large influence on tether length compared to control samples. PDBu- and Ro31-treated samples on the other hand show a clear increase in short tethers for PDBu and a clear increase in long tethers for PKC inhibited Ro31-samples. This result is confirmed in the number of tethers per 1 $\mu m^2$ AZ surface area (Figure 32 E and F). The segmented tethers for PDBu- and Ro31-treated SVs illustrate the structure of long and short tethers in both states. Shortly tethered SVs in PDBu-samples are endowed with short tethers additional to long tethers, with large volume tethers arranged to fit in the gap between SV and AZ-membrane and also alongside the SV. Ro31-sampes show tethers with rather complex structure stretching away from the SV. When analyzing tether lengths, it has to be kept in mind that tethers are not measured from end to end of an elongated segment but from SV neighboring voxel to membrane voxel. Thus, the actual size of the segment is not always represented in statistics. With the analysis of tether lengths presenting the opposite of what was expected, the influence of PKC on the structures creating tethers of SVs to the AZ-membrane have to be discussed further.

---

[11] Mean tether length: mean ± sem PDBu = 13.1 ± 0.57 nm; N = 270; mean ± sem Ro31 = 16.25 ± 0.66 nm, N = 240, p < 0.001; K-W-test
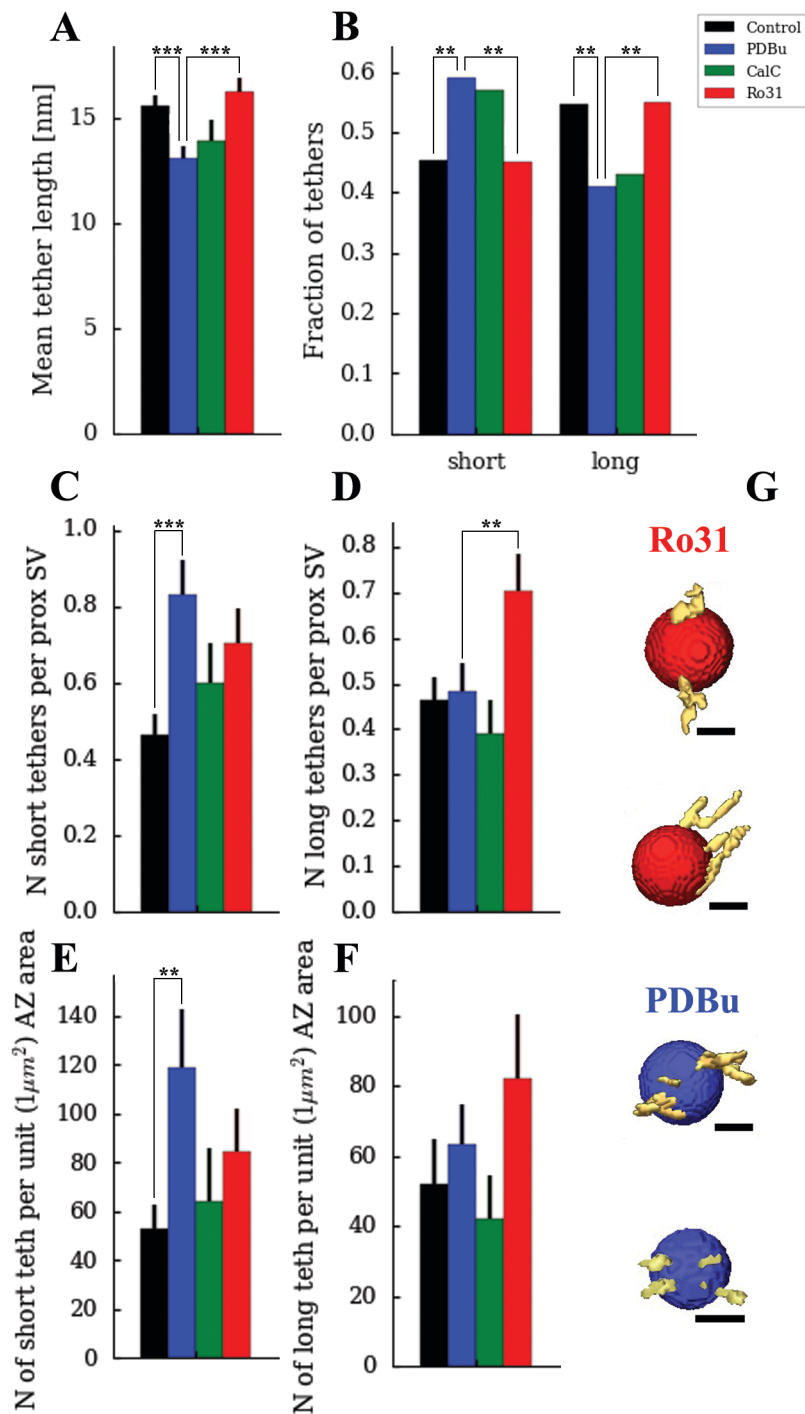
*Figure 32: Tether length in antagonist treated synaptosomes.*

*A: The mean tether length of the sum of tethers is shrunk in PDBu-treated samples but not in Ro31-treated samples with CalC-treated samples showing insignificantly shorter tethers than controls (mean ± sem CalC = 13.98 ± 1.00 nm, N = 107, p > 0.1; mean ± sem Ro31 = 16.25 ± 0.66 nm, N = 240, p < 0.001; K-W-test). B: The fraction of short (< 11 nm) tethers is significantly increased for PDBu-treated specimen while the fraction of short tethers in Ro31-samples is significantly smaller. The fractions of long tethers behave vice versa with CalC-treated synaptosomes showing tethers in the size range of PDBu-treated samples (short tether fractions control: 0.453, N = 212, PDBu: 0.591, N = 215, p < 0.01; CalC: 0.570, N = 86; p > 0.5; Ro31: 0.452, N = 166, p < 0.01; long tether fractions control: 0.547; PDBu: 0.409, p < 0.01; CalC: 0.430, p > 0.5, Ro31: 0.548, p < 0.01). C: PDBu-treated synaptosomes show significantly more short tethers per proximal SV (mean ± sem control = 0.46 ± 0.06, N = 228; mean ± sem PDBu = 0.83 ± 0.09, N = 164, p < 0.001; K-W-test; mean ± sem CalC = 0.60 ± 0.10, N = 87; mean ± sem Ro31 = 0.70 ± 0.09, N = 118). D: Ro31-treated-samples show significantly*

*more long tethers per proximal SV compared to PDBu-treated samples (mean ± sem control = 0.46 ± 0.05, N = 228; mean ± sem PDBu = 0.48 ± 0.06, N = 164, mean ± sem CalC = 0.39 ± 0.07, N = 87; mean ± sem Ro31 = 0.70 ± 0.08, N = 118, p < 0.001; K-W-test). **E**: The number of short tethers per unit AZ surface area is significantly increased for PDBu compared to controls and inhibitor treatments (mean ± sem control = 52.57 ± 10.07, N = 17; mean ± sem PDBu = 118.61 ± 23.97, N = 16, p < 0.1; K-W-test; mean ± sem CalC = 64.37 ± 21.77, N = 9; mean ± sem Ro31 = 84.22 ± 17.77, N = 8). **F**: The number of long tethers per unit AZ surface area is increased for Ro31 in and insignificant way (mean ± sem control = 52.21 ± 12.54, N = 17; mean ± sem PDBu = 63.53 ± 11.18, N = 16, mean ± sem CalC = 41.96 ± 12.40, N = 9; mean ± sem Ro31 = 82.02 ± 18.20, N = 8). **G**: Representative proximal SVs with tethers from Ro31-samples show long, complex tethers, while tethered SVs from PDBu-samples show additional short tethers with long tethers folded and rearranged to fit in the gap between AZ-membrane and tethered SV.*

In the last chapter with exclusive assessment of the effect of PDBu on synaptosomes, the focus was put on tethering and release priming. For treatments with antagonists of phorbol ester CalC and Ro31 connectivity of SVs was observed as well. PDBu itself has an effect on connectivity, specifically on the number of connectors per SV and on the connector length. While connectors are significantly longer in the proximal zone to the presynaptic membrane the connector length is conform between PDBu- and control samples in the distal zones. While the fraction of connected SVs is similar in PDBu-samples and control samples, PDBu-treated synapses show a lower number of connectors per SV, especially for non-tethered SVs. For inhibitor-treatments, a higher fraction of connected SVs was observed, and connectivity was especially high for tethered SVs of Ro31-treated samples. For the same group of SVs (tethered, Ro31), the number of connectors per SV was significantly increased relative to PDBu-treated samples. Overall, CalC- and Ro31-treated samples revealed SVs with a higher number of connectors compared to PDBu. Because PKC has low activity in CalC-treated samples but is completely inactivated by ATP deprivation in Ro31- samples, the phenotypes were expected to show differences. These differences are prominent amongst other results in the connector length measured relative to the distance from the AZ. Connecting structures in control synapses become shorter with the closer distance to the presynaptic membrane, connectors in Ro31-treated synaptosomes behave vice versa. Ro31-connectors become longer, the closer to the AZ. PDBu-treated samples showing a similar but milder phenotype.

This might suggest that a specific species of connecting proteins is still prevalent in proximity to the AZ in Ro31-treated synapses while the same species is cleaved of in the physiological state. In the same plot the increasing connector length in PDBu-treated samples in the proximal and intermediate zone may indicate that a translocation of Munc13 to the presynaptic membrane equally influences connectivity of SVs.
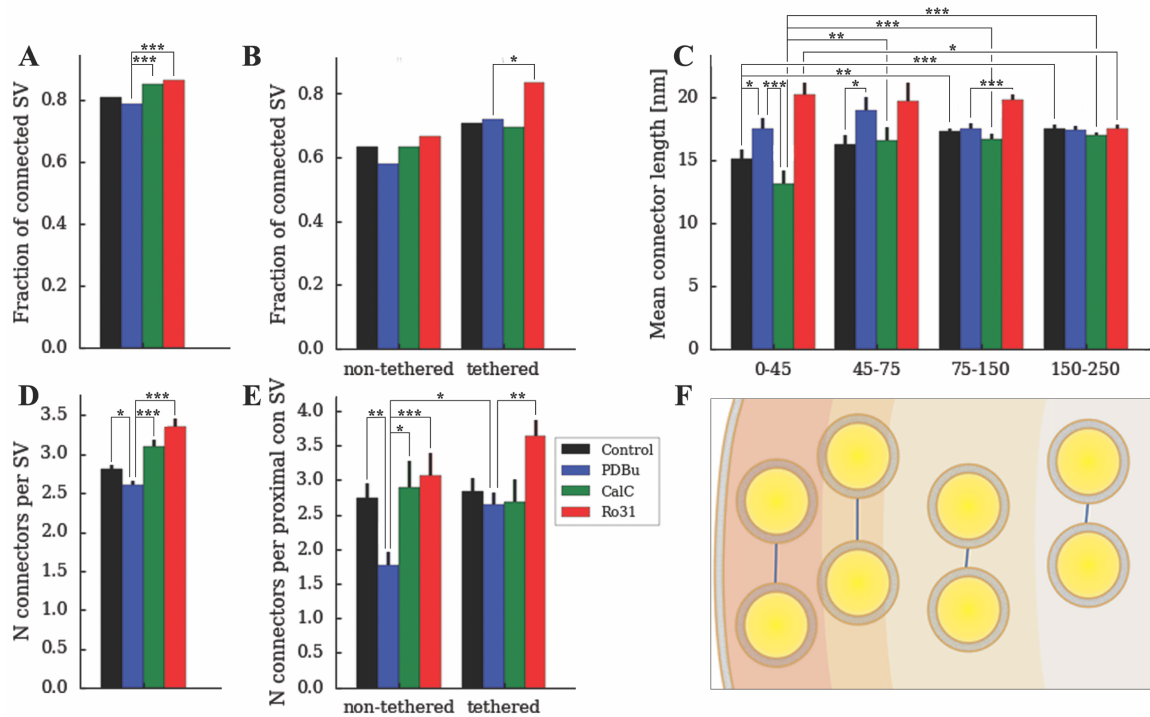
*Figure 33: Connectivity in synaptosomes treated with PDBu and its inhibitors CalC and Ro31.*

*A: A larger fraction of SVs are connected in PKC-deactivated synaptosomes with CalC- or Ro31-treatment (control: 0.808, N = 2115; PDBu: 0.789, N = 1450, p > 0.1; CalC: 0.852, N = 1089, p < 0.001; Ro31: 0.863, N = 991, p < 0.001; Chi-square test).*

*B: The fraction of connected SVs is larger for tethered SVs of Ro31- treated samples (non-tethered SVs, control: 0.634, N = 82, PDBu: 0.580, N = 50, CalC: 0.634, N = 41, Ro31: 0.667, N = 27; tethered SVs, control: 0.705, N = 146, PDBu: 0.719, N = 114, CalC: 0.696, N = 46, Ro31: 0.835, N = 91, p < 0.05; Chi-square test).*

*C: The mean length of connectors relative to the distance from the active zone, in the proximal, the intermediate and distal zone 1 and 2 (proximal zone: control mean ± sem = 15.15 ± 0.66 nm, N = 198, PDBu mean ± sem = 17.53 ± 0.87 nm, N = 135, p < 0.05, CalC mean ± sem = 13.15 ± 1.05 nm, N = 69, p < 0.001, Ro31 mean ± sem = 20.27 ± 0.93 nm, N = 161; intermediate zone: control mean ± sem = 16.22 ± 0.82 nm, N = 162, p < , PDBu mean ± sem = 18.97 ± 1.10 nm, N = 110, p < 0.05, CalC mean ± sem = 16.61 ± 1.06 nm, N = 72, p < 0.01 to CalC, Ro31 mean ± sem = 19.69 ± 1.46 nm, N = 53; distal zone 1: control mean ± sem = 17.29 ± 0.28 nm, N = 1200, p < 0.01 to control, PDBu mean ± sem = 17.55 ± 0.34 nm, N = 725, CalC mean ± sem = 16.68 ± 0.39 nm, N = 568, p < 0.001 to CalC, Ro31 mean ± sem = 19.83 ± 0.45 nm, N = 496, p < 0.001; distal zone 2: control mean ± sem = 17.56 ± 0.24 nm, N = 1431, p < 0.001 to control, PDBu mean ± sem = 17.43 ± 0.30 nm, N = 904, CalC mean ± sem = 16.96 ± 0.29 nm, N = 990, p < 0.001 to CalC, Ro31 mean ± sem = 17.55 ± 0.31 nm, N = 978, p < 0.05 to Ro31; K-W-test).*

*D: The number of connectors per SV is slightly but significantly decreased for PDBu-treated samples and highly significantly increased for CalC- and Ro31- treated samples (control mean ± sem = 2.80 ± 0.05, N = 2115; PDBu mean ± sem = 2.60 ± 0.06, N = 1450, p < 0.05; CalC mean ± sem = 3.10 ± 0.08, N = 1089, p < 0.001; Ro31 mean ± sem = 3.36 ± 0.09, N = 991, p < 0.001; K-W-test).*

*E: The number of connectors per proximal connected SV are shown here relative to tethering with non- tethered SVs showing reduced number of connectors for PDBu-treated samples and tethered SVs showing increased number of connectors for Ro31-treated synaptosomes (non-tethered SVs: control mean ± sem = 1.73 ± 0.20, N = 82, PDBu mean ± sem = 1.02 ± 0.17, N = 50, p < 0.05 to controls, p < 0.01 to PDBu, CalC mean ± sem = 1.83 ± 0.33, N = 41, Ro31 mean ± sem = 2.04 ± 0.36, N = 27, p < 0.05; tethered SVs: control mean ± sem = 1.99 ± 0.17, N = 146, PDBu mean ± sem = 1.89 ± 0.17, N = 114, CalC mean ± sem = 1.87 ± 0.29, N = 46, Ro31 mean ± sem = 3.03 ± 0.24, N = 91, p < 0.001; K-W-test).*

*F: Scheme of connector lengths relative to the AZ membrane, to illustrate plot C.*

To sum up, we showed that a visualization of release facilitation by cryo-EM is possible. Our data shows that the number of tethers is increased by the application of PDBu, likely in a Munc13-dependent manner. These results parallel the release facilitation determined by the glutamate release assay. While the number of tethers binding the presynaptic membrane increase stronger than the number of tethered SVs it becomes apparent that the number of tethers per SV is the most critical factor for priming SV for release. With an average of more than two tethers per SV, PDBu-treated synaptosomes show an increased ratio of SVs in the RRP. These findings could be confirmed by applying treatments with both PKC inhibitors.

Our data shows that the tether length is regulated by PKC. While PDBu-treated synaptosomes show a peak in 6 nm-tethers, Ro31-treated synaptosomes show a higher ratio of long tethers. This may be an indication that PKC is required to convert SVs from long to short tethering structures or to catalyze cleaving off long tethers. Additionally, it suggests that the number of tethers is more critical for release facilitation than the tether length, since Ro31-treated synaptosomes are equally release facilitated as PDBu-treated synaptosomes. For exclusively PDBu-treated samples the prominent accumulation of tethers of 6 nm length points out that the tethering structure established with the help of Munc13 is in that range of size. Furthermore, the lack of a peak in the longer size range of the tether length histogram suggests the short-term existence of PDBu-Munc13-complexes, which should be in the size range of 20 nm.

When observing connectivity in all data sets, interesting features can be observed. While PDBu reduces the number of connectors of SVs close to the AZ and equally increases the connector length we can assume that short connectors existing in control synaptosomes are reduced in PDBu-samples. The latter was confirmed by CalC- and Ro31-treatment but surprisingly connectivity is overall higher in both inhibitor treatments and specifically for tethered SVs in Ro31-treated synapses. Here lies the main difference between PKC-inhibited phenotype (CalC) and PKC-deactivated (Ro31) phenotype, suggesting that PKC is crucial for catalyzing connectors to be cleaved off SVs close to the AZ. The Phenotypes of all treatments are summed up schematically in Figure 34.
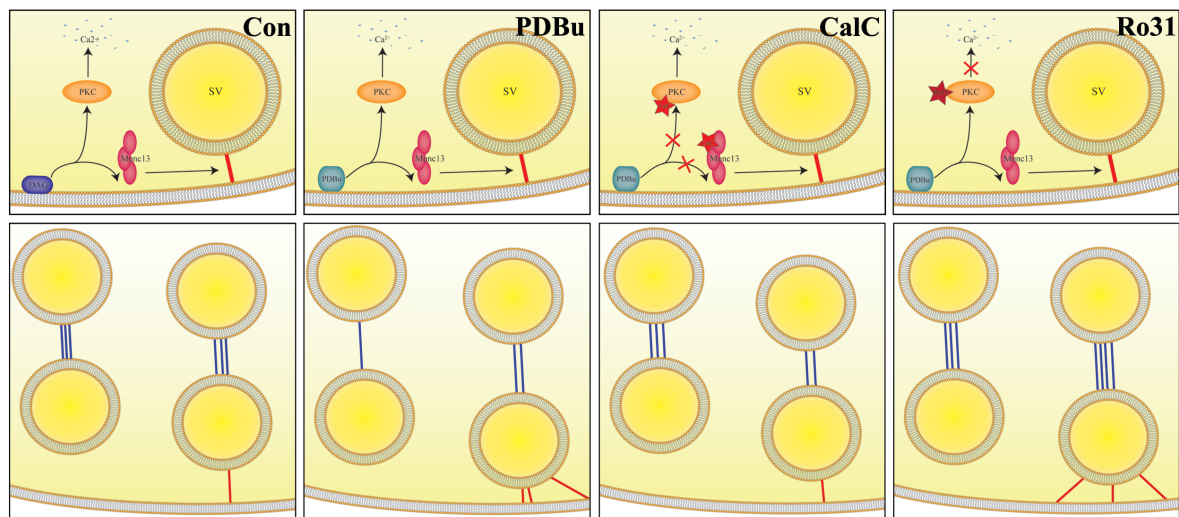
Results



*Figure 34: Schematic summary of the synaptosome analysis.*

*The four different pathways of control and treated synaptosomes created four different phenotypes of SV tethering and connectivity. While PDBu-treated samples show more short tethers and longer and fewer connectors relative to controls, CalC- and Ro31-treated synaptosomes both show increased connectivity. The inhibitor treatments show similar number of connectors but differ in connector length. While tethering of CalC-SVs is comparable to control SVs, Ro31-SVs are equally shortly tethered to the AZ membrane but by fewer short tethers and multiple long tethers.*

While the statistical data collected from isolated synaptic connections was very helpful to understand the crucial structural features of transmitter release facilitation, the results should be confirmed by investigating the same features in samples closer to the physiological environment of a synapse. This analysis was performed with primary cultured neurons, as will be shown in the following chapter.

## 4.3 Analysis of cryo fibbed cultured neurons

The ultimate goal of preparing cultured neurons from hippocampal cells was the collection of tomography data for the analysis of release facilitation in the close to physiological state. Since the data acquisition was and is still impeded by problems during sample preparation and synapse localization in TEM, the tomograms acquired were additionally used to investigate features of axonal processes. In the end a small statistical analysis was possible but has to be handled with care due to small data sets.

### 4.3.1 Redeposition and contamination on fibbed primary cultured neurons

Previously recorded synapses from culture captured in CET seemed to be immature and small in size (Lučić et al., 2007). Here, cultures were investigated at DIV 21 to allow mature synapses to form. Mature synapses formed between primary cultured neurons are often in a range of 1 μm in thickness. In order to record tomograms close to cell bodies, where synapses are concentrated, it was necessary to thin the samples before acquiring tomograms. While methods formerly used for sample thinning created artefacts, such as compressed synaptic vesicles after vitreous sectioning of organotypic hippocampal culture (Fernández-Busnadiego et al., 2010; Lučić et al., 2013), focused ion beam milling does not impact the tissue structure (Rigort et al., 2012).

The initial strategy for culture milling was to seed cells in a rather low density (3.0 x $10^5$ cells/well) to make sure for proper vitrification during plunging. However, the ice thickness obtained rendered lamella milling rather impossible, because thin ice and low density of biomaterial renders a lamella very unstable. Figure 35 G shows a lamella milled from this culture. Thus, wedge milling was a more promising strategy, but also bearing complications. Since cells do not exclusively grow one-sided but often on both sides of the carbon film (Figure 35 E), one-sided milling cannot reliably thin the sample sufficiently. Obtaining a thin wedge required milling at a very low angle. That in turn often leads to milling of biomaterial from grid bars (Figure 35 F) and thus increasing redeposition. Wedges milled too thick for TEM are reflecting electrons in SEM images, appearing as a characteristic bright surface (Figure 35 D). Consequently, the cell culture seeding density was increased to a density of 6.0 x $10^5$ cells/well. This density was suitable for lamella

milling, even though it caused crystalline ice to form in parts of the sample. In this way, lamellas of a sufficiently large surface and stability could be produced (Figure 35 H).

Aside from sample density, redeposition of gallium and milled biomaterial was to be tackled by different milling strategies. This redeposition accumulated as electron dense granules on the backside of the neuronal cells in reference to the ion beam source (Figure 35 A and B). There was no difference in intensity of redeposition in lamellas and wedges, so the milling angle as (typically $\iota = 5°$ for wedges and $\iota = 11°$ for lamellas) a major difference between the two strategies did not significantly influence the formation of redeposition. Changing the width of the milled surface (30 μm for wedges and 15 μm for lamellas) also did not affect the redeposition. Platinum applied by sputtering or GIS was no source of redeposition and omitting the step did not solve the redeposition problem either. We came to hypothesize that the granules visible on the samples are milled biomaterial and gallium. This redeposition seems to be strongest in samples with highly uneven surface and high ratio of plasma membrane exposed to the ion beam.

Because milling angle and width did not affect redeposition intensity, we chose cleaning cross section (CCS) as the standard milling method for neurons. Biomaterial is removed by the ion beam in a line by line approach, ablating material in one line thoroughly before milling the next line in the pattern. Also, with this strategy, the redeposition could not be significantly reduced.

Since tomograms showed a reasonably good quality revealing structural details of neuronal processes and synapses, data was usable despite artifacts arising from surface contamination (Figure 35 C). Redeposition was limited to the surface (Figure 36 A) of the sample and not implanted into ice or neurons, thus a software-based method of contamination removal could be employed without disturbing valuable information in the data.
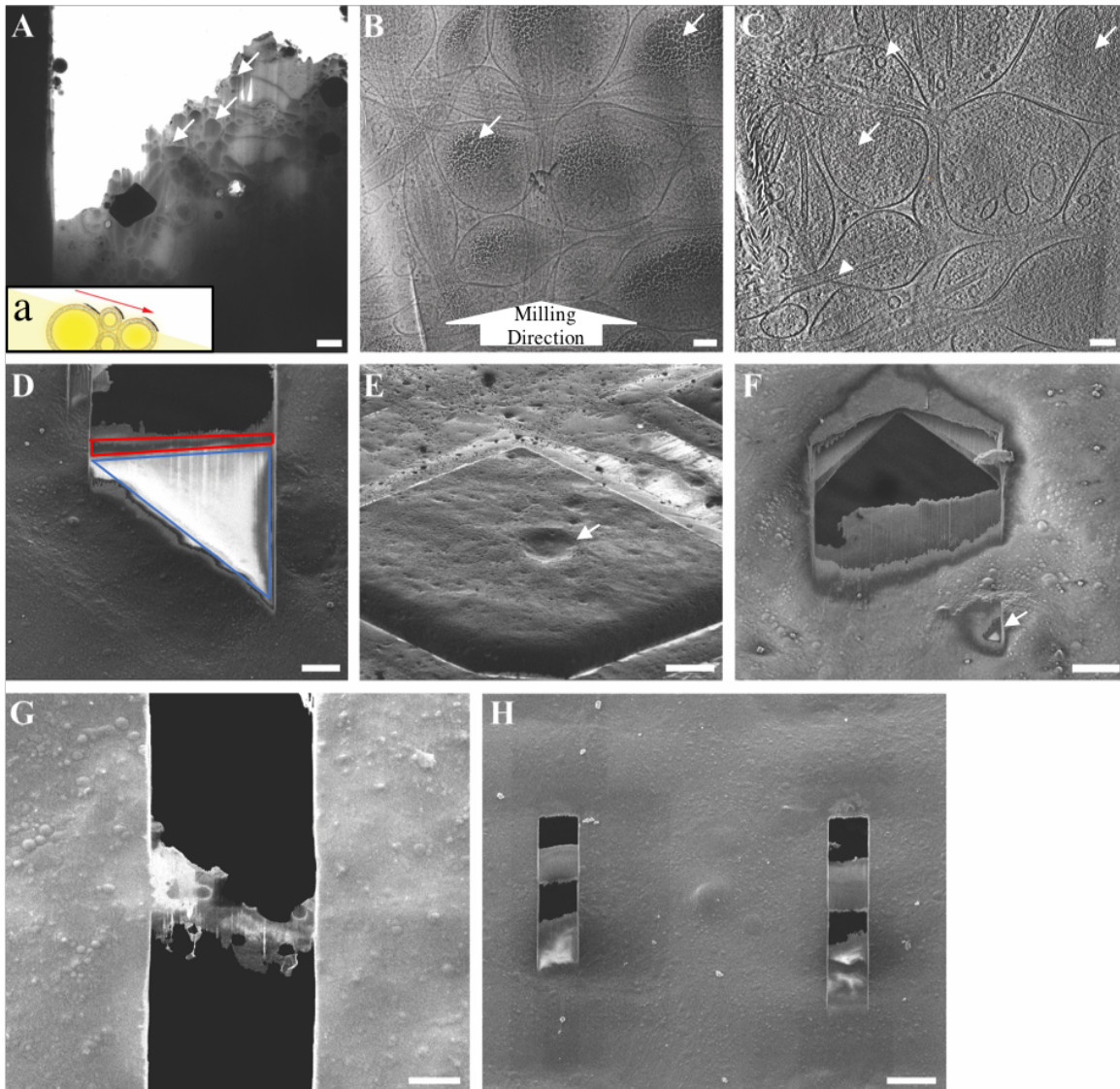
*Figure 35: Focused ion beam milling of primary cultured neurons.*

*The top panels illustrated the incidence of contamination in respect to the milling direction. Redeposition occurred on the backside of the biological material, opposite of the ion source. Panel **A** shows a wedge in TEM with processes clearly visible due to redeposition (arrows) resting on them (Scale bar: 1 µm). Inset **a** schematically depicts redeposition accumulating on the backside of plasma membranes opposite of the ion beam. Panel **B** shows a projection TEM image of the same tissue as can be seen in a tomographic slice in C. The milling direction is indicated in B with redeposition (arrows) sitting in the ion beam shadow (scale bar: 100 nm). **C** shows ripple-like artifacts (arrows) occurring due to redeposition, but still synaptic vesicles and densities inside microtubules (arrowheads) are visible (scale bar: 100 nm).*

*The middle panels show wedge milling on neuronal cultures in SEM (scale bars: 10 µm). Panel **D** shows bright appearance of the wedge in the electron beam, which is too thick for TEM imaging (thick area enclosed in blue, thin area enclosed in red). Panel **E** shows neurons growing on the backside of the grid. One-sided wedge milling is unable to thin a sample shown in E. Panel **F** illustrates a source of redeposition: the ion beam hitting material on the grid bar (arrow) before it reaches the wedge area, thus dispersing milled material over the wedge.*

*The lower panels show lamella milling of neurons in SEM. While **G** shows a lamella milled from a grid of medium thickness (scale bar: 5 µm), **H** shows lamellae milled from very thick ice, barely possible to be vitrified (scale bar: 20 µm)*

## 4.3.2  Removal of contamination artifacts from tomograms

The fine processes of primary neuronal cultures forming a network on the grid create a highly uneven surface, which turned out to be prone to the material redeposition shown in the previous section. As it can be seen in Figure 35, tomograms presented neuronal features despite surface contamination, but even mild contamination creates stripe artifacts similar to those formed by fiducial markers. The artifacts are strongly visible as streaks in y-slices perpendicular to the tomography tilt axis creating a high-frequency pattern (see Figure 36 A) and form ripples in z-slices (see Figure 36 E). To analyze this data for fine details like filaments without misinterpretation of artifacts, the tomogram cleaning procedure was developed specifically for this purpose (Fernandez et al., 2016). In short, surface contamination was masked, re-projected and subtracted from the original tilt series. The subtracted tilt images were then used to reconstruct an improved tomogram. This procedure was repeated iteratively to create a cleaned version of the tomogram. The masked-out area is visible in y-slices as well as a strong reduction in streak artifacts (see Figure 36 B). A closer look at the mitochondrion shows the cristae free of ripples after tomogram cleaning procedure proving that valuable information remains unimpaired.
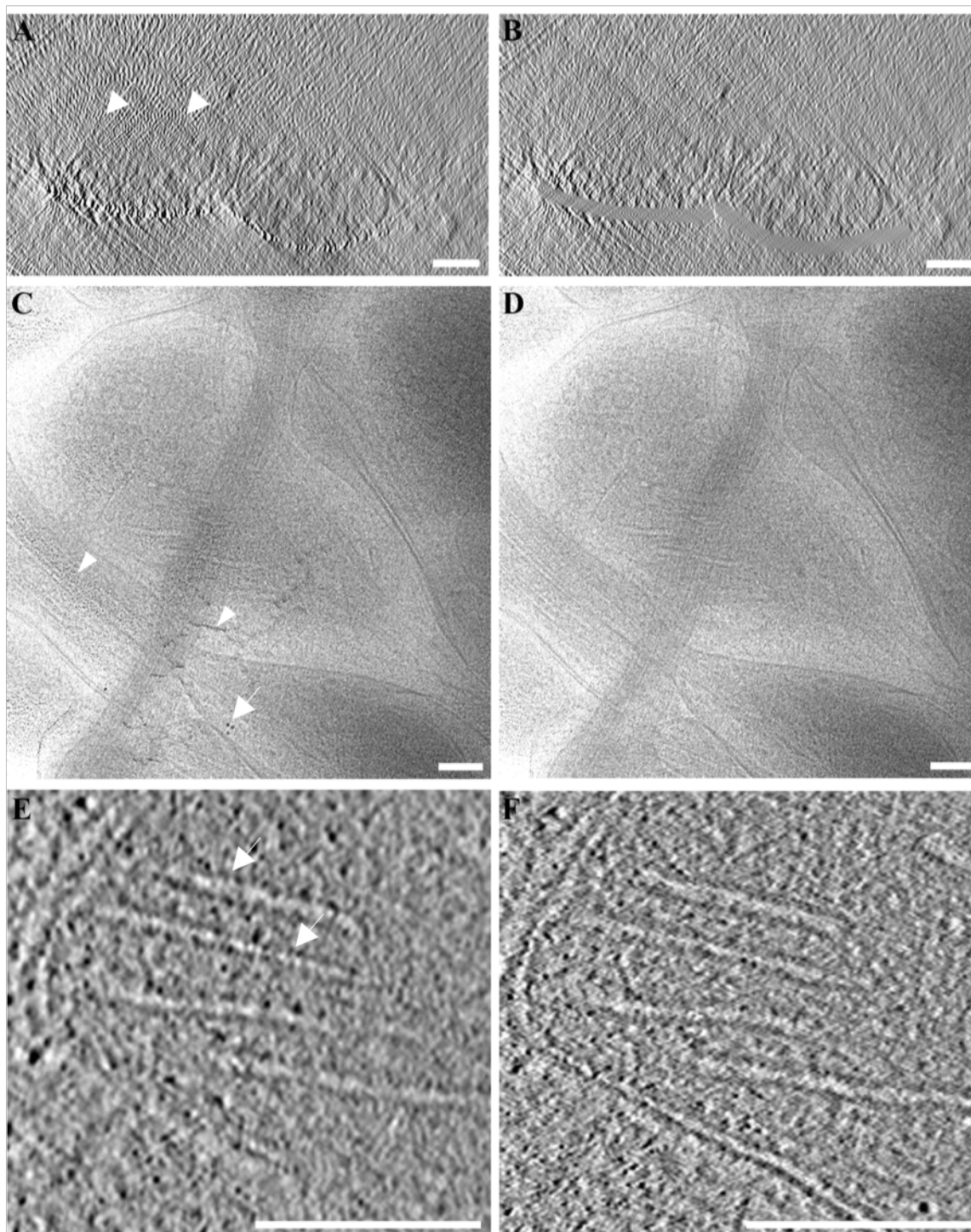
*Figure 36: Tomogram cleaning and removal of artifacts.*

*A: y-slice of a tomogram with a layer of redeposition sitting on the neuronal cells and the resulting ripple artifacts (arrows). B: Contamination was masked, and tomogram was reconstructed with redeposition subtracted. C and D: Zero-degree tilt-series image with redeposition (arrowheads) and gold markers and reprojected tilt-series after cleaning procedure without redeposition and markers. E and F show z-slices of the tomogram at the mitochondrion before (E) and after (F) tomogram cleaning procedure. Ripple shaped artifacts are indicated by arrows in E.  Scale Bars: 100 nm*

### 4.3.3  Structure of neuronal processes

While the target of this project, imaging synapses in primary cultured neurons, was barely feasible, we recorded tomograms of swellings of neuronal processes containing clusters of vesicles and organelles. While these regions of neurons were previously imaged without ion beam milling, they were frequently recorded within the area of lamellae or wedges, because they could not be distinguished from synapses in projection images. These tomograms nevertheless revealed interesting networks of vesicles and other structures like microtubules and mitochondria. While this thesis studies connecting filaments of synaptic vesicles intensively, the focus of this analysis was laid on structures organizing clusters of dense core granules.

In neuronal processes, piccolo-bassoon transport packages (PTV) (Zhai et al., 2001); (Shapira et al., 2003); (Dresbach et al., 2006) and synaptic vesicle protein transport vesicles (STV) (Bury and Sabo, 2016) are vesicular structures known to cargo active zone scaffolding proteins and synaptic vesicle proteins. While the PTVs are morphologically identified as dense-core vesicles of 80 nm in diameter (Shapira et al., 2003), STVs are thought to be of clear lumen (Tao-Cheng, 2007) and different sizes and shapes. In our data, we detected vesicle-shaped dense core granules that were smaller (see plot H in Figure 37) than the average synaptic vesicle to be found either in synaptic terminals or axonal varicosities. Those granules were connected to smooth endoplasmic reticulum (SER) as well as microtubules and formed packages of granules. The size of the granules was very uniform with a diameter of $31.89 \pm 3.4$ nm smaller than clear lumen synaptic vesicles within the same axonal swelling ($44.36 \pm 5.2$ nm) and vesicles located at the synaptic terminal ($39.06 \pm 5.8$ nm). Granules were found to be connected to microtubules and SER by several linkers, a structure which has yet to be identified. Furthermore, synaptic vesicles located in this specific varicosity were located in a separate vesicle pool from the dense-core granules. This agglomeration of synaptic vesicles on the sack-shaped compartment of this axonal swelling is another indicator for the hypothesis that synaptic formation happens rather in sack- than spindle-shaped varicosities. Thus, a step towards maturation of a presynaptic bouton might be observed here with no obvious site of AZ-formation yet.
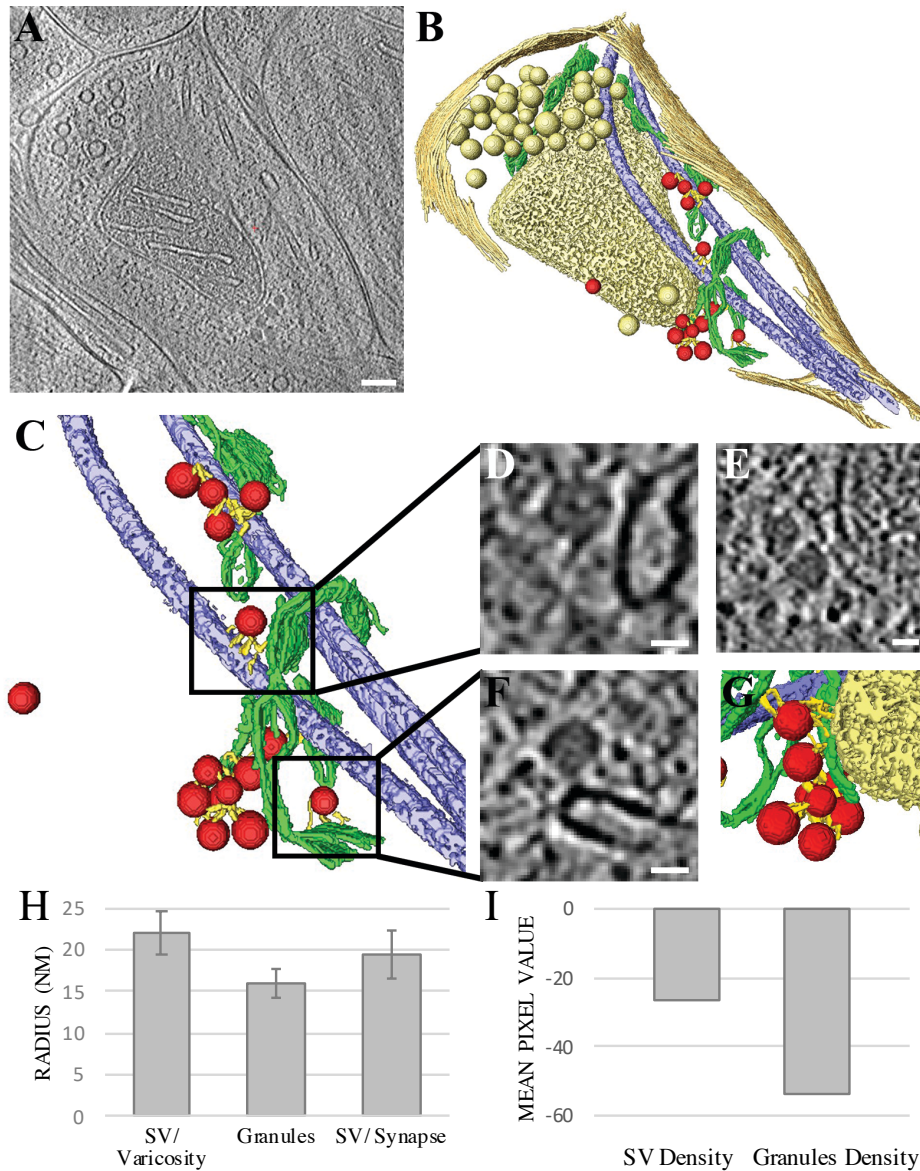
*Figure 37: Bouton of a neuronal process.*

*A: tomographic z-slice of a neuronal process containing synaptic vesicles, mitochondrion, microtubules as well dense granules is depicted in A (Scale bar: 100 nm). Segmentation of the tomogram (B) illustrates the localization of dense granules segmented in red, as well as synaptic vesicles, mitochondrion and the plasma membrane (yellow). A closer look shows (C) granules located closely to smooth ER (green) and microtubules (light purple) as well as connected to these structures (segmented in yellow). D and F show details in z-slices corresponding to segmented structures in rectangles. E and G show dense granules connected to smooth ER close to the mitochondrion in z-slice and the segmented volume. Plot H shows radii of synaptic vesicles in varicosities compared to those located at synapses in comparison to dense core granules, plot I illustrated the mean pixel values of granules compared to varicosity vesicles. Scale bar of D, E and F: 20 nm*

Results

### 4.3.4 Synapses in primary cultured neurons

*For the following analysis, tomography data of immature and untreated synapses was kindly provided by Dr. Yoshiyuki Fukuda.*

To confirm the analysis of synaptosomes presented in previous sections, release facilitation evoked by phorbol ester treatment was investigated in primary cultured neurons. Neurons collected from embryonal hippocampal tissue were grown on EM grids. They formed networks of neurites and survived at least until DIV 21. To visualize formation of synapses between neuronal processes immunolabelling against Munc13 and PSD-95 as well as Phalloidin staining was performed (Figure 38). Signals show the presence of both proteins being important synaptic players are dispersed over the whole process but highly localized in puncta. As can be observed in the upper row of images, Munc13 co-localized with PSD-95 throughout processes, but Munc13 also infiltrates finer neurites, which don't show any staining against PSD-95. The immunofluorescence data indicated that precise targeting of FIB milling to a specific fluorescent spot was not necessary. Furthermore, correlative procedures that account for z-positioning were not developed at the time.
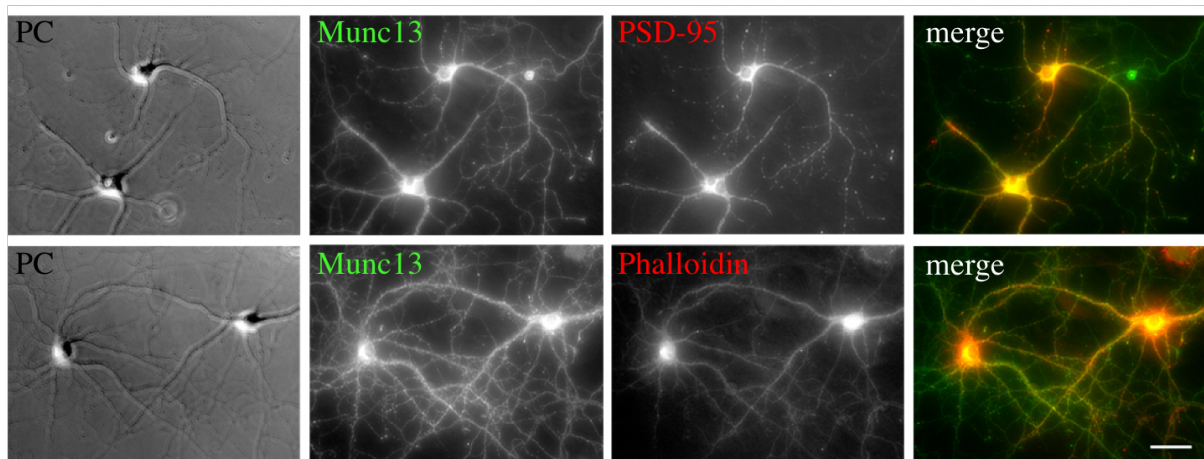


*Figure 38: Immunolabelling of primary cultured neurons.*

*The first column shows phase contrast (PC) light microscopy images of two neuronal cell bodies with neurites grown to contact. Munc13-labelling in the second column shows an overall dispersed signal but also puncta in the lower image, indicating localization for synapse formation. The third column depicts PSD-95 and Phalloidin labelling respectively with puncta of PSD-95 localization on dendrites. The fourth column shows an overlay of both channels with Munc13-signal in green and PSD-95/Phalloidin in red. Scale bar: 50 µm*

While tomography of unfibbed samples prepared before this project, showed mainly synapses in an early state in development, samples thinned by FIB in the course of this project enabled us to record data from mature synapses. Figure 39 depicts mature synapses (A and B) compared to immature ones (C) lacking a clear electron dense synaptic cleft and a postsynaptic density with the presynapse only sparsely endowed with synaptic vesicles. Despite the poor display of typical synaptic features, immature synapses were distinguishable by events of membrane fusion at the presynaptic membrane. In comparison, mature synapses depicted in Figure 39 A and B are densely packed with synaptic vesicles and show a clear and electron dense synaptic cleft as well as the postsynaptic electron dense protein network.
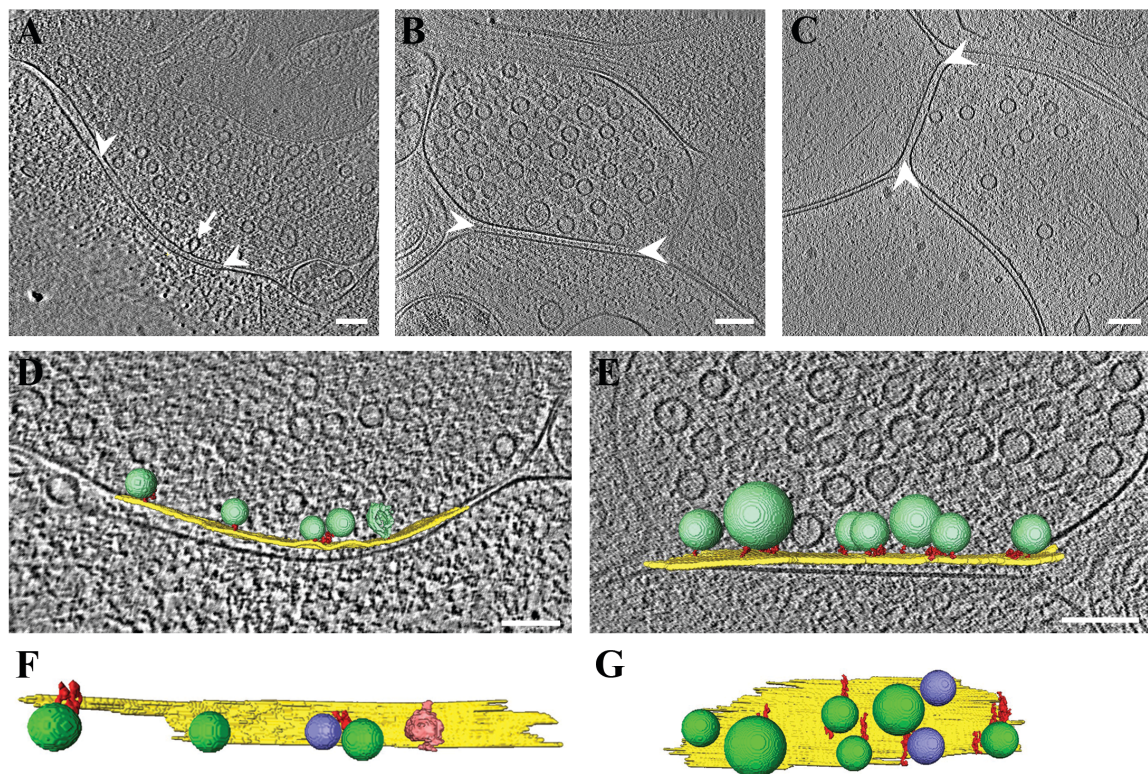


*Figure 39: Synapses in primary cultured neurons.*

*The top panels show slices of tomograms with arrowheads indicating the dimensions of the synaptic connections. **A** and **B** show mature synapses recorded from cryo fibbed neurons with a densely filled presynaptic compartment, an electron dense synaptic cleft and a postsynaptic density. **C** shows an immature synapse, which lacks the typical features like an electron dense cleft or the PSD but has tethered and releasing vesicles as well as the typical cleft interspace size. The latter was recorded from unfibbed neuronal samples. The second panels show both mature synapses (**A** and **B**) with segmented membrane at the AZ and tethered vesicles as well as a release event in **D**. (Scale bars: 100 nm). **F** and **G** show SVs tethered to the membrane at the AZ in color code. Purple SVs are shortly tethered (0-5 nm) and green SVs are tethered in medium length (5-10 nm). The release event is segmented in pink.*

Results

Figure 40 illustrates the quantification of synaptic features depending on the state of synaptogenesis. It confirms the lack of proximal SVs in immature synapses and the resulting decrease in tether number per AZ surface area. Additionally, the number of tethers per tethered SVs are reduced before a synapse reaches full maturity. Because the mean tether length is similar in both states of development, it can be assumed that similar species of tethering filaments exist in both. Connectors on the other hand, are overall reduced in number and also show a strong difference in length, indicating that a short connecting protein does not exist yet in immature synapses.
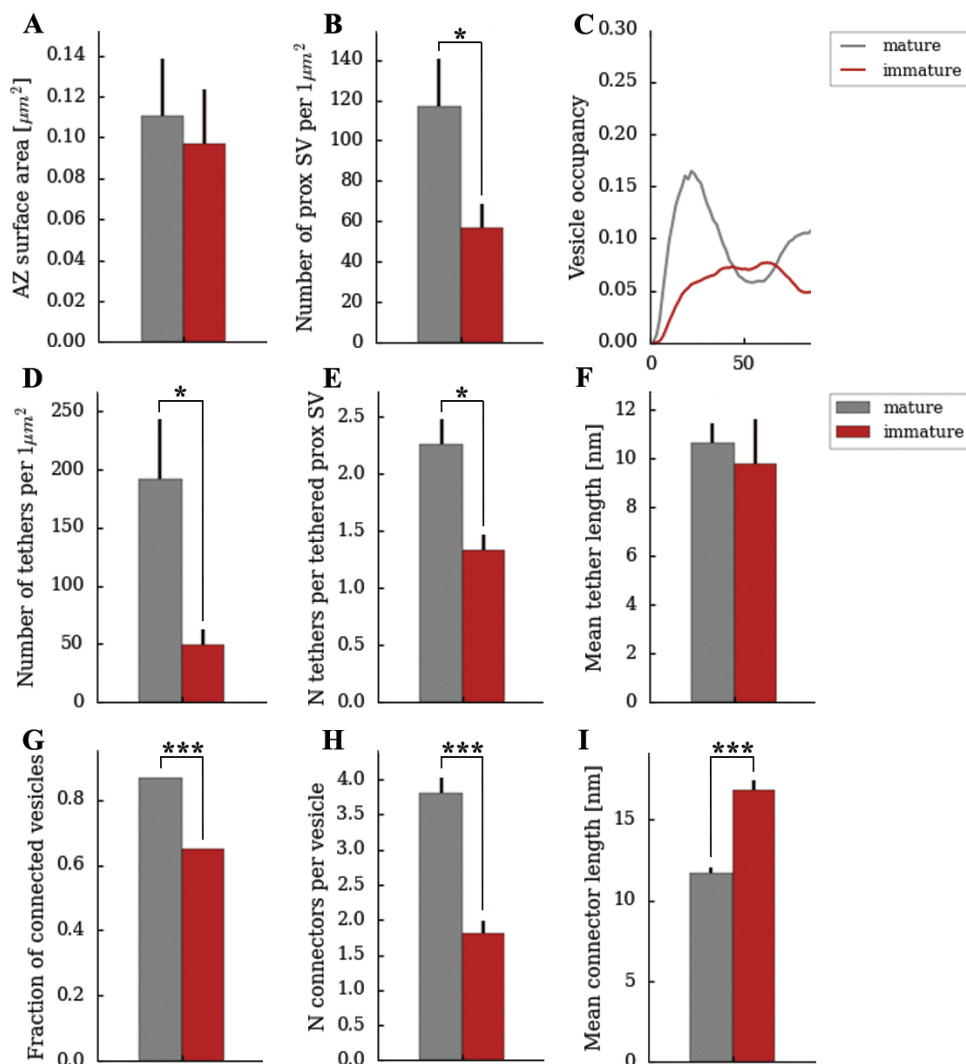


*Figure 40: Quantification of features of immature and mature synapses.*

*A: The AZ-surface of immature synapses reached the average size of a mature synapse of 0.1 μm². B: There is a 50%-reduction in number of proximal SVs in immature synapses (Mature mean ± sem = 116.63 ± 23.48, Immature mean ± sem = 56.62 ± 11.9, p<0.1, t-test) , also visible in a dip in vesical occupancy in the proximal zone to the AZ in C. D: Since proximal SVs are missing, the number of tethers per 1 μm² are strongly reduced in immature synapses (Mature mean ±*

*sem = 191.33 ± 51.38, Immature mean ± sem = 48.85 ± 14.06, p<0.1, t-test). **E**: Even tethered SVs show a reduced number of tethers per SV (Mature mean ± sem = 2.26 ± 0.21, n = 39, Immature mean ± sem = 1.33 ± 0.13, n = 15). **F**: The mean tether length is similar in both maturation phases, indicating the same species of tethers exist in both (Mature mean ± sem = 10.66 ± 0.80 nm, n = 90, Immature mean ± sem = 9.77 ± 1.82 nm, n = 20). **G**: Connectivity is overall reduced in immature synapses illustrated by a lower fraction of connected SVs (Fraction Mature = 0.865, n = 200, Fraction Immature = 0.649, n = 188, p<0.001, Chi-square-test) and by a reduced number of connectors per SV in **H** (Mature mean ± sem = 3.81 ± 0.21, n = 200, Immature mean ± sem = 1.81 ± 0.17, n = 188, p < 0.001, K-W-test) . **I**: The strong difference in mean connector length indicates a lack of a species of short connectors in immature synapses (Mature mean ± sem = 11.7 ± 0.34 nm, n = 545, Immature mean ± sem = 16.86 ± 0.54 nm, n = 275, p < 0.001, K-W-test). (N: mature = 4, immature = 5)*

Despite different states of development, both datasets gave an insight into synaptic activity of primary cultured neurons. In comparison, synaptic connections in culture seem to be more active than those in isolated synaptosomes. Figure 41 depicts events of membrane fusion during release of vesicles as well as endocytotic events, rarely visible in isolated synaptosomes. Numerous omega shaped transmitter discharging vesicles at the AZ membrane as well as vesicle membrane fusing with plasma membrane in the vicinity of the AZ can be observed. A small synapse shown in Figure 41 B is likely in the development, because the AZ is rather small and shows signs of growth. Hence, numerous vesicles were caught fusing outside the AZ-area. Furthermore, membrane invaginations occur outside of the AZ, indicating that these synaptic vesicles were caught during the initial steps of endocytosis (C in Figure 41) rather than during late stages of vesicle collapse into the membrane.
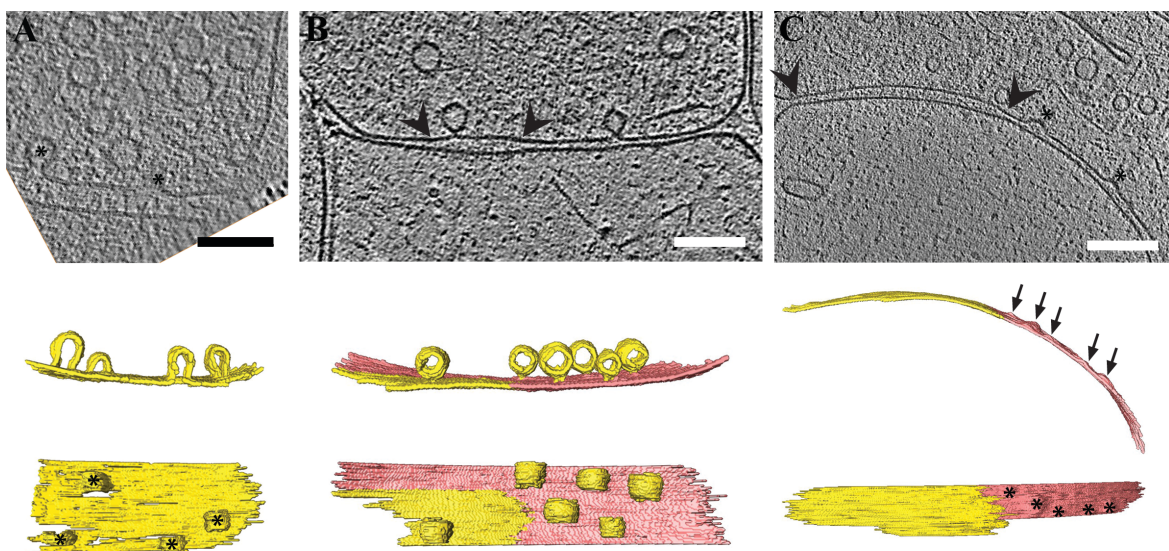


*Figure 41: Events of synaptic release and endocytosis in synapses of primary cultured neurons.*

*Column **A** shows synaptic vesicle release at the AZ-membrane in tomographic slice (release events indicated with asterisk) and segmented isosurface. Column **B** shows a fusing synaptic vesicle at the AZ-membrane (segmented in yellow, indicated by arrowheads) as well as fusion events in the vicinity of the synaptic cleft. Column **C** shows a wide AZ-area (segmented*

*in yellow, indicated by arrowheads) exclusive of transmitter release and several sites of presumable vesicle endocytosis (indicated by asterisk in the tomographic slice and the membrane view segmentation and by arrows in the side view segmentation). Scale bars: 100 nm*

In conclusion it is safe to say that tomography data of primary cultured neurons provides a fascinating insight into transport processes, synapse formation as well as SV recycling in immature and mature synapses. All of those processes are to be investigated further to identify main players of transport granules and vesicles and to visualize the essential steps in synaptic development. Especially the comparative analysis of maturating synapses and varicosities may be the basis to draw conclusions for synaptogenesis.

## 4.4 Phorbol ester treated synapses in primary cultured neurons

As we have learned from the analysis of release facilitated synaptosomes there is only a limited effect of phorbol ester treatment beyond the proximal zone to the AZ membrane. To expedite investigation of synapses from cultured neurons, we focused the manual segmentation on this very zone tracing only the presynaptic membrane with proximal SVs. Thus, analysis for the few available tomograms (see Table 6) was performed within a few days. Synapses, which appeared to be immature as well as synapses cut off lying on the edge of the field of view, have been excluded from the analysis.

*Table 6: Summary of the total number of tomograms acquired, from which a subset of data includes synapses (total) and another subset was suitable for analysis with its vesicles, tethers and connectors segmented and included in statistical analysis. Here, synapses not suitable for analysis were immature or not completely in the field of view of the data.*

|  | Control | PDBu |
|---|---|---|
| tomograms | 22 | 10 |
| synapses total/analyzed | 7/3 | 3/2 |
| vesicles | 47 | 38 |
| tethers | 18 | 23 |
| connectors | 71 | 33 |

As can be seen from Table 6 the dataset is insufficient to draw strong conclusions from results.

Synaptic tomograms were only segmented in the proximal zone to a maximum distance of 100 nm from the AZ. Thus, it is not possible to evaluate the physiological vesicle occupancy of SVs relative to the AZ distance for the whole segmentation region, as done before. Since synapses in culture reveal SV occupancy in the close to physiological state the curves to be seen in Figure 42 are noteworthy. While synaptosomes are vitrified in a buffer with ion concentrations set to prevent from stimulation, synapses in culture are active until sample vitrification. Thus, the typical SV occupancy profile in synaptosomes was seen only rarely in synapses. Instead, SVs in the proximal zone did not necessarily display a peak. PDBu-treated synapses on the other hand showed a large and extended peak with a dip around 100 nm. This made them different from synaptosomes, which show lower SV concentration in the intermediate zone of 45 nm – 75 nm. The mean minimal distance of proximal SVs was consistent with observations in synaptosomes, while PDBu-treated synapses showed a 40% reduced distance. This is a clear indication of the effect of PDBu-treatment on tethering of SVs.
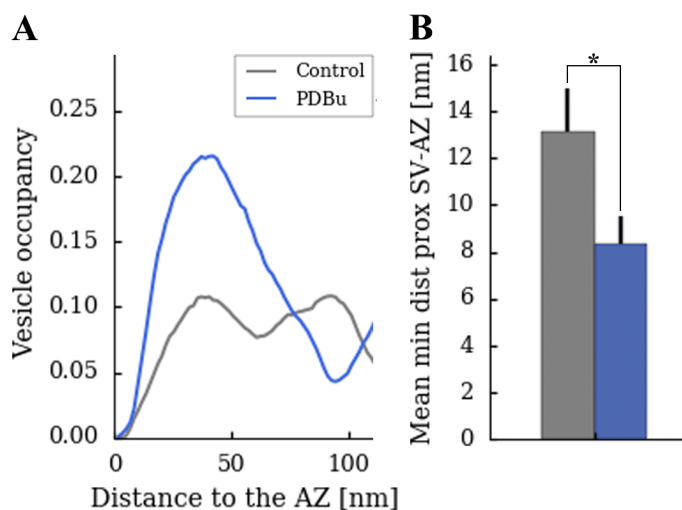


*Figure 42: Vesicle occupancy and mean minimal distance of SVs to the AZ in synapses.*

**A**: *A wide peak in SV occupancy of PDBu-treated synapses discriminates occupancy from synaptosomes as well as a shrunk peak for control synapses.* **B**: *The mean minimal distance of SV is 40% shorter than in control synapses (mean ± sem control = 13.11 ± 1.83 nm, mean ± sem PDBu = 8.34 ± 1.21 nm, p < 0.05, Student's t-test)*

Results

Since this analysis was focused on the proximal zone of the presynaptic volume from the beginning, results feature characteristics of this area. As it can be seen in Figure 43, the number of tethers dramatically increased as an effect of PDBu-treatment. Consequently, the fraction of tethered SVs was increased by around 17%. The number of proximal tethered SVs per unit AZ surface area (1 $\mu m^2$) increased three times a for PDBu-treated synapses. Finally, the fraction of proximal SVs in the RRP is augmented by around 8%.
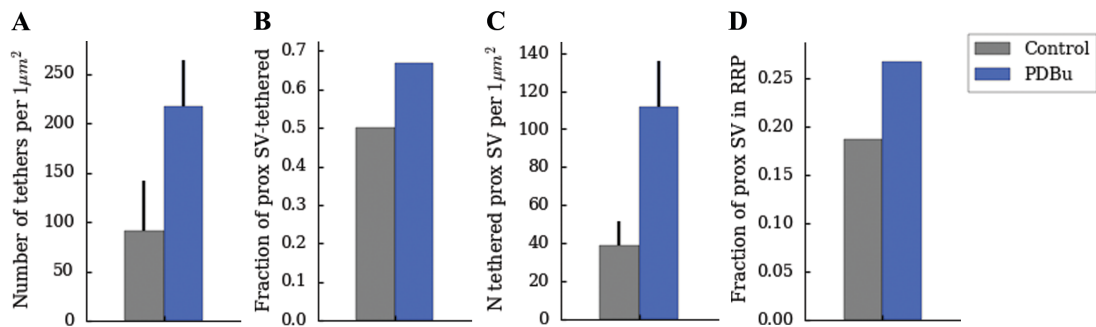


*Figure 43: Tethering in synapses.*

*A: The number of tethers per AZ surface in 1 $\mu m^2$ is more than doubled after PDBu-treatment (mean ± sem control = 91.68 ± 50.12, N = 3; mean ± sem PDBu = 216.73 ± 46.87, N = 2, p > 0.1, Student's t-test). B: The fraction of proximal SVs that are tethered is insignificantly increased (control: 0.500, N = 16, PDBu: 0.667, N = 15). C: The number of tethered SVs per AZ surface is 3-times higher in PDBu-treated synapses than in control synapses (mean ± sem control = 38.67 ± 12.52, N = 3; mean ± sem PDBu = 111.88 ± 24.01, N = 2). D: The fraction of SVs is insignificantly higher in PDBu-treated synapses than in controls (control: 0.188, N = 16, PDBu: 0.267, N = 15).*

In summary, it is indicated that synaptic plasticity provoked by the treatment with phorbol esters can equally be observed in primary cultured neurons in their close to physiological environment. To finally confirm this result, more data has to be acquired and segmented. Additionally, it might be worthwhile to analyze existing data beyond the proximal zone of the presynaptic compartment to expand the analysis by investigating connectivity and SV occupancy in a more elaborate way.

During the work on this thesis the ongoing effort to achieve a streamlined sample preparation and high-quality data acquisition of synaptic tomograms was never finalized in a satisfactory manner. While the software-based tool for removal of artifacts became crucial for multiple applications, redeposition still rendered reliable detection of synapses in TEM images almost impossible. Thus, in numerous sessions of data collection yield of synaptic tomograms remained limited. Despite the useful information extracted from non-synaptic neuronal processes, the main goal of this project could not entirely be accomplished. Thus,

it still remains a future goal to master the preparation of synaptic samples of primary cultured neurons with limited redeposition and low sample thickness.

# 5. Discussion

## 5.1 Structural features of facilitation of evoked release

During evoked release of glutamate at excitatory synapses, an action potential triggers fast and short opening of voltage-gated $Ca^{2+}$-channels. This results in a local rise of intraterminal $Ca^{2+}$ and causes $Ca^{2+}$ binding to sensors of the SV fusion machinery and terminating fusion abruptly when local $Ca^{2+}$-levels decrease. The v-SNARE synaptobrevin-2 and the t-SNARES syntaxin-1 and SNAP-25 may form a tight complex of $\alpha$-helical SNARE-motifs supported by complexin and synaptotagmin-1. While the helical bundle zippers up, energy is released probably essential for fusion of vesicular and presynaptic membrane (Sutton et al., 1998). This process occurs in less than a millisecond, provided that the SV is already in the primed state.

This study illustrates the ultrastructural features of synapses in the state of release facilitation that is manifested in increased rates of SV priming. PDBu-treated synaptosomes and synapses showed larger RRPs indicating the crucial role of Munc13 during SV priming. This state was formerly also described as superpriming of SVs, which is the result of either posttetanic potentiation or activation of the PLC-DAG-dependent pathway (Taschenberger et al., 2016). Also Lee et al defined SVs in a pool of fast releasing vesicles with high $Ca^{2+}$-sensitivity to be superprimed or being in a state of positional priming (Lee et al., 2013).

The calcium- and phospholipid-dependent protein kinase PKC is equally known to prime SVs for release via multiple intermediate steps (see 1.2.3) and was for a time suspected to be the only mediator of phorbol ester induced release facilitation (Stevens and Sullivan, 1998). Here is shown the structural phenotype of synapses in the state of phorbol ester-induced facilitation under a complete PKC inhibition. While control samples show mainly long SV tethers, neurotransmitter release facilitated synaptosomes showed a peak of tether length at 6 nm. This indicates that Munc13 is involved in the formation of short tethers, while Munc13 itself is not in that range of length. The MUN domain itself, which supports the SNARE-complex formation is 195 Å in length and is sufficient to rescue vesicle

exocytosis after Munc13 KO (Basu et al., 2005). Furthermore, no significant number of tethers in that range could be observed in release facilitated synaptosomes. This implies the Munc13 dependent priming step rapidly generates short tethers. Furthermore, the increase in Munc13-concentration also increases the number of vesicles comprising the structural RRP, defined as SVs tethered by more than two filaments. Another indicator for the fast binding of Munc13 to SVs (via other AZ proteins) is the only insignificant increase in number of protrusions at the AZ-membrane without binding SVs (Figure 25). A closer look at the multiple tethers of a SV in the RRP (Figure 28) displays longer complex segments exist in addition to short ones. Consequently, larger complexes which might be part of the priming machinery are still bound to SVs, while short tethers bring the fusing membranes into proximity. Thus, these longer filaments (probably including Munc13) lye rather flat on the presynaptic membrane to fit into the gap between SVs and presynaptic membrane. Because the MUN-domain is structurally strikingly similar to the family of CATCHR proteins, that work in various trafficking steps, Munc13 may also form elongated arrays of stacked $\alpha$-helical bundles with flexible hinge regions, that tether vesicles to the site of fusion (Li et al., 2011). Consequently, Munc13 may be flexible during the priming process with no elongated form stretching from membrane to the SV but rather assumes a folded conformation together with binding partners.

According to these results we can hypothesize the following, taking our knowledge of the priming machinery into account (see 1.2.2): DAG/phorbol ester-dependent translocation to the presynaptic membrane and Munc13 activation act downstream of RIM1$\alpha$-dependent disruption of the Munc13-homodimer (Camacho et al., 2017). Munc13 might be translocated together with RIM1$\alpha$ with Munc13 binding DAG/PDBu and RIM1$\alpha$ binding Ca$^{2+}$-channels via RIM-BP (Kaeser et al., 2011). Simultaneously, RIM1$\alpha$ binds the SV-associated Rab3, enabling tethering SVs to the membrane via this complex. After interaction of Munc13 with the inhibitory Munc18-Syntaxin-1-complex, the SNARE domain of Syntaxin-1 is exposed to interact with SNAP-25 and the v-SNARE Synaptobrevin. During this process the priming complex is presumably lying flat on the presynaptic membrane to enable the formation of short tethering filaments. This scheme of vesicle fusion is based on the assumption that long tethers represent the SV priming complex (Munc13-RIM1$\alpha$-Rab3), while short tethers represent the membrane fusion complex (SNARE). Complexin clamps the SNARE-complex, inhibiting zippering up and membrane

fusion. Only upon $Ca^{2+}$-binding of Synaptotagmin-1, which may be enabled by the interaction of Synaptotagmin-1 with the Munc13-RIM1$\alpha$-Rab3-complex, the complexin clamp is released and zippering of SNAREs leads to fusion (Giraudo et al., 2006). $Ca^{2+}$-dependent phospholipid-binding Synaptotagmin-1 might induce membrane curvature and reduce the energy barrier for membrane fusion (Hui et al., 2009). Because the samples analyzed in this thesis were deprived of $Ca^{2+}$ to allow the visualization of SV priming during release facilitation without depletion of the proximal synaptic zone from spontaneous release, SNARE complexes might have been arrested in the state of incomplete zippering of the $\alpha$-helical bundles.

Fusion processes with having hemi-fusion as a stable intermediate step (Jahn and Südhof, 1999) were never observed in the data acquired here. It is also worthy to mention that SVs were never observed having an extended contact with plasma membrane. Such a state, termed docking, presumably occurs prior to fusion, and is often mentioned in literature (Jahn and Fasshauer, 2012). It is usually observed in conventional EM, thus its formation might be due to dehydration artifacts.

## 5.2 Structural features of spontaneous release facilitation

Spontaneous and evoked neurotransmitter release are the two main modes of signal transduction and it is known so far that the overexpression of Munc13 facilitates both of those release modes (Betz et al., 1998). In evoked synaptic transmission cytosolic $Ca^{2+}$ is increased upon arrival of an action potential and vesicles primed for release, fuse with the presynaptic membrane in milliseconds (Südhof, 2004). Such activity-evoked vesicle fusion supports most of neurotransmitter release and is an essential component of synaptic information transmission. Spontaneous transmitter release on the other hand plays and important role in the maintenance of the structure and function of the synapse (Sutton et al., 2006). It occurs at a very low rate of one or two vesicles per minute and in absence of activity (Geppert et al., 1994). In contrast to the highly orchestrated evoked neurotransmitter release, spontaneous vesicle fusion is only loosely regulated by extracellular $Ca^{2+}$ or intracellular $Ca^{2+}$-fluctuations (Angleson and Betz, 2000). To this day it is still under discussion which

synaptic vesicles are determined for spontaneous release and if there is any difference in vesicle pools for the two modes of release. Experiments with fluorescent styryl dyes came to different outcomes (Sara et al., 2005; Wilhelm et al., 2010). Interestingly, spontaneous fusion rate is not altered by KO of proteins critical for evoked SV fusion like synaptotagmin-1, complexin and RIM1$\alpha$ (Calakos et al., 2004; Geppert et al., 1994; Reim et al., 2001). Spontaneous release is significantly reduced after genetic deletion of synaptobrevin, Munc18 and Munc13 (Schoch et al., 2001; Verhage et al., 2000). Munc13 isoforms are essential for spontaneous as well as evoked transmitter release and in KO mutants synapse formation is undisturbed but signal transmission is completely muted (Varoqueaux et al., 2002). Since the two important players in SV priming are essential for spontaneous release, it is probable that spontaneous fusion is the result of occasional firing of SNAREs due to Brownian fluctuations of the vesicle. This can be increased by strong water efflux from the synapse induced by high osmolarity in sucrose solution (Jahn and Fasshauer, 2012). Furthermore it was proposed that spontaneous release simply reflects an imperfect suppression of evoked vesicle fusion and that it does not have a function (Kaeser and Regehr, 2014). Other studies showed different properties for SVs undergoing spontaneous release and show an altered dynamic behavior than not releasing SVs, particularly in the ability to engage in directed motion (Peng et al., 2012). Thus, there is no complete consent on the features of SVs destined for spontaneous release. However, there are indicators that spontaneous release is not at all without any function but crucial for synaptic activity. It may regulate synaptic strength by influencing protein synthesis and act as a trophic factor to prevent the loss of dendritic spines by activating AMPA ($\alpha$-amino-3-hydroxy-5- methyl-4-isoxazolepropionic acid) receptors (McKinney et al., 1999). It also restricts the diffusion of AMPA receptors at active synapses, thereby regulating the number and type of AMPA receptors present at a synapse (Ehlers et al., 2007).

It was reported that both modes of release share the same SV pool and the SVs therein cannot be discriminated easily (Wilhelm et al., 2010). If SVs to be spontaneously released are tethered to the presynaptic membrane just as SV fusing upon AP-signaling, they might be by an alternative set of fusion proteins like non-canonical SNARES. This might indicate that the two forms of release are spatially segregated (Atasoy et al., 2008; Ramirez and Kavalali, 2011). In any way, the fundamental roles of spontaneous release indicate that it might be regulated somehow. It has been shown before and also in this thesis (see 4.1.2) that

spontaneous neurotransmitter discharge can be facilitated by phorbol ester as can be evoked glutamate release. Thus, structural features of SVs or SV-pools destined to fuse spontaneously might be different. While short and multiple tethers should also increase the probability of spontaneous release, the presence of longer connectors for PDBu- and Ro31-treated synaptosomes in the proximal and intermediate zone might indicate a facilitation of spontaneous release regardless of the tethering state. Especially the fact that this is the case for tethered as well as untethered SVs (see Supplementary figure 1) might show the availability of SVs for spontaneous release independent of tethering/priming for release. It was hypothesized before that SVs might be tagged for one way of neurotransmitter release during endocytosis (Chung et al., 2010) indicating that SVs destined for spontaneous release, if at all, obtain features independent of tethering and the release machinery. A possible feature might be the lack of a specific species of connectors, for example Synapsin. It organizes the reserve pool of SVs (Gitler et al., 2008), which might be a source of spontaneously released SVs (Ramirez and Kavalali, 2011). In general, it can be assumed that an extension in length of interconnecting filaments augments the overall motility of SVs within a presynaptic terminal and thus increases the probability of SVs randomly fusing during spontaneous release. Interestingly, PKC-inhibited Ro31-treated synaptosomes show multiple of these long connectors, indicating that the same species of protein interacts with PKC. These connectors may be a target of PKC-phosphorylation and thus be cleaved of SVs in PDBu-treaded synaptosomes with active PKC. Furthermore, multiple long connectors as do exist in Ro31-treated synaptosomes don't interfere with release facilitation on the basis of PDBu. Unfortunately, the identity of these connectors cannot be determined by this study.

## 5.3   The role of PKC in release facilitation

Before discussing the effect of the two PKC-inhibitors on the synaptosomal phenotype, the presumable way of action of both should be clarified. Staurosporines like Ro31 are ATP competitive PKC- inhibitors (Tamaoki et al., 1986) and thus PKC is completely inactive during Ro31-treatment. CalC is supposed to equally inactivate PKC in its entirety, since it is binding at the $C_1$-domain of PKC and thus displacing PDBu followed by the destruction of the kinase after photoactivation of CalC and free radical production

(Gopalakrishna et al., 1992; Sossin, 2007). While the release facilitating effect of PDBu could be abolished by CalC-treatment and the phenotype in many aspects is similar to control synaptosomes, we can confirm the inhibition of PDBu-activation by CalC. On the other hand, we have to assume that the photoactivation did not occur under the conditions of this experiment. The incubation of synaptosomes with CalC was conducted in a laboratory equipped for photosensitive experiments and thus was illuminated to a minimum (desk lamps at the vitrification bench). Consequently, it can be assumed that the $C_1$-binding domain of PKC and Munc13 is blocked by CalC. This means the PDBu-induced release facilitation is abolished, while a PKC-activity should still be existent at a base line level. Thus, we can conclude that PDBu-treated samples show increased PKC-activity, CalC-treated samples show a low PKC activity and Ro31- treated samples should be depleted of active PKC.

Considering these assumptions, we should observe the connectivity of vesicles especially in proximity to the active zone. Connector lengths were increased in PDBu- and Ro31-treaded samples. Since both of these samples have the PDBu-dependent release facilitation in common but Ro31-samples lack PKC activity, we can conjecture that the extended connectors do occur independently of PKC activity. Since both samples are in the state of release facilitation, it is legitimate to speculate that during the course of enhanced SV priming for release connectors are indirectly affected as well. The activation of Munc13 with the consequent assembly of the SV priming and fusion complexes might activate other kinases like PKA, which in turn modifies SV connectivity. PKA is known to phosphorylate Synapsin, a protein known to control SV pools in glutamatergic synapses (Gitler et al., 2008; Jovanovic et al., 2001; Lee, 2006; Millán et al., 2003). Phosphorylation of Synapsin might be a regulatory switch in synaptic activity that causes dissociation of phosphorylated Synapsin from the SV-membranes (Sihra et al., 1989). While Synapsin is known to regulate the reserve SV pool (Gitler et al., 2008) it cannot be localized bound to SVs in the RRP (Siksou et al., 2007). Connectors in the proximal zone are likely composed of other proteins, amongst those possibly synaptobrevin, as hypothesized before (Fernández-Busnadiego and Lučić, 2012).

Although it is not possible to define the identity of interconnecting filaments in this study the decrease and increase in numbers depending on pharmacological treatment was

Discussion

quantified. Connectivity was increased for both PKC-inhibiting treatments, meaning the fraction of connected SVs is increased as well as the number of connectors per SV. Compared to the low connectivity of PDBu-treaded samples (increased PKC activity) in untethered SVs, the high connectivity in PKC-inhibited synaptosomes is striking together with a strong increase of connectivity for Ro31-treated samples at tethered SVs (see Figure 33, p. 76). It can be assumed that the reduced (CalC) or the absent (Ro31) activity of PKC is responsible for flawed connector dissociation from SVs during SV priming. Upon stimulation a large fraction of connectors is removed from SVs in a phosphorylation-dependent manner, thus increasing SV motility (Fernández-Busnadiego and Lučić, 2012). Consequently, it is not surprising that we observed a lack of connector dissociation from SVs in PKC-inhibited synaptosomes. Interestingly, the increased connectivity in Ro31-treated synaptosomes does not affect the release facilitation of these synapses, indicating that a dissociation of at least some type of connector is not critical for spontaneous SV release.

The most striking and unexpected phenotype observed in synaptosomes treated with PKC-inhibitors was the effect on tether length. While it was expected that CalC-treated synaptosomes are endowed with longer tethers similar to controls and Ro31-treated synaptosomes with short tethers as observed in PDBu-treated samples, the result showed the opposite (see Figure 32, p. 74). To understand this unexpected result, a closer look at the PKC-substrates in the synapse is necessary. Among the candidates to be involved in tether formation there is Munc18 as well as SNAP-25 and Synaptotagmin-1, with the former being an inhibitor of SNARE complex-formation and the latter being a component of the SNARE-complex. PKC-catalyzed phosphorylation inhibits the interaction of Munc18 with Syntaxin-1 and thus Syntaxin-1 is free to bind Synaptobrevin and SNAP-25 to assemble the SNARE complex (de Jong et al., 2016). In PKC-inhibited synaptosomes Munc18 remains in its non-phosphorylated form interacting with Syntaxin-1 and blocking SNARE-complex formation.

Additional to Munc18, SNAP-25 and Synaptotagmin-1 are targets of PKC (de Jong et al., 2016; Nagy et al., 2002). While SNAP-25 binds Synaptobrevin and Syntaxin-1 to assemble the SNARE-complex, Synaptotagmin-1 is the SV-associated $Ca^{2+}$-sensor, and thus critical for $Ca^{2+}$-dependent fusion (Silinsky and Searl, 2003). In Ro31-treated synaptosomes the lack of PKC activity and consequently the deficient phosphorylation of those targets may

account for the low number of short tethers, while those short tethers exist in CalC-treated synaptosomes. Interesting about these results is the fact that spontaneous release is independent of SNAP-25 phosphorylation (Hepp et al., 2002; Houeland et al., 2007), while it is essential for evoked vesicle fusion. This may serve as an explanation for the increased spontaneous release from Ro31-synaptosomes despite the lack of augmented short tethers. Despite significant differences in numbers of short and long tethers in the three pharmacological treatments employed, a clear conclusion as to whether one of the types of tethers is responsible for one mode of release cannot be made. It seems that short tethers in the range of numbers as seen after PDBu-treatment are not crucial for facilitated spontaneous release, because Ro31-treated samples equally show release facilitation, but no increase in short tethers. On the other hand, we cannot conclude that long tethers are sufficient for release facilitation, because all groups of treatments showed amounts of short tethers, which might be sufficient for release facilitation.

So far it was under discussion if the activation of PKC by PDBu is necessary for release facilitation. While Lou et al as well as Silinsky and Searl (Lou et al., 2008; Silinsky and Searl, 2003) showed it was necessary but not sufficient, Rhee et al (Rhee et al., 2002) claimed that PDBu-dependent release facilitation relies exclusively on Munc13 translocation. Palfreyman and Jorgensen (Palfreyman and Jorgensen, 2007) even propose that the phosphorylation of Munc18 is a prerequisite for DAG/PDBu-dependent translocation of Munc13. We can shed new light on this discussion. In summary, we saw an effect of PKC-activity on the ultrastructural synaptic phenotype (eg. in tether lengths), which did not influence release facilitation in PDBu- and Ro31-synaptosomes or the absence of facilitation in CalC-synaptosomes. Ro31-samples were release facilitated without an increase in short tethers. CalC-samples did not show release facilitation even though short tethers existed. We propose that the acceleration of vesicle recruitment seen after SNAP-25- and Munc18-phosphorylation in the presence of phorbol ester is masked by the massive Munc13-recruitment to the AZ-membrane (Nagy et al., 2002). PDBu-dependent activation of Munc13 as well as PKC results in release facilitation with ultrastructurally visible multiple short tethers, while PDBu-dependent release facilitation with inhibition of PKC results in release facilitation despite a lack of increase in short tethers and the existence of multiple long tethers. Thus, we can conclude that multiple tethers are essential for augmented SV fusion while short tethers in numbers as seen in control samples are sufficient

Discussion

for release facilitation together with an increase in connecter length in proximity to the AZ. Additionally, we can assume that PDBu- and Ro31-treated samples show two different states of release facilitation. Without active PKC SVs are mainly primed with long tethers, thus it is probably the priming complex (Munc13-Rim1α-Rab3) that is tethering SV. With activated PKC the SVs move from this primed state to the shortly tethered state, presumably by SNARE-complex formation, supported by PKC and Munc13. Thus, the results gained by CET-analysis revealed nuances in the effect of pharmacological treatment so far undisclosed in physiological experiments (summed up in Figure 44).

+ **Long Tethers**
- **Short Connectors**

+ **Short Tethers**
- **Long Connectors**

Munc13

PKC/Munc13

Rim  Rab3

Munc13

DAG

SNARE

Ca²⁺-channel

Hypothesis

+ **Munc13-Rim1α-Rab3-complex formation**

+ **Phosphorylation of Munc18, SNAP-25 and Syt-1**
+ **Syntaxin release from Munc18**
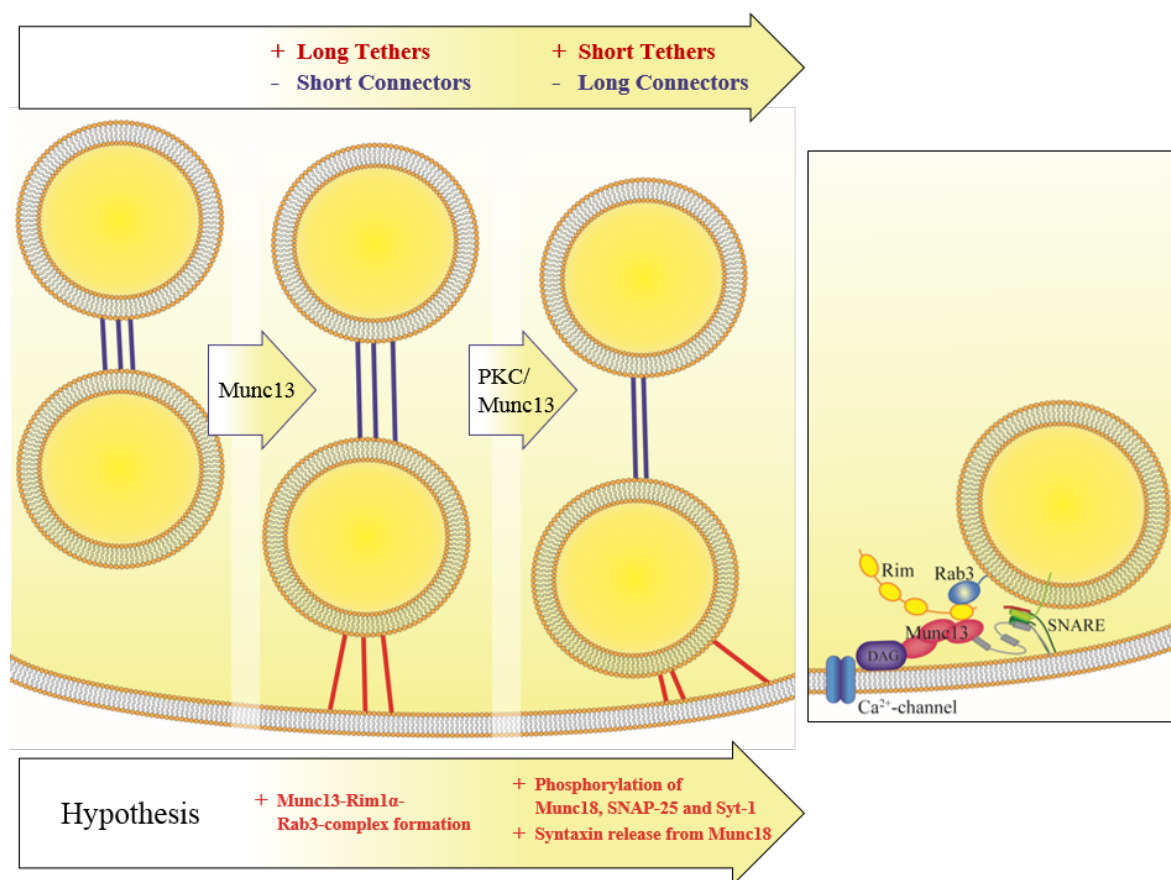
*Figure 44: The role of Munc13 and PKC in synaptic vesicle priming:*

*The accumulation of long tethers and the reduction of short connectors relies on Munc13 activation. For the formation of multiple short tethers and the decline in connectivity, PKC is additionally necessary. The lower arrow sums up the hypothesis described in this chapter: Munc13-translocation triggers the formation of the Munc13-Rim1α-Rab3-complex visible as long tethers in the data presented here. Short connectors holding SVs in the reserve pool are cleaved off, which may be Synapsin. Catalyzed by Munc13, Syntaxin is set free from Munc18; PKC phosphorylates the substrates Munc18, SNAP-25 and Synaptotagmin-1 (Syt-1) enabling SNARE-complex formation. Long connectors are removed in proximity to the AZ, which may be Synaptobrevin. The right-hand side scheme shows the Munc13-Rim1α-Rab3-complex probably represented by long tethers and the SNARE-complex, probably represented by short tethers here.*

## 5.4 Disruption of synaptic cell-cell adhesion molecules by PDBu-dependent PKC-activation

For the quantification of synaptic features in a statistical analysis, numbers were put into reference to the surface area of the AZ-membrane. PDBu-treated synaptosomes were endowed with significantly smaller AZ-surfaces (see Figure 24, p. 63) and synaptic clefts compared to control samples. The decrease of AZ-membrane surface area was striking and comparison to the surface sizes of PKC-inhibitor treated samples revealed correlation with the level of PKC-activity in each synaptosomal treatment. Consequently, treatment of synaptosomes with PDBu is aspersed to affect cell adhesion in the synaptic cleft. Although phorbol esters are quite conventional amongst pharmacological treatments of synaptosomes, this relationship was so far not reported. However, phorbol esters have a similar effect on cell adhesion in cancerous tissue and the presumable target proteins were reported in studies (Fabre and García de Herreros, 1993; Xia et al., 2003). These studies showed an influence of PKC-activation by phorbol esters on the cell adhesion maintained by Cadherin and Catenin. Classical cadherins undertake critical roles in cell-cell adhesion in vertebrates and mediate the majority of tissue-specific interactions and thus have direct effects on development and cancer (Batlle and Wilkinson, 2012; Seong et al., 2015). At synaptic junctions cadherins form trans-dimers and bridge the intercellular space with their ectodomains, while their cytoplasmic domains bind Catenins and are thus linked to intracellular signaling pathways and the cytoskeleton. It was found that p120-catenins are critical for excitatory synapses and spines since the genetic depletion of p120-catenins led to a reduction of both developing and mature synapses. Studies suggest that p120-catenin family proteins regulate dendritic arborization and mediate Cadherin stability (Seong et al., 2015). In murine fibroblasts and human carcinoma cells the influence of PDBu on cell adhesion was tested. PDBu resulted in rapid changes in cell adhesion by changing phosphorylation levels of serine and threonine in p120-catenins (Xia et al., 2003). The application of the phorbol ester TPA on colon cancer cells, colonies scattered with diminished cell-cell contacts. The effect of TPA was the increase in PKC activity provoked by the phorbol ester and correlated with the loss of Cadherin in the samples (Fabre and García de Herreros, 1993). Both findings from research on cancerous cells are consistent

with the effects of PDBu on the cell-cell adhesion at the synaptic cleft of synaptosomes and may explain the mean reduction of the AZ surface area by almost 40%. Moreover, the surface areas of the presynaptic membranes in PKC-inhibitor treated samples may provide a reference for the PKC-activity in those samples: the smaller the AZ-surface the higher the activity of PKC (see Supplementary figure 3, p. 114). According to this assumption the residual activity after CalC-treatment can be confirmed.

## 5.5   Maturation of synapses in cultured neurons

Thanks to CET we could visualize and quantitively analyze the ultrastructure of vitrified, close-to-native state neuronal processes in their specialized compartments of axonal boutons, developing synapses and mature synapses of dissociated hippocampal neurons. These cultures were grown for an extended time to allow synaptogenesis, and then vitrified and thinned with the focused ion beam. Thus, these diverse steps in neuronal development could be analyzed.

The data presented here show that clusters of vesicles in axonal boutons are interconnected by pleiomorphic filaments, which play a major role in axonal transport processes (Schrod et al., 2017). Additional to synaptic vesicles, dense-core granules of uniform size exist in axonal boutons and are equally interconnected and tethered to smooth endoplasmatic reticulum and microtubules (Figure 37, p. 85). Large dense-core vesicles like Piccolo-Bassoon transport vesicles (PTVs) and synaptic vesicle protein transport vesicle (STVs), which are transported in connection with each other (Bury and Sabo, 2011; Tao-Cheng, 2007). On the contrary, the granules shown here are arranged in clusters distant from synaptic vesicles at non-synaptic axonal boutons. This might indicate that theses granules are not part of synaptic machinery delivery organelles like PTVs and STVs but may have another role or are selected for degradation.

The non-synaptic bouton shown Figure 37 (p. 85) is endowed with a cluster of synaptic vesicles located in the tumefaction of the axon but not yet accumulating proximal to the plasma membrane. Boutons like these might represent the state of non-synaptic swellings during synaptogenesis that contain clusters of synaptic vesicles, but not the release

machinery needed to tether vesicles to the presynaptic membrane. Furthermore, these vesicles are located at some distance from the microtubules and are thus probably not in the process of transport but are paused at this axonal swelling.

Synaptic connections that were thin enough to be imaged by CET without an additional thinning step often turned out to be immature. These synapses were endowed with the characteristic synaptic cleft, which usually presents itself in universal shape of a surface of around 0.1 µm$^2$ and a width of 25 nm (Lučić et al., 2005b) and decorated with trans-cleft densities. The postsynaptic structure on the other hand was not as dense as was commonly observed for isolated cortical synaptic terminals and appeared less elaborate but rather as a thin leaflet proximal to the postsynaptic membrane. This feature of a thin leaflet-shaped PSD was also found for inhibitory synapses in CET confirmed by transmitter receptor staining with correlative microscopy (Tao et al., 2018). Nevertheless, these synapses are defined here as immature, since they were of overall reduced size compared to the data shown in the afore mentioned publication. In the presynaptic component, the cytosolic volume was sparsely populated with synaptic vesicles, while the interconnecting filaments and tethering structures of the synaptic release machinery were weak. The quantification of the presynaptic protein network shows two interesting facts (Figure 40, p. 88). Tethering of SVs is overall reduced in immature synapses but the proteins, which tether SVs are presumably the same, since they have the same mean length. Connectivity is equally reduced in immature synapses, but connectors also show a strong difference in length, indicating that different proteins form the pool of connectors. Opposed to these features of immaturity, plenty of events of vesicle fusion, such as omega shapes, are captured in tomography data as well as almost fully collapsed endocytosed vesicles at membrane stretches alongside the synaptic cleft (Figure 41, p. 89). Especially since the incidence of vesicle fusion is very rare in synaptosomes (~1 event/10 synaptosome tomograms) the indication of multiple events of exo- and endocytosis is surprising.

Tomography data of mature synapses showed exceptionally high density in the postsynaptic as well as the presynaptic terminals (Figure 39, p. 87). Since mature synapses often exceed the thickness which can be tolerated in CET, thus necessitating thinning with FIB, which proved to be a significant bottleneck. During FIB-milling of neuronal samples milled biomaterial and gallium redeposited on the milled surface and was thus hiding

discernible features of the milled area in TEM. After development of tomogram cleaning algorithms data acquired of synapses from culture could be analyzed without disturbing densities of redeposited material on the specimen. Mature synapses are characterized by elaborate protein complexes, that stretch throughout the cytosol of the postsynaptic density with the borders of its organization barely to make out. The presynapse was completely filled with synaptic vesicles compared to synaptosomes. The number of proximal vesicles tethered to the presynaptic membrane was similar to observations made for synaptosomes. This is another confirmation of the suitability of synaptosomes for statistical analysis of synaptic structure.

Finally, native synapses in primary culture were brought to the state of release facilitation by the application of phorbol ester to the living cells immediately before vitrification. Despite the lack of significant results due to the low number of PDBu-treated tomograms the trend towards a strong effect of release facilitation is visible (Figure 43, p. 92). Overall tethering (number of tethered SVs) as well as the number of vesicles in the readily releasable pool was strongly increased compared to naïve synapses.

In conclusion, the analysis of tomography data of primary cultured neurons from hippocampal cells allowed us to get an insight into the major functional entities. Non-synaptic axonal boutons could be visualized as well as immature synapses and large synapses in their mature state. Imaging neurons in cell culture by CET remains a challenging target because sample preparation from cells in the state of synaptogenesis is not at all trivial. While neuronal processes are often thin enough for CET imaging, data of large synapses is sparse because they exceed the feasible thickness. Still no progress has been made to prepare FIB-thinned neuronal samples without redeposition of dense material. Nevertheless, the collection of a large dataset of synapses is of high interest with regard to the future investigation of synaptic development and maturation. This was recently achieved for the analysis of different types of synapses from cultured neurons (Tao et al., 2018), which gives hope and motivation to continue the endeavor of high-throughput investigation of synapses in native neuronal cells.

# 6. Conclusion

The analysis of vitrified neuronal samples from isolated synaptic terminals of the rodent cortical tissue and primary culture from dissociated hippocampal cells provided complementary results. Isolated synaptosomes provide relatively fast sample preparation and comparably high-throughput data acquisition and allow significant statistical analysis of synaptic structures despite their limited viability. For neurons from cell culture the viability and synaptogenesis were shown, thus serving as an excellent system to investigate viable and active neuronal cells in their close-to-native state. However, high quality data collection from primary cultured neurons is not at all trivial and it is hindered by multiple bottlenecks during the process. Thus, this thesis combines quantification of structural features in synaptosomes with a more qualitative view on synaptic data.

Phorbol esters have been used extensively in experiments testing synaptic plasticity with the help of physiological and biochemical analysis, as has been done in this thesis, and also in numerous studies with the help of electrophysiology. This thesis now complements the previous findings with insights into the ultrastructural features of synaptosomes and synapses in a fully-hydrated, vitrified state. The segmentation method based on the hierarchical connectivity algorithm for the automated detection of tethers and connectors between synaptic vesicles and the active zone membrane proved to be suitable to investigate synaptic plasticity in structural detail. PDBu-dependent release facilitation revealed to be fully dependent on Munc13-translocation to the sites of vesicle fusion triggering synaptic vesicle priming for release and increasing the pool of readily releasable vesicles. The effect of PDBu was independent of the application of PKC-inhibitors in physiological experiments, but PKC-inhibition caused subtle ultrastructural differences in synaptosomes, which were not reported before. The number of short tethers increased PDBu-treated synaptosomes, but their length was reverted to the control level by PKC-inhibition. We can speculate that these short tethers are missing because the substrates of PKC, Munc18 and SNAP-25, which are critical for vesicle fusion, are not phosphorylated in PKC-inhibited samples. We could also show here that the PKC-dependent activation of its substrates in the synapse are not essential for release facilitation measured in physiological experiments. Additionally, tomograms of

Conclusion

PDBu-treated synaptosomes revealed a reduced AZ surface area, presumably due to changes in phosphorylation levels of Catenins after PKC-activation, which affects the cell-cell adhesion function of Catenin-Cadherin-complexes.

To further investigate the influence of phorbol ester on synaptic plasticity, subtomogram averaging may be beneficial. The identification of protein complexes present in the synaptic cleft and at the postsynaptic membrane, the trans-cleft colocalization of vesicle fusion sites and postsynaptic neurotransmitter reception sites can be identified. These nanocolumns were shown before and it may be highly interesting to explore if the sites of signal transmission align during vesicle priming for release, that is even before membrane fusion.

In the second part of this thesis, tomography data of different entities of primary cultured neurons was presented. In non-synaptic axonal boutons dense-core granules of uniform size were observed. Having contact filaments to microtubules these granules are possibly involved in transport along the axon. Nevertheless, they are likely independent from synaptic vesicles, because they did not cluster with those granules. Non-synaptic axonal boutons might represent a precursor state of synaptic assembly, where synaptic vesicles accumulate at a bulge of the bouton. The subsequent phase of synaptic development, immature synapses, are also shown in this thesis. They are sparsely endowed with electron dense complexes at the pre- and postsynaptic terminals and have a reduced number of synaptic vesicles. These findings are complemented by tomography data of mature synapses, revealing a higher density of synaptic vesicles and vesicle attached protein complexes compared to immature synapses. Compared to synapses in their native state, phorbol ester treated synapses presented strong features of release facilitation, similar to the results in synaptosomes. Thus, this thesis nicely illustrates different stages of synaptogenesis and plasticity, from the synaptic precursor, via the immature and mature synapses to the synaptic terminal in the state of release facilitation.

# 7. Appendix

*Supplementary table 1: FIB-milling strategies to overcome redeposition. Rough milling settings for wedges: 0.3 nA, CCS-settings: 700 ns, Overlap 65%, z-size ~ 6 μm*

| Milling order | Milling angle (deg) | Fine milling | Pollish | CCS | Contamination |
|---|---|---|---|---|---|
| 1 | 8 | 0.1 nA | No | No | Few c. but strongly irregular thickness and milling |
| 2 | 7 | 0.1 nA | No | 0.1 nA | Good: Fine c., smaller than 10 nm, regular thickness |
| 3 | 8 | 0.1 nA | No | 0.1 nA | Usual c. |
| 4 | 10 | 0.3 nA | No | 0.3 nA | Strong c. |
| 1 | 9 | 0.1 nA | 50 pA | No | Usual c., regular surface |
| 2 | 13 | 0.1 nA | No | No | Good: Fine c., smaller than 10 nm, regular thickness |
| 3 | 9 | 0.1 nA | No | 0.1 nA | Few-normal c. |
| 4 | 7 | 0.1 nA | No | 0.1 nA | Strong c., narrow wedge |
| 5 | 8 | 0.1 nA | 50 pA | No | Partly strong c. |
| 1 | 10 | 0.1 nA | No | 0.1 nA | Too thick, normal c. |
| 2 | 9 | 0.1 nA | No | 0.1 nA | Few-normal c. |
| 4 | 11 | 0.1 nA | No | 0.1 nA | Strong c. |
| 5 | 11 | 0.1 nA | No | 0.1 nA | Few-normal c. |

# Appendix

| Milling order | Milling angle (deg) | Fine milling | Dwell time | pollish | |
|---|---|---|---|---|---|
| **1** | 11 | 0.1 nA | 1 $\mu$sec | 50 pA | Transparent layer of c. and few particular c. |
| **2** | 10.5 | 0.1 nA | 1.5 $\mu$sec | 50 pA | Transparent layer of c. and few-normal particular c. |
| **3** | 10 | 0.1 nA | 2.5 $\mu$sec | 50 pA | Few-normal c. |
| **4** | 10 | 0.1 nA | 2 $\mu$sec | 50 pA | Normal-strong c. |
| **Milling order** | **Milling angle (deg)** | **Fine milling** | **CCS** | **Wedge width** | |
| **1** | 10 | 0.1 nA | 0.1 nA | 35 $\mu$m | Very strong c. |
| **2** | 8 | 0.1 nA | 0.1 nA | 35 $\mu$m | Very strong c. |
| **3** | 10 | 0.1 nA | 0.1 nA | 15 $\mu$m | Very strong c. |
| **4** | 8 | 0.1 nA | 0.1 nA | 15 $\mu$m | Good, partly normal or few c. |
| **5** | 10 | 0.1 nA | No | 35 $\mu$m | Good, partly normal or few c. |
| | | | | | |

*Supplementary table 2: Synaptosome tomography data analyzed for the statistical evaluation of this thesis*

| Control | dimensions | Microscope, detector | vesicle ids | extra ids | connectors threshold | pixel size (unbinned) | identifier |
|---|---|---|---|---|---|---|---|
| Con-7_tomo1-P2-DDD | 925, 925, 311 | Polara2, K2 | 9-167 | no | 1000, 2000, 50 | 4.27 | Con_5 |
| Con-7_tomo2-P2-DDD | 925, 925, 331 | Polara2, K2 | 9,247 | no | 400, 1900, 75 | 4.27 | Con_6 |
| Con-7_tomo3-P2-DDD | 925, 925, 291 | Polara2, K2 | 9,256 | no | 700, 1550, 50 | 4.27 | Con_8 |
| Con-7_tomo4-P2-DDD | 925, 925, 311 | Polara2, K2 | 9,163 | no | -100, 1100, 50 | 4.27 | Con_7 |
| Con-9-1_tomo1-P2-DDD | 925, 925, 271 | Polara2, K2 | 9, 232 | 8: vacuole | 1200, 3850, 150 | 4.27 | Con_9 |
| Con-9-1_tomo2-P2-DDD | 925, 925, 331 | Polara2, K2 | 9,256 | no | -325, 275, 25 | 4.27 | Con_10 |
| Con-9_tomo1 | 925,925,241 | Polara2, K2 | 9,256 | no | 940, 1300, 20 | 4.27 | Con_11 |
| Con-9_tomo2 | 925,925,241 | Polara2, K2 | 9,255 | no | 2720, 3160, 20 | 4.27 | Con_12 |
| Con-9_tomo4 | 925,925,301 | Polara2, K2 | 9,155 | 4, 5 | -750, 250, 50 | 4.27 | Con_13 |
| PDBu-con1-2_tomo1 | 512, 512, 181 | P1, CCD | 9,164 | no | -0.06, -0.29, 0.01 | 6.61 | Con_1 |
| PDBu-Con5-4_tomo1 | 512, 512, 161 | P1, CCD | 9,255 + 265,383 | no | -0.24, 0.08, 0.02 | 6.61 | Con_2 |
| PDBu-Con5-4_tomo2 | 512, 512, 181 | P1, CCD | 9, 193 | no | -0.28, -0.02, 0.02 | 6.61 | Con_3 |
| PDBu-Con5-4_tomo3 | 512, 512, 211 | P1, CCD | 9, 177 | no | -0.25, -0.01, 0.01 | 6.61 | Con_4 |
| Con11_tomo1_T2_K2 | 925, 925, 320 | T2, K2 | 8,211 | no | 3100, 3575, 25 | 3,42 | Con_14 |
| Con11_tomo2_T2_K2 | 925, 925, 320 | T2, K2 | 9,88 | no | -600, 0, 25 | 3,42 | Con_15 |
| Con11_tomo5_T2_K2 | 925, 925, 340 | T2, K2 | 9,255 + 265,336 | no | 2750, 3950, 50 | 3,42 | Con_16 |
| Con11_tomo7_T2_K2 | 925, 925, 270 | T2, K2 | 9,194 | no | 2800, 3300, 15 | 3,42 | Con_17 |
| PDBu | | | | | | | |
| PDBu-7-3-2_tomo2-P2-DDD | 925, 925, 321 | Polara2, K2 | 9,228 | no | 1550, 2250, 25 | 4.27 | PDBu_13 |

# Appendix

| | | | | | | | |
|---|---|---|---|---|---|---|---|
| **PDBu-7-3-4_tomo2-P2-DDD** | 925, 925, 251 | Polara2, K2 | 9,222 | no | 1225, 1650, 25 | 4.27 | PDBu_5 |
| **PDBu-7-3-4_tomo3-P2-DDD_1** | 925, 925, 331 | Polara2, K2 | 9,135 | no | -75, 375, 25 | 4.27 | PDBu_6 |
| **PDBu-7-3-4_tomo3-P2-DDD_2** | 925, 925, 331 | Polara2, K2 | 9,158 | no | -150, 475, 25 | 4.27 | PDBu_7 |
| **PDBu-9-2_tomo1-P2-DDD** | 925, 925, 241 | Polara2, K2 | 9,238 | 4-7 | 1850, 2325, 25 | 4.27 | PDBu_12 |
| **PDBu-9_tomo1** | 925, 925, 301 | Polara2, K2 | 9, 254+ 266-396 | 4,5 | 2200,2900, 50 | 4.27 | PDBu_10 |
| **PDBu-9_tomo2** | 925, 925, 281 | Polara2, K2 | 9, 190 | 4-6 | -45, -11, 2 | 4.27 | PDBu_8 |
| **PDBu-9_tomo3** | 925, 925, 301 | Polara2, K2 | 9, 231 | no | 1790, 2170, 20 | 4.27 | PDBu_9 |
| **PDBu-9_tomo4** | 925, 925, 221 | Polara2, K2 | 9,223 | 4 | 250, 1500, 50 | 4.27 | PDBu_11 |
| **PDBu3-3-3_tomo1** | 512, 512, 131 | Polara2, CCD | 9, 72 | no | -0.2, -0.02, 0.01 | 4.57 | PDBu_1 |
| **PDBu3-4-3_tomo1** | 512, 512, 121 | Polara2, CCD | 9, 110 | no | -0.36, 0.2, 0.02 | 4.57 | PDBu_2 |
| **PDBu3-4-3_tomo2** | 512, 512, 151 | Polara2, CCD | 9,151 | no | -0.34, 0.2, 0.02 | 4.57 | PDBu_3 |
| **PDBu5-3-4_tomo4** | 512, 512, 161 | Polara2, CCD | 9,156 | 4-8 | -0.225, -0.015, 0.015 | 4.57 | PDBu_4 |
| **PDBu-12_tomo2_T2_K2** | 925, 925, 280 | T2, K2 | 9,138 | 4 | 2225, 2625, 25 | 4,21 | PDBu_14 |
| **PDBu-12_tomo3_T2_K2** | 925, 925, 220 | T2, K2 | 9,44 | 4 | 2500, 2800, 15 | 4,21 | PDBu_15 |
| **PDBu-12_tomo4** | 925, 925, 370 | T2, K2 | 9,210 | 4 | 1200, 2050, 30 | 4,21 | PDBu_16 |
| **CalC** | | | | | | | |
| **CalC-6-2-tomo1-P2-DDD** | 925, 925, 201 | Polara2, K2 | 9,210 | no | | 4,27 | CalC_2 |
| **CalC-8-1_tomo2-P2-DDD** | 925, 925, 231 | Polara2, K2 | 9,236 | 4-7: omega shape | 1900, 2350, 20 | 4,27 | CalC_3 |
| **CalC-8-1_tomo3-P2-DDD** | 925, 925, 261 | Polara2, K2 | 9-255 | 4-6: omega shape | 1800, 2400, 25 | 4,27 | CalC_4 |
| **CalC-8-1_tomo4-P2-DDD** | 925, 925, 281 | Polara2, K2 | 9-256 | no | -400, 450, 50 | 4,27 | CalC_5 |
| **CalC-8_tomo1-P2-DDD** | 925, 925, 306 | Polara2, K2 | 9-189 | no | 1550, 2600, 50 | 4,27 | CalC_1 |

| | | | | | | | |
|---|---|---|---|---|---|---|---|
| **CalC-9-3_tomo1-P2-DDD** | 925, 925, 251 | Polara2, K2 | 2-256 | no | 1950, 2850, 50 | 4,27 | CalC_6 |
| **CalC-9-3_tomo2-P2-DDD** | 925, 925, 261 | Polara2, K2 | 9,255+264, 418 | no | 2950, 3450, 25 | 4,27 | CalC_8 |
| **CalC-9-3_tomo3-P2-DDD** | 925, 925, 231 | Polara2, K2 | 9,192 | 4 | 2700, 3000, 15 | 4,27 | CalC_9 |
| **CalC-9-3_tomo4-P2-DDD** | 925, 925, 181 | Polara2, K2 | 9,226 | 4-7: vacuoles | 1300, 6300, 250 | 4,27 | CalC_7 |
| **CalC-11_tomo4_T2_K2** | 925,925,100 | T2, K2 | 9,255+265,434 | | 2250, 3800, 75 | 4,21 | CalC_10 |
| **Ro31** | | | | | | | |
| **Ro31-6-5-3_tomo4-P2-DDD** | 925, 925, 281 | Polara2, K2 | 9,207 | 7,8: vacuoles | 1850, 3300, 75 | 4,27 | Ro31_1 |
| **Ro31-9-4_tomo3-P2-DDD** | 925, 925, 401 | Polara2, K2 | 8,256 | no | -900, 4000, 200 | 4,27 | Ro31_2 |
| **Ro31-9-4_tomo4-P2-DDD** | 925, 925, 281 | Polara2, K2 | 9,248 + 257,389 | no | 120, 540, 20 | 4,27 | Ro31_4 |
| **Ro31-9-4_tomo5-P2-DDD** | 925, 925, 301 | Polara2, K2 | 9-256 | 7,8: vacuoles | -55, 5, 2.5 | 4,27 | Ro31_3 |
| **Ro31-11_tomo3-P2-DDD** | 925, 925, 211 | Polara2, K2 | 9-98 | 4: vac | 1815, 2055, 15 | 4,27 | Ro31_5 |
| **Ro31-11_tomo5-P2-DDD** | 925, 925, 211 | Polara2, K2 | 9-193 | 4-8: DCVs | 2250, 2700, 25 | 4,27 | Ro31_6 |
| **Ro31-12_tomo5-P2-DDD** | 925, 925, 251 | Polara2, K2 | 9,256+265,372 | no | 450, 750, 15 | 4,27 | Ro31_7 |
| **Ro31-12_tomo9-P2-DDD** | 925, 925, 311 | Polara2, K2 | 9-166 | no | 0, 1000, 50 | 4,27 | Ro31_8 |

Appendix
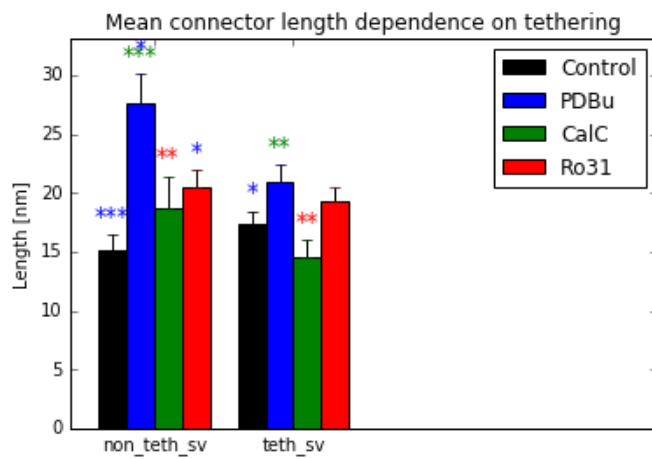


*Supplementary figure 1: Mean connector length for tethered (teth_sv) and non-tethered (non_teth_sv) SV*
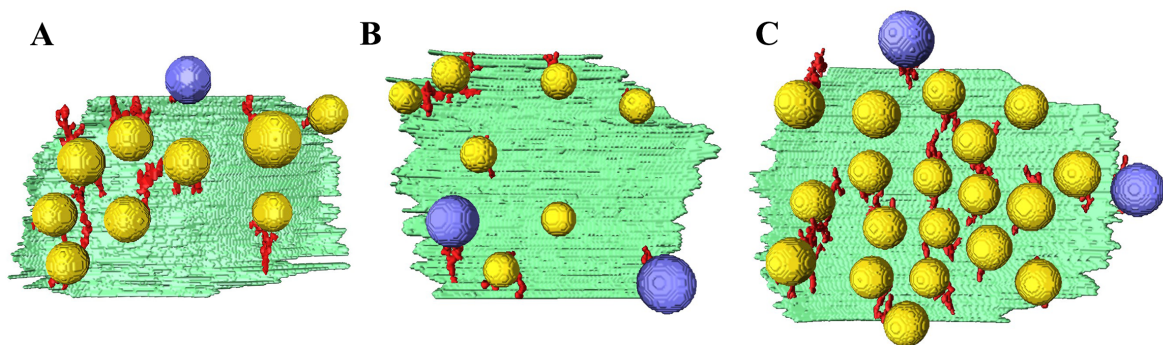


*Supplementary figure 2: Segmented AZ-membranes and tethered SVs illustrating the existence of long tethers close to the rim of the AZ.*
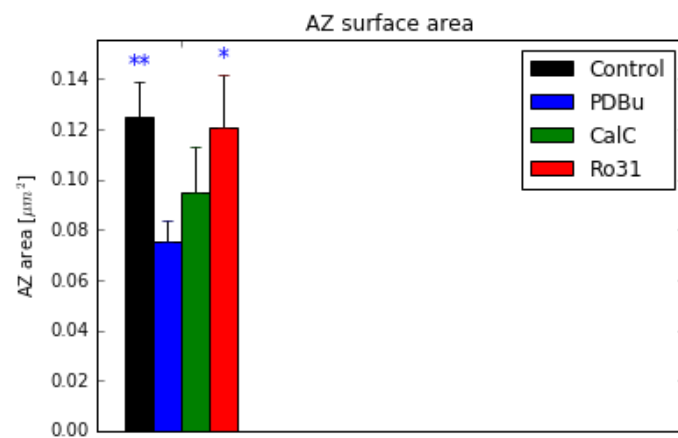


*Supplementary figure 3: AZ-surface area of control synaptosomes and all treatments in $\mu m2$.*

# 8. Abbreviations

| | |
|---|---|
| ADA | adenosine deaminase |
| AMPA | α-amino-3-hydroxy-5- methyl-4-isoxazolepropionic acid |
| AZ | active zone |
| BSA | bovine serum albumin |
| BIM-1 | Bisindolylmaleimide 1 |
| CalC | Calphostin C |
| CCD | charged-coupled device |
| CET | cryo-electron tomography |
| Cryo-EM | cryo-electron microscopy |
| CMF-HBSS | Calcium- and Magnesium-free Hank's Balanced Salt Solution |
| DED | Direct electron detector |
| DIV | days *in vitro* |
| DTT | Dithiotreitol |
| FM4-64 | (*N*-(3-Triethylammoniumpropyl)-4-(6-(4-(Diethylamino)Phenyl) Hexatrienyl)Pyridinium Dibromide) |
| GBD | glass bottom dish |
| GDH | Glutamate Dehydrogenase |
| GIF | Gatan imaging filter |
| GIS | Gas injection system |
| HB | Homogenization Buffer |
| HBM | Hepes-buffered medium |
| K-W test | Kruskal-Wallis test |
| L-AP4 | L-(+)-phosphonobutyrate |

Abbreviations

| | |
|---|---|
| NPM | Neuronal Plating Medium |
| PBS | Phosphate-Buffered Saline |
| PDBu | 4-β-phorbol-12,13-dibutyrate |
| PEI | Polyethyleneimine |
| PVDF | Polyvinylidendifluorid |
| RIPA | Radioimmunoprecipitation Assay |
| Ro31-8220 | 2-{1-[3-(Amidinothio)propyl]-1H-indol-3-yl}-3-(1-methylindol-3-yl)maleimide methane sulfonate salt, Bisindolylmaleimide IX |
| SDB | Semi-dry blotting buffer |
| SER | smooth endoplasmic reticulum |
| SPA | single particle analysis |
| SVE | synaptic vesicle endocytosis |
| SV | synaptic vesicle |
| Syt-1 | synaptotagmin-1 |

# 9. Bibliography

Acuna, C., Liu, X., Gonzalez, A., and Südhof, T.C. (2015). RIM-BPs Mediate Tight Coupling of Action Potentials to $Ca^{2+}$-Triggered Neurotransmitter Release. Neuron *87*, 1234–1247.

Aebi, U., and Pollard, T.D. (1987). A glow discharge unit to render electron microscope grids and other surfaces hydrophilic. J. Electron Microsc. Tech. *7*, 29–33.

Albert, S., Schaffer, M., Beck, F., Mosalaganti, S., Asano, S., Thomas, H.F., Plitzko, J.M., Beck, M., Baumeister, W., and Engel, B.D. (2017). Proteasomes tether to two distinct sites at the nuclear pore complex. Proc. Natl. Acad. Sci. *114*, 201716305.

Angleson, J.K., and Betz, W.J. (2000). Intraterminal Ca2+ and Spontaneous Transmitter Release at the Frog Neuromuscular. J. Physiol. *01*, 287–294.

Asano, S., Fukuda, Y., Beck, F., Aufderheide, A., Förster, F., Danev, R., and Baumeister, W. (2015). A molecular census of 26. Science *347*, 439–443.

Atasoy, D., Ertunc, M., Moulder, K.L., Blackwell, J., Chung, C., Su, J., and Kavalali, E.T. (2008). Spontaneous and Evoked Glutamate Release Activates Two Populations of NMDA Receptors with Limited Overlap. J. Neurosci. *28*, 10151–10166.

Augustin, I., Rosenmund, C., Südhof, T.C., and Brose, N. (1999). Munc13-1 is essential for fusion competence of glutamatergic synaptic vesicles. Nature *400*, 457–461.

Basu, J., Shen, N., Dulubova, I., Lu, J., Guan, R., Guryev, O., Grishin, N. V., Rosenmund, C., and Rizo, J. (2005). A minimal domain responsible for Munc13 activity. Nat. Struct. Mol. Biol. *12*, 1017–1018.

Batlle, E., and Wilkinson, D.G. (2012). Molecular mechanisms of cell segregation and boundary formation in development and tumorigenesis. Cold Spring Harb Perspect Biol *4*, a008227.

Beck, M., Förster, F., Ecke, M., Plitzko, J.M., Melchior, F., Gerisch, G., Baumeister, W., and Medalia, O. (2004). Nuclear Pore Complex Structure and Dynamics Revealed by Cryoelectron Tomography. Science (80-. ). *306*, 1387–1390.

Bennett, M.V.L. (2000). Seeing is relieving: Electrical synapses between visualized neurons. Nat. Neurosci. *3*, 7–9.

Betz, A., Okamoto, M., Benseler, F., and Brose, N. (1997). Direct interaction of the rat unc-13 homologue munc13-1 with the N terminus of syntaxin. J. Biol. Chem. *272*, 2520–2526.

# Bibliography

Betz, A., Ashery, U., Rickmann, M., Augustin, I., Neher, E., Südhof, T.C., Rettig, J., and Brose, N. (1998). Munc13-1 is a presynaptic phorbol ester receptor that enhances neurotransmitter release. Neuron *21*, 123–136.

Brandt, F., Carlson, L.A., Hartl, F.U., Baumeister, W., and Grünewald, K. (2010). The Three-Dimensional Organization of Polyribosomes in Intact Human Cells. Mol. Cell *39*, 560–569.

Bury, L.A., and Sabo, S.L. (2011). Coordinated trafficking of synaptic vesicle and active zone proteins prior to synapse formation. Neural Dev. *6*, 24.

Bury, L.A.D., and Sabo, S.L. (2016). Building a Terminal: Mechanisms of Presynaptic Development in the CNS. Neuroscientist *22*, 372–391.

Calakos, N., Schoch, S., Südhof, T.C., and Malenka, R.C. (2004). Multiple roles for the active zone protein RIM1alpha in late stages of neurotransmitter release. Neuron *42*, 889–896.

Camacho, M., Basu, J., Trimbuch, T., Chang, S., Pulido-Lozano, C., Chang, S.S., Duluvova, I., Abo-Rady, M., Rizo, J., and Rosenmund, C. (2017). Heterodimerization of Munc13 C2A domain with RIM regulates synaptic vesicle docking and priming. Nat. Commun. *8*, 1–13.

Chen, Y., Pfeffer, S., Hrabe, T., Schuller, J.M., and Förster, F. (2013). Fast and accurate reference-free alignment of subtomograms. J. Struct. Biol. *182*, 235–245.

Chung, C., Barylko, B., Leitz, J., Liu, X., and Kavalali, E.T. (2010). Acute Dynamin Inhibition Dissects Synaptic Vesicle Recycling Pathways That Drive Spontaneous and Evoked Neurotransmission. J. Neurosci. *30*, 1363–1376.

Coppola, T., Magnin-Lüthi, S., Perret-Menoud, V., Gattesco, S., Schiavo, G., and Regazzi, R. (2001). Direct Interaction of the Rab3 Effector RIM with Ca2+ Channels, SNAP-25, and Synaptotagmin. J. Biol. Chem. *276*, 32756–32762.

Cowen, M., Südhof, T.C., and Stevens, C.F. (2001). The Structure of Synapses. In Synapses, T.C. Südhof, and C.F. Stevens, eds. (Baltimore: JHU Press, 2003), p. 767.

Crowther, R.A., DeRosier, D.J., and Klug, A. (1970). The Reconstruction of a Three-Dimensional Structure from Projections and its Application to Electron Microscopy. Proc. R. Soc. A Math. Phys. Eng. Sci. *317*, 319–340.

Danev, R., Buijsse, B., Khoshouei, M., Plitzko, J.M., and Baumeister, W. (2014). Volta potential phase plate for in-focus phase contrast transmission electron microscopy. Proc. Natl. Acad. Sci. *111*, 15635–15640.

Dani, A., Huang, B., Bergan, J., Dulac, C., and Zhuang, X. (2010). Superresolution imaging of

chemical synapses in the brain. Neuron *68*, 843–856.

Daniel, J. a, Malladi, C.S., Kettle, E., McCluskey, A., and Robinson, P.J. (2012). Analysis of synaptic vesicle endocytosis in synaptosomes by high-content screening. Nat. Protoc. *7*, 1439–1455.

Daum, B., Walter, A., Horst, A., Osiewacz, H.D., and Kühlbrandt, W. (2013). Age-dependent dissociation of ATP synthase dimers and loss of inner-membrane cristae in mitochondria. Proc. Natl. Acad. Sci. *110*, 15301–15306.

Deng, L., Kaeser, P.S., Xu, W., and Südhof, T.C. (2011). RIM proteins activate vesicle priming by reversing autoinhibitory homodimerization of Munc13. Neuron *69*, 317–331.

Dresbach, T., Torres, V., Wittenmayer, N., Altrock, W.D., Zamorano, P., Zuschratter, W., Nawrotzki, R., Ziv, N.E., Garner, C.C., and Gundelfinger, E.D. (2006). Assembly of active zone precursor vesicles: Obligatory trafficking of presynaptic cytomatrix proteins Bassoon and Piccolo via A trans-Golgi compartment. J. Biol. Chem. *281*, 6038–6047.

Dubochet, J., Adrian, M., Chan, J., Lepault, J., and Mcdowall, A.W. (1988a). Chapter 5 Cryoelectron Microscopy of Vitrified Specimens. *2*, 129–228.

Dubochet, J., Adrian, M., Chang, J.-J., Homo, J.-C., Lepault, J., Mcdowall, A.W., and Schultz, P. (1988b). Cryo-electron microscopy of vitrified specimen. Q. Rev. Biophys. *21*, 129–228.

Dunkley, P.R., Heath, J.W., Harrison, S.M., Jarvie, P.E., Glenfield, P.J., and Rostas, J.A.P. (1988). A rapid Percoll gradient procedure for isolation of synaptosomes directly from an S1 fraction: homogeneity and morphology of subcellular fractions. Brain Res. *441*, 59–71.

Dunkley, P.R., Jarvie, P.E., and Robinson, P.J. (2008). A rapid Percoll gradient procedure for preparation of synaptosomes. Nat. Protoc. *3*, 1718–1728.

Ehlers, M.D., Heine, M., Groc, L., Lee, M.C., and Choquet, D. (2007). Diffusional Trapping of GluR1 AMPA Receptors by Input-Specific Synaptic Activity. Neuron *54*, 447–460.

Engel, B.D., Schaffer, M., Cuellar, L.K., Villa, E., Plitzko, J.M., and Baumeister, W. (2015). Native architecture of the chlamydomonas chloroplast revealed by in situ cryo-electron tomography. Elife *2015*, 1–29.

Fabre, M., and García de Herreros, A. (1993). Phorbol ester-induced scattering of HT-29 human intestinal cancer cells is associated with down-modulation of E-cadherin. J. Cell Sci. *106*, 513–522.

Faruqi, A.R., and Henderson, R. (2007). Electronic detectors for electron microscopy. Curr. Opin. Struct. Biol. *17*, 549–555.

# Bibliography

Fernández-Busnadiego, R., and Lučić, V. (2012). The Cell at Molecular Resolution: Principles and Applications af Cryo-Electron Tomography. In Cellular Imaging Techniques for Neuroscience and Beyond, F.G. Wouterlood, ed. (San Diego: Academic Press.), pp. 141–184.

Fernández-Busnadiego, R., Zuber, B., Maurer, U.E., Cyrklaff, M., Baumeister, W., and Lučić, V. (2010). Quantitative analysis of the native presynaptic cytomatrix by cryoelectron tomography. J. Cell Biol. *188*, 145–156.

Fernández-Busnadiego, R., Schrod, N., Kochovski, Z., Asano, S., Vanhecke, D., Baumeister, W., and Lučić, V. (2011). Insights into the molecular organization of the neuron by cryo-electron tomography. J. Electron Microsc. (Tokyo). *60 Suppl 1*, S137-48.

Fernandez, J.J., Li, S., and Lučić, V. (2007). Three-dimensional anisotropic noise reduction with automated parameter tuning: Application to electron cryotomography. Curr. Top. Artif. Intell. *4788*, 60–69.

Fernandez, J.J., Laugks, U., Schaffer, M., Bäuerlein, F.J.B., Khoshouei, M., Baumeister, W., and Lučić, V. (2016). Removing Contamination-Induced Reconstruction Artifacts from Cryo-electron Tomograms. Biophys. J. *110*, 850–859.

Ferrero, J.J., Torres, M., and Sánchez-Prieto, J. (2011). Inhibitors of diacylglycerol metabolism reduce time to the onset of glutamate release potentation by mGlu7 receptors. Neurosci. Lett. *500*, 144–147.

Ferrero, J.J., Alvarez, A.M., Ramirez-Franco, J., Godino, M.C., Bartolome-Martin, D., Aguado, C., Torres, M., Lujan, R., Ciruela, F., and Sanchez-prieto, J. (2013). beta-Adrenergic Receptors Activate Exchange Protein Directly Activated by cAMP ( Epac ), Translocate Munc13-1 , and Enhance the Rab3A-RIM1alpha Interaction to Potentiate Glutamate Release at Cerebrocortical Nerve Terminals. J. Biol. Chem. *288*, 31370–31385.

Förster, F., Villa, E., Thomas, D., Korinek, A., and Baumeister, W. (2012). Structure Determination of Macromolecular Complexes by Cryo-Electron Microscopy in vitro and in situ. In Biophysical Techniques for Structural Characterization of Macromolecules (Comprehensive Biophysics), H.J. Dyson, ed. (Amsterdam: Elsevier), pp. 245–276.

Forsythe, I.D., and Clements, J.D. (1990). Presynaptic glutamate receptors depress excitatory monosynaptic transmission between mouse hippocampal neurones. J. Physiol. *429*, 1–16.

Frank, J. (2006). Three-Dimensional Electron Microscopy of Macromolecular Assemblies: Visualization of Biological Molecules in Their Native State (New York: Oxford University Press).

Fukuda, Y., Laugks, U., Lučić, V., Baumeister, W., and Danev, R. (2015). Electron cryotomography of vitrified cells with a Volta phase plate. J. Struct. Biol. *190*, 143–154.

Garvalov, B.K., Zuber, B., Bouchet-Marquis, C., Kudryashev, M., Gruska, M., Beck, M., Leis, A.,

Frischknecht, F., Bradke, F., Baumeister, W., et al. (2006). Luminal particles within cellular microtubules. J. Cell Biol. *174*, 759–765.

Geppert, M., Goda, Y., Hammer, R.E., Li, C., Rosahl, T.W., Stevens, C.F., and Südhof, T.C. (1994). Synaptotagmin I: A major Ca2+sensor for transmitter release at a central synapse. Cell *79*, 717–727.

Geppert, M., Goda, Y., Stevens, C.F., and Südhof, T.C. (1997). The small GTP-binding protein Rab3A regulates a late step in synaptic vesicle fusion. Nature *387*, 810–814.

Gereau, R.W., and Conn, P.J. (1995). Multiple presynaptic metabotropic glutamate receptors modulate excitatory and inhibitory synaptic transmission in hippocampal area CA1. J. Neurosci. *15*, 6879–6889.

Giraudo, C.G., Eng, W.S., Melia, T.J., and Rothman, J.E. (2006). A clamping mechanism involved in SNARE-dependent exocytosis. Science (80-. ). *313*, 676–680.

Gitler, D., Cheng, Q., Greengard, P., and Augustine, G.J. (2008). Synapsin IIa Controls the Reserve Pool of Glutamatergic Synaptic Vesicles. J. Neurosci. *28*, 10835–10843.

Glaeser, R.M. (1999). Review: Electron crystallography: Present excitement, a nod to the past, anticipating the future. J. Struct. Biol. *128*, 3–14.

Glaeser, R.M., and Taylor, K.A. (1978). Radiation damage relative to transmission electron microscopy of biological specimens at low temperature: a review. J. Microsc. *112*, 127–138.

Goldstein, J.I., Newbury, D.E., Echlin, P., Joy, D.C., Lyman, C.E., Lifshin, E., Sawyer, L., and Michael, J.R. (2003). The SEM and Its Modes of Operation. In Scanning Electron Microscopy and X-Ray Microanalysis, (Boston, MA: Springer US), p. 675.

Gopalakrishna, R., Chen, Z.H., and Gundimeda, U. (1992). Irreversible oxidative inactivation of protein kinase C by photosensitive inhibitor calphostin C. FEBS Lett. *314*, 149–154.

Grimm, R., Koster, A.J., Ziese, U., Typke, D., and Baumeister, W. (1996). Zero-loss energy filtering under low-dose conditions using a post-column energy filter. J. Microsc. *183*, 60–68.

Grimm, R., Bärmann, M., Häckl, W., Typke, D., Sackmann, E., and Baumeister, W. (1997). Energy filtered electron tomography of ice-embedded actin and vesicles. Biophys. J. *72*, 482–489.

Hagen, W.J.H., Wan, W., and Briggs, J.A.G. (2017). Implementation of a cryo-electron tomography tilt-scheme optimized for high resolution subtomogram averaging. J. Struct. Biol. *197*, 191–198.

Han, Y., Kaeser, P.S., Südhof, T.C., and Schneggenburger, R. (2011). RIM determines $Ca^{2}+$ channel density and vesicle docking at the presynaptic active zone. Neuron *69*, 304–316.

# Bibliography

Hanson, P.I., Roth, R., Morisaki, H., Jahn, R., and Heuser, J.E. (1997). Structure and conformational changes in NSF and its membrane receptorcomplexes visualized by quick-freeze/deep-etch electron microscopy. Cell *90*, 523–535.

Harris, K., and Sultan, P. (1995). Variation in the number, location and size of synaptic vesicles provides an anatomical basis for the nonuniform probability of release at hippocampal CA1 synapses. Neuropharmacology *34*, 1387–1395.

Hegerl, R. (1996). The EM Program Package: A Platform for Image Processing in Biological Electron Microscopy. J. Struct. Biol. *116*, 30–34.

Hepp, R., Cabaniols, J., and Roche, P. (2002). Differential phosphorylation of SNAP-25 in vivo by protein kinase C and protein kinase A. FEBS Lett. *532*, 52–56.

Heuser, J.E., and Reese, T.S. (1973). Evidence for recycling of synaptic vesicle membrane during transmitter release at the frog neuromuscular junction. J. Cell Biol. *57*, 315–344.

Houeland, G., Nakhost, A., Sossin, W.S., and Castellucci, V.F. (2007). PKC Modulation of Transmitter Release by SNAP-25 at Sensory-to-Motor Synapses in Aplysia. J. Neurophysiol. *97*, 134–143.

Hui, E., Johnson, C.P., Yao, J., Dunning, F.M., and Chapman, E.R. (2009). Synaptotagmin-Mediated Bending of the Target Membrane Is a Critical Step in Ca2+-Regulated Fusion. Cell *138*, 709–721.

Hunter, J.D., and Hunter, B.J.D. (2011). Matplotlib : A 2D Graphics Environment. Sci. Program. *90*, 90–95.

Jahn, R., and Fasshauer, D. (2012). Molecular machines governing exocytosis of synaptic vesicles. Nature *490*, 201–207.

Jahn, R., and Südhof, T.C. (1999). Membrane fusion and exocytosis. Annu. Rev. Biochem. *68*, 863–911.

de Jong, A.P., and Verhage, M. (2009). Presynaptic signal transduction pathways that modulate synaptic transmission. Curr. Opin. Neurobiol. *19*, 245–253.

de Jong, A.P.H., Meijer, M., Saarloos, I., Cornelisse, L.N., Toonen, R.F.G., Sørensen, J.B., and Verhage, M. (2016). Phosphorylation of synaptotagmin-1 controls a post-priming step in PKC-dependent presynaptic plasticity. Proc. Natl. Acad. Sci. *113*, 5095–5100.

Jovanovic, J.N., Sihra, T.S., Nairn, A.C., Hemmings, H.C., Greengard, P., and Czernik, A.J. (2001). Opposing Changes in Phosphorylation of Specific Sites in Synapsin I During Ca2-Dependent Glutamate Release in Isolated Nerve Terminals. J. Neurosci. *21*, 7944–7953.

Junge, H.J., Rhee, J.S., Jahn, O., Varoqueaux, F., Spiess, J., Waxham, M.N., Rosenmund, C., and Brose, N. (2004). Calmodulin and Munc13 form a Ca2+sensor/effector complex that controls short-term synaptic plasticity. Cell *118*, 389–401.

Kaech, S., and Banker, G. (2006). Culturing hippocampal neurons. Nat. Protoc. *1*, 2406–2415.

Kaeser, P.S., and Regehr, W.G. (2014). Molecular Mechanisms for Synchronous, Asynchronous, and Spontaneous Neurotransmitter Release. Annu. Rev. Physiol. *76*, 333–363.

Kaeser, P.S., Deng, L., Wang, Y., Dulubova, I., Liu, X., Rizo, J., and Südhof, T.C. (2011). RIM proteins tether Ca2+ channels to presynaptic active zones via a direct PDZ-domain interaction. Cell *144*, 282–295.

Kamin, D., Lauterbach, M.A., Westphal, V., Keller, J., Schönle, A., Hell, S.W., and Rizzoli, S.O. (2010). High- And low-mobility stages in the synaptic vesicle cycle. Biophys. J. *99*, 675–684.

Khoshouei, M., Radjainia, M., Baumeister, W., and Danev, R. (2017). Cryo-EM structure of haemoglobin at 3.2 Å determined with the Volta phase plate. Nat. Commun. *8*, 1–6.

Kirkland, A.I., Chang, S.L.-Y.Y., and Hutchison, J.L. (2007). Atomic Resolution Transmission Electron Microscopy. In Science of Microscopy, pp. 3–64.

Kisielowski, C., Freitag, B., Bischoff, M., Lin, H. Van, Lazar, S., Knippels, G., Tiemeijer, P., Stam, M. Van Der, Harrach, S. Von, Stekelenburg, M., et al. (2008). Microscopy Microanalysis Detection of Single Atoms and Buried Defects in Three Dimensions by Aberration-Corrected Electron Microscope with 0.5-Å Information Limit. Energy 469–477.

Kochovski, Z. (2014). Image analysis of molecular complexes present in cryo-tomograms of neuronal synapses.

Koning, R.I. (2010). Cryo-Electron Tomography of Cellular Microtubules (Elsevier Inc.).

Koster, A.J., Grimm, R., Typke, D., Hegerl, R., Stoschek, A., Walz, J., and Baumeister, W. (1997). Perspectives of Molecular and Cellular Electron Tomography. *308*, 276–308.

Kremer, J.R., Mastronarde, D.N., and McIntosh, J.R. (1996). Computer visualization of three-dimensional image data using IMOD. J. Struct. Biol. *116*, 71–76.

Krivanek, O.L., and Mooney, P.E. (1993). Applications of slow-scan CCD cameras in transmission electron microscopy. Ultramicroscopy *49*, 95–108.

Krivanek, O.L., Friedman, S.L., Gubbens, A.J., and Kraus, B. (1995). An imaging filter for biological applications. Ultramicroscopy *59*, 267–282.

# Bibliography

Ladera, C., Martín, R., Bartolomé-Martín, D., Torres, M., and Sánchez-Prieto, J. (2009). Partial compensation for N-type Ca(2+) channel loss by P/Q-type Ca(2+) channels underlines the differential release properties supported by these channels at cerebrocortical nerve terminals. Eur. J. Neurosci. *29*, 1131–1140.

Laemmli, U.K. (1970). Cleavage of structural proteins during the assembly of the head of bacteriophage T4. Nature *227*, 680–685.

Lee, H.-K. (2006). Synaptic plasticity and phosphorylation. Pharmacol. Ther. *112*, 810–832.

Lee, J.S., Ho, W.-K., Neher, E., and Lee, S.-H. (2013). Superpriming of synaptic vesicles after their recruitment to the readily releasable pool. Proc. Natl. Acad. Sci. *110*, 15079–15084.

Li, W., Ma, C., Guan, R., Xu, Y., Tomchick, D.R., and Rizo, J. (2011). The crystal structure of a Munc13 C-terminal module exhibits a remarkable similarity to vesicle tethering factors. Structure *19*, 1443–1455.

Li, X., Mooney, P., Zheng, S., Booth, C.R., Braunfeld, M.B., Gubbens, S., Agard, D.A., and Cheng, Y. (2013). Electron counting and beam-induced motion correction enable near-atomic-resolution single-particle cryo-EM. Nat. Methods *10*, 584–590.

Liu, X., Seven, A.B., Camacho, M., Esser, V., Xu, J., Trimbuch, T., Quade, B., Su, L., Ma, C., Rosenmund, C., et al. (2016). Functional synergy between the Munc13 C-terminal C1and C2domains. Elife *5*, 1–27.

Lottspeich, F., and Engels, J.W. (2006). Bioanalytik.

Lou, X., Scheuss, V., and Schneggenburger, R. (2005). Allosteric modulation of the presynaptic Ca2+ sensor for vesicle fusion. Nature *435*, 497–501.

Lou, X., Korogod, N., Brose, N., and Schneggenburger, R. (2008). Phorbol Esters Modulate Spontaneous and Ca2+-Evoked Transmitter Release via Acting on Both Munc13 and Protein Kinase C. J. Neurosci. *28*, 8257–8267.

Lu, J., Machius, M., Dulubova, I., Dai, H., Südhof, T.C., Tomchick, D.R., and Rizo, J. (2006). Structural basis for a Munc13-1 homodimer to Munc13-1/RIM heterodimer switch. PLoS Biol. *4*, 1159–1172.

Lučić, V., Förster, F., and Baumeister, W. (2005a). Structural studies by electron tomography: from cells to molecules. Annu. Rev. Biochem. *74*, 833–865.

Lučić, V., Yang, T., Schweikert, G., Förster, F., and Baumeister, W. (2005b). Morphological characterization of molecular complexes present in the synaptic cleft. Structure *13*, 423–434.

Lučić, V., Kossel, A.H., Yang, T., Bonhoeffer, T., Baumeister, W., and Sartori, A. (2007). Multiscale

imaging of neurons grown in culture: from light microscopy to cryo-electron tomography. J. Struct. Biol. *160*, 146–156.

Lučić, V., Rigort, A., and Baumeister, W. (2013). Cryo-electron tomography: The challenge of doing structural biology in situ. J. Cell Biol. *202*, 407–419.

Lučić, V., Fernández-Busnadiego, R., Laugks, U., and Baumeister, W. (2016). Hierarchical detection and analysis of macromolecular complexes in cryo-electron tomograms using Pyto software. J. Struct. Biol. *196*, 503–514.

Ma, C., Li, W., Xu, Y., and Rizo, J. (2011). Munc13 mediates the transition from the closed syntaxin-Munc18 complex to the SNARE complex. Nat. Struct. Mol. Biol. *18*, 542–549.

Malenka, R.C., Madison, D. V, and Nicoll, R.A. (1986). Potentiation of synaptic transmission in the hippocampus by phorbol esters. Nature *321*, 175–177.

Martín, R., Durroux, T., Ciruela, F., Torres, M., Pin, J.-P., and Sánchez-Prieto, J. (2010). The metabotropic glutamate receptor mGlu7 activates phospholipase C, translocates munc-13-1 protein, and potentiates glutamate release at cerebrocortical nerve terminals. J. Biol. Chem. *285*, 17907–17917.

Martín, R., Bartolomé-Martín, D., Torres, M., and Sánchez-Prieto, J. (2011). Non-additive potentiation of glutamate release by phorbol esters and metabotropic mGlu7 receptor in cerebrocortical nerve terminals. J. Neurochem. *116*, 476–485.

Mastronarde, D.N. (2005). Automated electron microscope tomography using robust prediction of specimen movements. J. Struct. Biol. *152*, 36–51.

McKinney, R.A., Capogna, M., Dürr, R., Gähwiler, B.H., and Thompson, S.M. (1999). Miniature synaptic events maintain dendritic spines via AMPA receptor activation. Nat. Neurosci. *2*, 44–49.

McMullan, G., Faruqi, A.R., Clare, D., and Henderson, R. (2014). Comparison of optimal performance at 300 keV of three direct electron detectors for use in low dose electron microscopy. Ultramicroscopy *147*, 156–163.

Millán, C., Luján, R., Shigemoto, R., and Sánchez-Prieto, J. (2002). Subtype-specific expression of group III metabotropic glutamate receptors and Ca2+ channels in single nerve terminals. J. Biol. Chem. *277*, 47796–47803.

Millán, C., Torres, M., and Sánchez-Prieto, J. (2003). Co-activation of PKA and PKC in cerebrocortical nerve terminals synergistically facilitates glutamate release. J. Neurochem. *87*, 1101–1111.

Mori, N., Oikawa, T., Katoh, T., Miyahara, J., and Harada, Y. (1988). Application of the "imaging plate" to TEM image recording. Ultramicroscopy *25*, 195–201.

# Bibliography

Mosior, M., and Newton, A.C. (1995). Mechanism of Interaction of Protein Kinase C with Phorbol Esters. J. Biol. Chem. *270*, 25526–25533.

Nagy, G., Matti, U., Nehring, R.B., Binz, T., Rettig, J., Neher, E., and Sørensen, J.B. (2002). Protein kinase C-dependent phosphorylation of synaptosome-associated protein of 25 kDa at Ser187 potentiates vesicle recruitment. J. Neurosci. *22*, 9278–9286.

Newton, A.C. (1995). Protein Kinase C : Structure, Function ,and Regulation. J. Biol. Chem. *270*, 28495–28498.

Nicholls, D.G. (1998). Presynaptic modulation of glutamate release. Prog. Brain Res. *116*, 15–22.

Nicholls, D.G., Sihra, T.S., and Sanchez-prieto, J. (1987). Calcium-Dependent and -Independent Release of Glutamate from Synaptosomes Monitored by Continous Fluorometry. J. Neurochem. *49*, 50–57.

Nickell, S., Förster, F., Linaroudis, A., Net, W.D., Beck, F., Hegerl, R., Baumeister, W., and Plitzko, J.M. (2005). TOM software toolbox: acquisition and analysis for electron tomography. J. Struct. Biol. *149*, 227–234.

Nishizuka, Y. (1988). The molecular heterogeneity of protein kinase C and its implications for cellular regulation. Nature *334*, 661–665.

Nogales, E., and Scheres, S.H.W. (2015). Cryo-EM: A Unique Tool for the Visualization of Macromolecular Complexity. Mol. Cell *58*, 677–689.

Palfreyman, M., and Jorgensen, E.M. (2007). PKC Defends Crown Against Munc13. Neuron *54*, 179–180.

Parfitt, B.Y.K.D., and Madison, D. V (1993). Phorbol esters enhance synaptic transmission by a presynaptic, calium-dependent mechanism in rat hippocampus. J. Physiol. *471*, 245–268.

Peng, A., Rotman, Z., Deng, P.-Y., and Klyachko, V.A. (2012). Differential motion dynamics of synaptic vesicles undergoing spontaneous and activity-evoked endocytosis. Neuron *73*, 1108–1115.

Radermacher, M. (2006). Weighted back-projection methods. In Electron Tomography: Methods for Three-Dimensional Visualization of Structures in the Cell, (New York: Springer US), pp. 245–273.

Ramirez, D.M.O., and Kavalali, E.T. (2011). Differential regulation of spontaneous and evoked neurotransmitter release at central synapses. Curr. Opin. Neurobiol. *21*, 275–282.

Reim, K., Mansour, M., Varoqueaux, F., McMahon, H.T., Südhof, T.C., Brose, N., and Rosenmund, C. (2001). Complexins regulate a late step in Ca2+-dependent neurotransmitter release. Cell *104*, 71–81.

Reimer, L., and Kohl, H. (2008). Transmission Electron Microscopy, Physics of Image Formation

(New York: Springer US).

Rhee, J.S., Betz, A., Pyott, S., Reim, K., Varoqueaux, F., Augustin, I., Hesse, D., Südhof, T.C., Takahashi, M., Rosenmund, C., et al. (2002). Beta phorbol ester- and diacylglycerol-induced augmentation of transmitter release is mediated by Munc13s and not by PKCs. Cell *108*, 121–133.

Rigort, A., Bäuerlein, F.J.B., Leis, A., Gruska, M., Hoffmann, C., Laugks, T., Böhm, U., Eibauer, M., Gnaegi, H., Baumeister, W., et al. (2010). Micromachining tools and correlative approaches for cellular cryo-electron tomography. J. Struct. Biol. *172*, 169–179.

Rigort, A., Bäuerlein, F.J.B., Villa, E., Eibauer, M., Laugks, T., Baumeister, W., and Plitzko, J.M. (2012). Focused ion beam micromachining of eukaryotic cells for cryoelectron tomography. PNAS *109*, 4449–4454.

Robbins, E.M., Krupp, A.J., Perez de Arce, K., Ghosh, A.K., Fogel, A.I., Boucard, A., Südhof, T.C., Stein, V., and Biederer, T. (2010). SynCAM 1 Adhesion Dynamically Regulates Synapse Number and Impacts Plasticity and Learning. Neuron *68*, 894–906.

Rosenmund, C., and Stevens, C.F. (1996). Definition of the Readily Releasable Pool of Vesicles at Hippocampal Synapses. Neuron *16*, 1197–1207.

Ruskin, R.S., Yu, Z., and Grigorieff, N. (2013). Quantitative characterization of electron detectors for transmission electron microscopy. J. Struct. Biol. *184*, 385–393.

Sanchez-Prieto, J., Sihra, T.S., Evans, D., Ashton, A., Dolly, J.O., and Nicholls, D.G. (1987). Botulinum toxin A blocks glutamate exocytosis from guinea-pig cerebral cortical synaptosomes. Eur. J. Biochem. *165*, 675–681.

Sara, Y., Virmani, T., Deák, F., Liu, X., and Kavalali, E.T. (2005). An isolated pool of vesicles recycles at rest and drives spontaneous neurotransmission. Neuron *45*, 563–573.

Saxton, W.O., Baumeister, W., and Hahn, M. (1984). Three-dimensional reconstruction of imperfect two-dimensional crystals. Ultramicroscopy *13*, 57–70.

Schindelin, J., Arganda-Carreras, I., Frise, E., Kaynig, V., Longair, M., Pietzsch, T., Preibisch, S., Rueden, C., Saalfeld, S., Schmid, B., et al. (2012). Fiji: An open-source platform for biological-image analysis. Nat. Methods *9*, 676–682.

Schoch, S., Deak, F., Konigstorfer, A., Mozhayeva, M., Sara, Y., Südhof, T.C., and Kavalali, E.T. (2001). SNARE Function Analyzed in Synaptobrevin / VAMP Knockout Mice. Science (80-. ). *294*, 1117–1123.

Schrod, N., Vanhecke, D., Laugks, U., Stein, V., Fukuda, Y., Schaffer, M., Baumeister, W., and Lucic,

# Bibliography

V. (2017). Short linkers as ubiquitous structural organizers of vesicles in axons. PLoS Med. 1–27.

Schur, F.K.M., Hagen, W.J.H., Rumlová, M., Ruml, T., Müller, B., Kraüsslich, H.G., and Briggs, J.A.G. (2015). Structure of the immature HIV-1 capsid in intact virus particles at 8.8 Å resolution. Nature *517*, 505–508.

Seong, E., Yuan, L., and Arikkath, J. (2015). Cadherins and catenins in dendrite and synapse morphogenesis. Cell Adhes. Migr. *9*, 202–213.

Shapira, M., Zhai, R.G., Dresbach, T., Bresler, T., Torres, V.I., Gundelfinger, E.D., Ziv, N.E., and Garner, C.C. (2003). Unitary assembly of presynaptic active zones from Piccolo-Bassoon transport vesicles. Neuron *38*, 237–252.

Shapira, R., Silberberg, S.D., Ginsburg, S., and Rahamimoff, R. (1987). Activation of protein kinase C augments evoked transmitter release. Nature *325*, 58–60.

Sihra, T.S., Wang, J.K., Gorelick, F.S., and Greengard, P. (1989). Translocation of synapsin I in response to depolarization of isolated nerve terminals. Proc. Natl. Acad. Sci. U. S. A. *86*, 8108–8112.

Siksou, L., Rostaing, P., Lechaire, J.-P., Boudier, T., Ohtsuka, T., Fejtová, A., Kao, H.-T., Greengard, P., Gundelfinger, E.D., Triller, A., et al. (2007). Three-dimensional architecture of presynaptic terminal cytomatrix. J. Neurosci. *27*, 6868–6877.

Silinsky, E.M., and Searl, T.J. (2003). Phorbol esters and neurotransmitter release: More than just protein kinase C? Br. J. Pharmacol. *138*, 1191–1201.

Sossin, W.S. (2007). Isoform specificity of protein kinase Cs in synaptic plasticity. Learn. Mem. *14*, 236–246.

Stevens, C.F., and Sullivan, J.M. (1998). Regulation of the readily releasable vesicle pool by protein kinase C. Neuron *21*, 885–893.

Südhof, T.C. (1995). The synaptic vesicle cycle: A cascade of protein-protein interactions. Nature *375*, 645–653.

Südhof, T.C. (2004). The synaptic vesicle cycle. Annu. Rev. Neurosci. *27*, 509–547.

Sutton, M.A., Ito, H.T., Cressy, P., Kempf, C., Woo, J.C., and Schuman, E.M. (2006). Miniature Neurotransmission Stabilizes Synaptic Function via Tonic Suppression of Local Dendritic Protein Synthesis. Cell *125*, 785–799.

Sutton, R.B., Fasshauer, D., Jahn, R., and Brunger, A.T. (1998). Crystal structure of a SNARE complex involved in synaptic exocytosis at 2.4 A resolution. Nature *395*, 347–353.

Tamaoki, T., Nomoto, H., Takahashi, I., Kato, Y., Morimoto, M., and Tomita, F. (1986). Staurosporine, a potent inhibitor of phospholipid/Ca++ dependent protein kinase. Biochem. Biophys. Res. Commun. *135*, 397–402.

Tang, G., Peng, L., Baldwin, P.R., Mann, D.S., Jiang, W., Rees, I., and Ludtke, S.J. (2007). EMAN2: An extensible image processing suite for electron microscopy. J. Struct. Biol. *157*, 38–46.

Tao-Cheng, J.H. (2007). Ultrastructural localization of active zone and synaptic vesicle proteins in a preassembled multi-vesicle transport aggregate. Neuroscience *150*, 575–584.

Tao, C.-L., Liu, Y.-T., Sun, R., Zhang, B., Qi, L., Shivakoti, S., Tian, C.-L., Zhang, P., Lau, P.-M., Zhou, Z.H., et al. (2018). Differentiation and characterization of excitatory and inhibitory synapses by cryo-electron tomography and correlative microscopy. J. Neurosci. *38*, 1548–17.

Taschenberger, H., Woehler, A., and Neher, E. (2016). Superpriming of synaptic vesicles as a common basis for intersynapse variability and modulation of synaptic strength. Proc. Natl. Acad. Sci. *113*, E4548–E4557.

Taylor, K.A., and Glaeser, R.M. (1974). Electron Diffraction of Frozen, Hydrated Protein Crystals. Science (80-. ). *186*, 1036–1037.

Tokumaru, H., and Augustine, G.J. (1999). Unc-13 and Neurotransmitter Release. Nature *2*, 929–930.

Torres, V.I., and Inestrosa, N.C. (2017). Vertebrate Presynaptic Active Zone Assembly: a Role Accomplished by Diverse Molecular and Cellular Mechanisms. Mol. Neurobiol. 4513–4528.

Tsukita, S., and Ishikawa, H. (1980). The Movement of Membraneous Organelles in Axons, Electron Microscopic Identification of Anterogradely and Retrogradely Transported Organelles. J. Cell Biol. *84*, 513–530.

Unverdorben, P., Beck, F., led , P., Schweitzer, A., Pfeifer, G., Plitzko, J.M., Baumeister, W., and Forster, F. (2014). Deep classification of a large cryo-EM dataset defines the conformational landscape of the 26S proteasome. Proc. Natl. Acad. Sci. *111*, 5544–5549.

Varoqueaux, F., Sigler, A., Rhee, J.-S., Brose, N., Enk, C., Reim, K., and Rosenmund, C. (2002). Total arrest of spontaneous and evoked synaptic transmission but normal synaptogenesis in the absence of Munc13-mediated vesicle priming. Proc. Natl. Acad. Sci. U. S. A. *99*, 9037–9042.

Verhage, M., Maia, A.S., Plomp, J.J., Brussaard, A.B., Heeroma, J.H., Vermeer, H., Toonen, R.F., Hammer, R.E., Van Den Berg, T.K., Missler, M., et al. (2000). Synaptic assembly of the brain in the absence of neurotransmitter secretion. Science (80-. ). *287*, 864–869.

Wagner, N., Laugks, U., Heckmann, M., Asan, E., and Neuser, K. (2015). Aging Drosophila

# Bibliography

melanogaster display altered pre- and postsynaptic ultrastructure at adult neuromuscular junctions. J. Comp. Neurol. *523*, 2457–2475.

Waites, C.L., Leal-Ortiz, S.A., Okerlund, N., Dalke, H., Fejtova, A., Altrock, W.D., Gundelfinger, E.D., and Garner, C.C. (2013). Bassoon and Piccolo maintain synapse integrity by regulating protein ubiquitination and degradation. EMBO J. *32*, 954–969.

Walker, J.M., Homan, E.C., and Sando, J.J. (1990). Differential activation of protein kinase C isozymes by short chain phosphatidylserines and phosphatidylcholines. J. Biol. Chem. *265*, 8016–8021.

Wehmer, M., Rudack, T., Beck, F., Aufderheide, A., Pfeifer, G., Plitzko, J.M., Förster, F., Schulten, K., Baumeister, W., and Sakata, E. (2017). Structural insights into the functional cycle of the ATPase module of the 26S proteasome. Proc. Natl. Acad. Sci. *114*, 1305–1310.

Westphal, V., Rizzoli, S.O., Lauterbach, M.A., Kamin, D., Jahn, R., and Hell, S.W. (2008). Video-rate far-field optical nanoscopy dissects synaptic vesicle movement. Science (80-. ). *320*, 246–249.

Whittaker, V.P. (1993). Thirty years of synaptosome research. J. Neurocytol. *22*, 735–742.

Wilhelm, B.G., Groemer, T.W., and Rizzoli, S.O. (2010). The same synaptic vesicles drive active and spontaneous release. Nat. Neurosci. *13*, 1454–1456.

Wilkinson, S.E., Parker, P.J., and Nixon, J.S. (1993). Isoenzyme specificity of bisindolylmaleimides, selective inhibitors of protein kinase C. Biochem. J. *294*, 335–337.

Williams, D.B., and Carter, C.B. (2009). Transmission electron microscopy: A textbook for materials science (New York: Springer US).

Wu, X.S., and Wu, L.G. (2001). Protein kinase c increases the apparent affinity of the release machinery to Ca2+ by enhancing the release machinery downstream of the Ca2+ sensor. J. Neurosci. *21*, 7928–7936.

Xia, X., Mariner, D.J., and Reynolds, A.B. (2003). Adhesion-associated and PKC-modulated changes in serine/threonine phosphorylation of p120-catenin. Biochemistry *42*, 9195–9204.

Zhai, R.G., Vardinon-Friedman, H., Cases-Langhoff, C., Becker, B., Gundelfinger, E.D., Ziv, N.E., and Garner, C.C. (2001). Assembling the presynaptic active zone: A characterization of an active zone precursor vesicle. Neuron *29*, 131–143.

Zhang, G., Kazanietz, M.G., Blumberg, P.M., and Hurley, J.H. (1995). Crystal structure of the Cys2 activator-binding domain of protein kinase Cδ in complex with phorbol ester. Cell *81*, 917–924.

Zhang, Y.H., Kenyon, J.L., and Nicol, G.D. (2001). Phorbol ester-induced inhibition of potassium

currents in rat sensory neurons requires voltage-dependent entry of calcium. J. Neurophysiol. *85*, 362–373.

Zheng, S.Q., Palovcak, E., Armache, J.P., Verba, K.A., Cheng, Y., and Agard, D.A. (2017). MotionCor2: anisotropic correction of beam-induced motion for improved cryo-electron microscopy. Nat. Methods *14*, 331–332.

Zhou, Q., Zhou, P., Wang, A.L., Wu, D., Zhao, M., Südhof, T.C., and Brunger, A.T. (2017). The primed SNARE-complexin-synaptotagmin complex for neuronal exocytosis. Nature *548*, 420–425.

Zuber, B., Nikonenko, I., Klauser, P., Muller, D., and Dubochet, J. (2005). The mammalian central nervous synaptic cleft contains a high density of periodically organized complexes. Proc. Natl. Acad. Sci. U. S. A. *102*, 19192–19197.

Zucker, R.S., and Regehr, W.G. (2002). Short-Term Synaptic Plasticity. Annu. Rev. Physiol. *64*, 355–405.

# 10.　　Acknowledgements

# 11. Publication List

Wagner, N., Laugks, U., Heckmann, M., Asan, E., and Neuser, K. (2015). Aging Drosophila melanogaster display altered pre- and postsynaptic ultrastructure at adult neuromuscular junctions. J. Comp. Neurol. *523*, 2457–2475.

Fukuda, Y., Laugks, U., Lučić, V., Baumeister, W., and Danev, R. (2015). Electron cryotomography of vitrified cells with a Volta phase plate. J. Struct. Biol. *190*, 143–154.

Fernandez, J.J., Laugks, U., Schaffer, M., Bäuerlein, F.J.B., Khoshouei, M., Baumeister, W., and Lučić, V. (2016). Removing Contamination-Induced Reconstruction Artifacts from Cryo-electron Tomograms. Biophys. J. *110*, 850–859.

Lučić, V., Fernández-Busnadiego, R., Laugks, U., and Baumeister, W. (2016). Hierarchical detection and analysis of macromolecular complexes in cryo-electron tomograms using Pyto software. J. Struct. Biol. *196*, 503–514.

Vargas, K.J., Schrod, N., Davis, T., Fernandez-Busnadiego, R., Taguchi, Y. V., Laugks, U., Lucic, V., and Chandra, S.S. (2017). Synucleins Have Multiple Effects on Presynaptic Architecture. Cell Rep. *18*, 161–173.

Laugks, U., Hieke, M., and Wagner, N. (2017). MAN1 Restricts BMP Signaling During Synaptic Growth in Drosophila. Cell. Mol. Neurobiol. *37*, 1077–1093.

Schrod, N., Vanhecke, D., Laugks, U., Stein, V., Fukuda, Y., Schaffer, M., Baumeister, W., and Lucic, V. (2017). Short linkers as ubiquitous structural organizers of vesicles in axons. PLoS Med. 1–27.

Radecke, J., Laugks, U., Goldie, K., McMahon, H.T., Stahlberg, H., Lucic, V., and Zuber, B. (2018). Time resolved cryo-electron tomography of synaptic vesicle exocytosis reveals structural modifications of synaptic vesicles and presynaptic cytomatrix. *in submission*

Martinez-Sanchez, A., Kochovski, Z., Laugks, U., Meyer zur alten Borgloh, J., Pfeffer, S., Baumeister, W., and Lucic, V. (2018). Template-free detection and classification of heterogeneous membrane-bound complexes in cryo-electron tomograms. 1–18. *in review*

# 12.    List of Tables

# 13.    List of Figures

List of Figures